STAR Note 401

AN ENDCAP ELECTROMAGNETIC CALORIMETER FOR STAR

CONCEPTUAL DESIGN REPORT

April 28, 1999

L.C. Bland, W.W. Jacobs, J. Sowinski, E.J. Stephenson, S.E. Vigdor and S.W. Wissink

Indiana University Cyclotron Facility

Contents

1 Overview

This document lays out the motivation and preliminary design for adding an endcap electromagnetic calorimeter (EEMC) to the STAR detector at RHIC. Allowance for an EEMC has been built into STAR from its inception, but this component becomes a crucial element of the detector only when one considers its application to the study of high-energy polarized proton collisions at RHIC. Specifically, it is the unique capabilities of STAR, supplemented by an endcap calorimeter, for determinations of the spin structure of protons, that drive the design of the proposed EEMC.

Figure 1 illustrates how the proposed endcap calorimeter will fit into the existing STAR detector. The EEMC will expand STAR's acceptance for photons, electrons and π^0 and η^0 mesons (via their decay to photon pairs) from the pseudorapidity range $|\eta| \leq 1.0$ to $-1.0 \leq \eta \leq 2.0$, with full azimuthal coverage. For hadron jets (which often include π^0 and η^0 mesons) that are fully contained within the active detector volume, the increase in acceptance is considerably more than a factor of two, from $|\eta| \leq 0.3$ to $-0.3 \leq \eta \leq 1.3$. The increased acceptance provides access to critical phase space regions for colliding beams of polarized protons or of protons and heavy nuclei, allowing STAR to provide: (1) the definitive measurement of the *gluon* contribution to the spin of a proton; (2) an effective separation of antiquark *vs.* quark contributions to the proton spin in $W^{\pm}$ production; (3) enhanced sensitivity to hyperon spin structure in measurements of the polarization transfer from beam protons to hyperon fragments of jets; (4) meaningful Standard Model tests via parity-violating helicity asymmetries in hard jet production; and (5) access to the most interesting kinematic regime in *nuclear* gluon distributions, probed in p-A collisions. The addition of the EEMC would thus enable STAR to meet some of the most important goals of the RHIC spin program [1], as well as to measure nuclear properties crucial to the RHIC heavy-ion collision program.
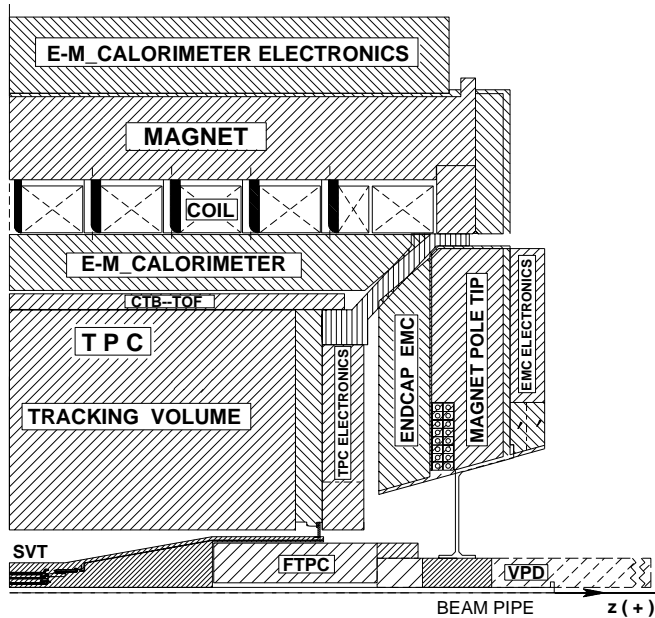
Figure 1: *A quarter-section of the cylindrically and reflection symmetric STAR detector, showing where the proposed endcap EMC would fit. The EEMC is an annulus of inner radius ≈ 75 cm, outer radius ≈ 215 cm and depth ≈ 34 cm. The inner and outer radii grow with depth, as indicated. Also shown are the time projection chamber (TPC) providing tracking for $-2 \leq \eta \leq +2$, central trigger barrel (CTB), barrel EMC (E-M CALORIMETER), silicon vertex tracker (SVT), forward TPC (FTPC) and a projected vertex position detector (VPD).*

In particular, simulations suggest that STAR with the EEMC will facilitate the world's best measurement of the unknown gluon spin contribution ΔG. It is already known that the gluons, despite having no intrinsic mass of their own and no direct influence on the quantum numbers of the nucleon, nonetheless dominate the nucleon's mass [2]. It is crucial to any understanding of

1

nucleon structure to find whether the gluons also make important contributions to spin. A direct measurement of ΔG holds the key to separating the quark, gluon and orbital angular momentum contributions to the proton's spin. A direct determination of ΔG requires interpretable strong-interaction processes that probe polarized gluons at low Bjorken x-values, $x_{gluon} < 0.1$, the region containing the vast majority of gluons in a nucleon. Low-order perturbative QCD (pQCD) should be adequate to describe hard collisions (with transverse momentum transfer $p_T \gtrsim 10$ GeV/c) of the high-energy polarized proton beams that will be available at RHIC. The large acceptance of STAR allows detection of the jets that signal most of the interesting partonic collision processes. With the addition of the endcap, one can detect γ-jet coincidences – a channel dominated by quark-gluon Compton scattering $(q + g \rightarrow q + \gamma)$ – over a kinematic range providing sensitivity to $0.01 \leq x_{gluon} \leq 0.3$. This point is illustrated, along with the quality of the data attainable, by simulations in Fig. 2, showing the $\vec{p} - \vec{p}$ spin correlation parameter expected for this channel, and the values of $\Delta G(x)$ that would be extracted therefrom with a simplified analysis algorithm. Measurements at two beam energies, $\sqrt{s} = 200$ and 500 GeV, are needed to cover this entire range in x_{gluon}, and the EEMC is essential to access the low-x gluons that dominate the integral spin contribution ΔG.
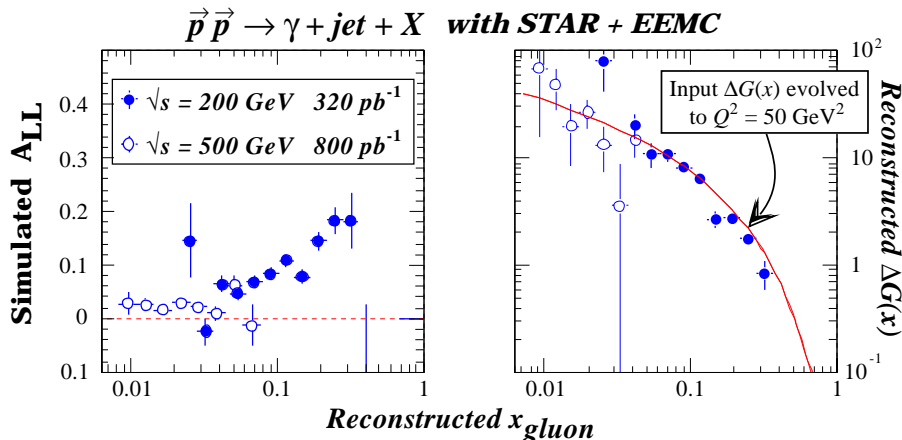
Figure 2: *Simulation results for the pp spin correlation A_{LL} and the gluon helicity distribution $\Delta G(x)$ extracted therefrom, for photon-jet coincidence events at $\sqrt{s}$=200 and 500 GeV. Simulations are shown for STAR including the proposed endcap EMC. The events that pass cuts described in Ref. [3] have been subjected to a simplified analysis algorithm (see Sec. 2) that assumes the only contributing process to be quark-gluon Compton scattering with $x_{quark} > x_{gluon}$. The error bars reflect counting statistics for the indicated integrated luminosities, corresponding to ten-week runs at each of the two energies, and for beam polarizations of 0.7. The solid curve in the right-hand frame represents the model input for $\Delta G(x, Q^2 = 50 \, (GeV/c)^2)$. Small systematic deviations between the input and extracted gluon helicity distributions arise from the simplifying assumptions in the data analysis (see Sec. 2), and are correctable via simulations.*

Of the envisioned physics program, it is the ΔG measurement via direct photon production and determination of antiquark helicity distributions via $W^\pm$ production that impose the most stringent demands on the EEMC performance. In particular, the EEMC must provide reasonable resolution and linearity in energy measurements for photons up to at least 50 GeV and for electrons and positrons up to at least 150 GeV. At these high energies, it must provide the means to distinguish

single photons from π^0 and η^0 mesons (which are considerably more abundant than direct photons at $p_T < 20$ GeV/c) and $e^\pm$ from charged hadrons. Its segmentation must be suitable to allow clean hardware triggering on these relatively rare events, at luminosities where minimum-bias pp collisions will occur in a substantial fraction of the RHIC beam crossings. Additional important constraints are imposed by budget and by integration within STAR; *e.g.*, STAR imposes serious limitations on the available depth (37.5 cm) for the EEMC and on the trigger and readout rates for pp collisions.

The solution we propose to the above performance demands is a lead-plastic scintillator sampling calorimeter, with a total depth of 21 radiation lengths and a sampling fraction of 6.6%. The active volume, providing full azimuthal coverage over the pseudorapidity range $1.07 \leq \eta \leq 2.00$, will be subdivided into 720 projective towers, each comprising 24 scintillator layers read out through optical fibers routed to a single phototube (PMT). A state-of-the-art shower-maximum detector (SMD), containing 7200 extruded plastic scintillating strips of triangular cross section, will be placed five layers deep within the EEMC. SMD readout via optical fibers and multi-anode PMT's should provide sufficient shower profile characterization to distinguish γ's from π^0's at the needed level up to 40-50 GeV. As an additional aid in $\gamma - \pi^0$ discrimination at still higher energies, and in distinguishing electrons from charged hadrons, we provide for independent readout of the first two scintillating layers within each calorimeter tower as a preshower detector.

Most aspects of the proposed design are conservative, in that they are based on technological solutions that have already been demonstrated to work well in recently constructed electromagnetic calorimeters of similar performance and/or geometry. We have carried out extensive simulations and some critical measurements to convince ourselves that the non-standard performance demands on the STAR EEMC, especially in γ/π^0 discrimination, can be realistically met with the proposed detector.

The estimated overall cost for constructing the EEMC and installing it within STAR is \$6.65 M. We are seeking the largest portion (\$4.27 M) of the necessary funding from the National Science Foundation, in two separate grants (one from the Physics Division and a second from the Major Research Instrumentation Program). An additional \$2 M is to be provided by Indiana University, in matching funds (\$0.86 M) and other specialized research accounts, and by the Indiana University Cyclotron Facility (IUCF) NSF-funded operating grant. We expect the remaining funding to be contributed from the research grants of other collaborating institutions. We envision a three-year construction project, culminating in installation of the EEMC within STAR during the summer shutdown in 2002. This timescale matches well the projected schedule for developing polarized proton beams in RHIC to the luminosities needed to achieve the spin physics goals laid out in more detail in the following section.

2   The Proposed Scientific Program

In this section we elaborate on the physics goals of the EEMC project, emphasizing the measurement of the gluon spin contribution to the overall proton spin, which represents the centerpiece of the RHIC spin program. The EEMC will also provide side benefits for nucleus-nucleus collision studies: *e.g.*, it will expand the rapidity range over which one can trigger on anomalous ratios of neutral- to charged-pion multiplicities, one of the suggested signatures of the momentary restoration of chiral symmetry in the very hot matter formed in RHIC collisions. However, the nucleus-nucleus program does not drive the design of the EEMC, and so is not described further below.

2.1   Probing the Gluon Spin Distribution

2.1.1   The Importance of ΔG

The overall spin projection of a longitudinally polarized proton can be decomposed as follows:

$$S_z \;=\; \frac{1}{2} \;=\; \frac{1}{2}\Delta\Sigma \;+\; \Delta G \;+\; L_z^q \;+\; L_z^G, \tag{1}$$

where Σ represents the summed contribution from up, down and strange quarks and antiquarks, and G represents contributions from gluons. The Δ in each case denotes the integrated (over momentum fraction, as measured by Bjorken x) *difference* in parton distribution functions for parton spins aligned parallel *vs.* antiparallel to the proton spin; L_z denotes the net orbital angular momentum projection of the indicated partons. The results of polarized deep inelastic scattering (DIS) experiments carried out at CERN, SLAC and DESY in recent years [4] are sometimes quoted as determining the value $\Delta\Sigma = 0.29 \pm 0.06$ (specified here [4] for a squared four-momentum transfer $Q^2 = 5$ GeV^2). This value is much smaller than that predicted (≈ 0.6) by relativistic constituent quark models [5]. However, the axial anomaly of QCD complicates the interpretation of the polarized DIS results [6], by introducing a dependence of the integrated asymmetry on ΔG, resulting in the *correlated* constraint on $\Delta\Sigma$ and ΔG shown in Fig. 3. (ΔG is actually a function of Q^2, but we suppress explicit mention of this dependence in most of what follows, for simplicity.) In fact, if ΔG were approximately $+3$, then not only $\Delta\Sigma$, but also the individual contributions from u, d and s quarks, would be restored to agreement with constituent quark models! Of course, then large and oppositely directed *orbital* contributions would be needed to reduce the overall proton spin projection to 1/2.
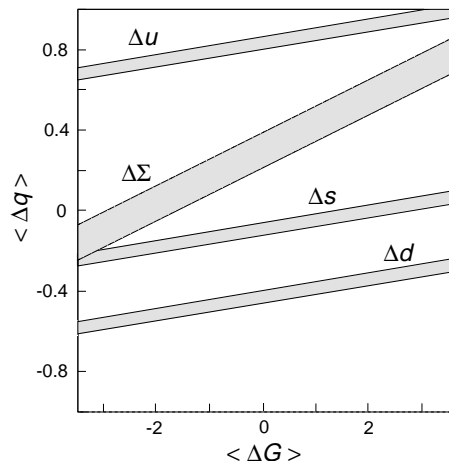
Figure 3: *The correlation of quark and gluon contributions to the longitudinal polarization of a proton, introduced by the effect of the QCD axial anomaly on the interpretation of polarized DIS asymmetries [4]. The separation of quark and gluon contributions to polarized DIS is scheme-dependent, and is shown here for one particular QCD factorization scheme. The bands in each case represent $\pm 1\sigma$ limits on the quark contributions deduced [4] from DIS results.*

4
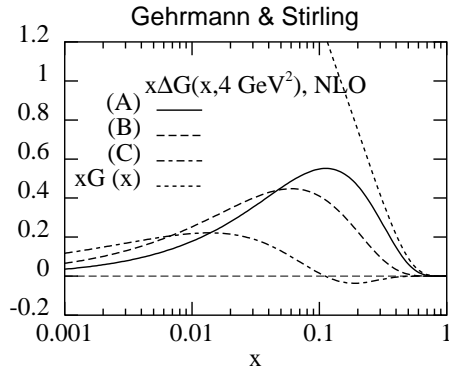
Figure 4: *Three models of the gluon helicity distribution used in next-leading-order global analyses of polarized DIS results by Gehrmann and Stirling [7]. All three are consistent with observed scaling violations in DIS. The solid curve (A), corresponding to an integral $\Delta G(4\ GeV^2)=1.71$, is used in simulations presented here.*

It is clear from these considerations that measurement of ΔG is the key to the next major breakthrough in understanding the nucleon's spin substructure. A precision better than ± 0.5 in ΔG would allow a meaningful assessment of the constituent quark model, by reducing the interpretation uncertainty for the DIS asymmetries to a level comparable to the present measurement uncertainties in these experiments. At the same time, such a result for ΔG would provide initial constraints on parton *orbital* angular momenta inside a proton. At present, ΔG is constrained only indirectly, by the spin-dependence of QCD-induced scaling violations in the DIS data [7], to lie roughly between zero and +3. The x-dependence $\Delta G(x)$ is essentially unconstrained, as suggested by the three very different "fits" in Fig. 4, where the gluon polarization $\Delta G(x)/G(x)$ near $x \approx 0.1$ varies from zero to 40%. Despite the fact that the gluon polarization for all three fits falls off with decreasing x, the integral $\Delta G \equiv \int_0^1 \Delta G(x) dx$ is still *dominated* in each case by contributions from $x < 0.1$, since this is the region where gluons are most abundant. [Note that $\Delta G(x)$ is multiplied by x in the curves in Fig. 4.] It is thus crucial to design measurements to constrain $\Delta G(x)$ to values of x as far below 0.1 as feasible.

Because the gluons participate only in the strong interaction, reactions used to probe $\Delta G(x)$ must be chosen carefully with respect to their selectivity and theoretical interpretability within the framework of perturbative QCD (pQCD). This criterion places a premium on high energies, on hard collisions (high transverse momentum transfer p_T), and on those experiments that approach most closely the ideal of measuring the gluon helicity preference *directly*, at leading order (LO) in pQCD and at experimentally determined values of x_{gluon}. The ultimate analyses to extract $\Delta G(x, Q^2)$ will certainly include pQCD contributions through at least next-to-leading order (NLO), but the significant theoretical ambiguities in such analyses will be best constrained if the corrections to LO calculations are small from the start.

2.1.2 Photon-Jet Coincidences

The study of direct photon production with STAR and the EEMC, in the reaction $\vec{p} + \vec{p} \to \gamma$+jet+X, has decisive advantages over most other proposed techniques in meeting the criteria for a significant measurement of the gluon spin contribution:

1) **In LO pQCD, there is a single dominant partonic collision subprocess:** $q+g \to q+\gamma$. The main LO background, from annihilation $q + \overline{q} \to \gamma + g$, contributes at the $\sim 10\%$ level [8]. NLO calculations [9] indicate no qualitative changes in spin sensitivity from the LO expectations (sensitivity to ΔG is slightly *enhanced*). Higher-twist corrections are expected to remain negligible at $p_T \gtrsim 10$ GeV/c, where RHIC count rates will still be reasonable.

5

2) **The sensitivity to gluon polarization is guaranteed to be large in an experiment with appropriate kinematic coverage.** QCD predicts large spin effects only when *both* colliding partons are polarized [8]. Sensitivity to gluon spin thus relies on the combination of a highly polarized collision partner with a sizable parton-level spin correlation [$\hat{a}_{LL}(\cos\theta^*)$ for longitudinally polarized partons scattering at c.m. angle θ^*]. At LO, $\hat{a}_{LL}$ for gluon Compton scattering approaches unity at $\cos\theta^* = -1$, *i.e.*, when the γ is detected in the direction of the incident quark (where the cross section for the process is also maximized) [8]. Large quark polarizations ($\gtrsim 30\%$) are available at momentum fractions $x_{quark} \gtrsim 0.2$ [4] to probe ΔG. It is then highly desirable to sample very asymmetric partonic collisions ($x_q \geq 0.2$ with $x_g \leq 0.1$), in which both products will be boosted forward in the lab frame. **Coverage for such asymmetric collisions requires the EEMC proposed for STAR,** which then also spans the appropriate range of θ^*, where the spin correlation is large.

3) **Detection of γ-jet coincidences allows event-by-event kinematic reconstruction of the momentum fractions $x_{1,2}$ for the colliding partons.** It is this coincidence detection involving jets that requires the large acceptance of STAR (as opposed to the PHENIX detector at RHIC) and that facilitates the *direct* extraction of $\Delta G(x)$ from the data. The combination of coincidence and polarization measurements also considerably reduces sensitivity [3] to a problem that has plagued the extraction of *unpolarized* gluon distributions from direct photon cross sections [10], namely, kinematic smearing arising from apparently significant *transverse* components (k_T) of the initial parton momenta.

4) **Measurements with STAR plus EEMC will cover a suitably broad range of momentum fractions, $0.01 \lesssim x_g \lesssim 0.3$, to determine the integral contribution of gluons to the proton helicity with a precision better than ± 0.5.** The only other contemplated experiment that could match or exceed this reach in x_g-values requires acceleration of polarized protons in the HERA collider, a major facility upgrade whose priority will not be decided for a few more years. This coverage with STAR requires the EEMC, as well as runs at two bombarding energies, $\sqrt{s} = 200$ and 500 GeV. Adequate statistical precision can be obtained with 10-week runs at each energy, at the so-called "enhanced" $\vec{p} + \vec{p}$ luminosities ($\sim 10^{32}$ cm^{-2}s^{-1}) expected to become available by 2002.

The need for the EEMC is illustrated by simulation results in Figs. 5 and 6. As described in Ref. [3], the simulations employed an event generator considerably more sophisticated than the event reconstruction algorithm, which was designed to represent the simplest approach to a direct, LO extraction of ΔG. Figure 5 plots the pseudorapidity ranges over which the photons and jets are detected for the event sample most likely to be analyzed to extract $\Delta G(x)$. These results demonstrate clearly that the endcap coverage is needed for both photons and jets, and especially at both ends of the accessible x_{gluon} range. The impact of the EEMC on the projected $\Delta G(x)$ results attainable in a 10-week run at $\sqrt{s} = 200$ GeV is illustrated in Fig. 6. The generated $\vec{p} - \vec{p}$ spin correlations in Fig. 6 decrease in magnitude with decreasing x_{gluon} because the gluon polarization $\Delta G(x)/G(x)$ input to the calculation (corresponding to the solid curve in Fig. 4) is falling. Nonetheless, the addition of the endcap allows the best measurements of gluon polarization to be made for $x_g < 0.1$. The crucial need for measurements in this region is clarified in the lower frames of Fig. 6, which compare the $\Delta G(x)$ values extracted by the simplified reconstruction algorithm with the theoretical input. The growing gluon abundance leads to a steady *increase* in $\Delta G(x_g)$ with decreasing x_g, making the lower end of the range essential to constrain the integral ΔG meaningfully.
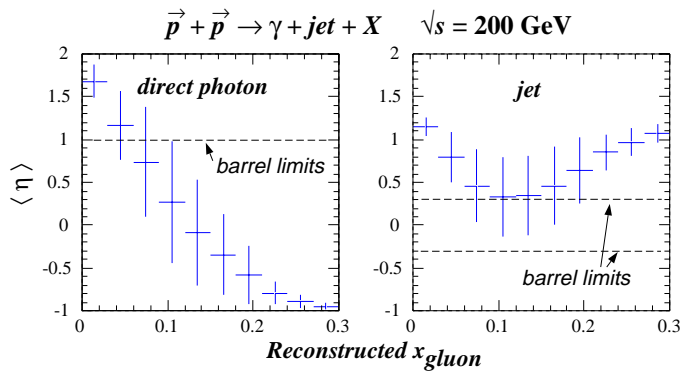
6

Figure 5: *Moments of the pseudorapidity distribution of simulated photon-jet coincidence events contributing to each bin in reconstructed x_{gluon} values. Each point represents the mean contributing η-value for γ's or jets, with the "error" bars reflecting the rms deviation from the mean. The dashed horizontal lines indicate the ends of the acceptance of the barrel EMC currently under construction. The endcap dominates the acceptance for $x_g < 0.1$ and for $x_g > 0.2$, and is of substantial importance in the intermediate region.*

The extracted values of $\Delta G(x)$ in Fig. 6 exhibit small systematic deviations from the theoretical input curve, which has been evolved to the most probable momentum transfer for the simulated events ($Q^2 = 50$ (GeV/c)^2, corresponding to $p_T = 10$ GeV/c). These deviations arise from simplifying assumptions made in the event reconstruction, *e.g.*, the neglect of the simulated contributions from k_T-smearing, from the finite resolution in determining $\cos\theta^*$, from $q\bar{q} \to \gamma g$, and from Compton scattering with $x_{gluon} > x_{quark}$. The latter effect is especially important for the nearly symmetric partonic collisions detected preferentially near mid-rapidity, but diminishes rapidly in the endcap region. Indeed, it is clear from Fig. 6 that with the EEMC, the systematic errors become unimportant at $x_g < 0.1$, where one finds the dominant contributions to the integral. Comparison of the two lower frames reveals that **the EEMC significantly expands the x_g coverage, while significantly reducing statistical and systematic errors, greatly enhancing the quality of the measurement.** The remaining deviations at larger x_g in Fig. 6 can be corrected via simulations in a way that introduces quite modest ($\sim 5\%$) model-dependence in the deduced integral.

The largest systematic error in deducing ΔG from the simulation results in Fig. 6 arises from the poorly constrained extrapolation to $x_g = 0$. The constraints will be dramatically improved by taking an additional 10-week run at $\sqrt{s} = 500$ GeV. As illustrated in Fig. 2, the higher-energy data with the EEMC extend the x_g range downward from 0.04 to 0.01. Although the input gluon polarization, and hence the simulated asymmetries, become quite small in this region, the projected extraction of $\Delta G(x)$ with STAR+EEMC is still good enough to reduce the extrapolation uncertainty *by a factor of 6*. When data from both energies are included in a fit to the reconstructed $\Delta G(x)$ values (without making any corrections for the systematic deviations noted above), using the general functional form from Ref. [7], we extract an integral $\Delta G_{recon} = 1.62 \pm 0.23$, to be compared with 1.71 ± 1.35 for a fit to the 200 GeV data alone. The error bars here include the statistical plus extrapolation uncertainties. The statistical error will be increased by a factor between 1.5 and 2.0 by the need for subtraction of background associated with π^0 and η^0 mesons that cannot be distinguished from isolated photons (see Sec. 3.2). When this and other systematic errors (most prominently from an assumed $\pm 5\%$ uncertainty on each measured beam polarization) are added in quadrature, the integral ΔG should still be determined to better than ± 0.5, as desired.

$$\vec{p} + \vec{p} \rightarrow \gamma + jet + X$$

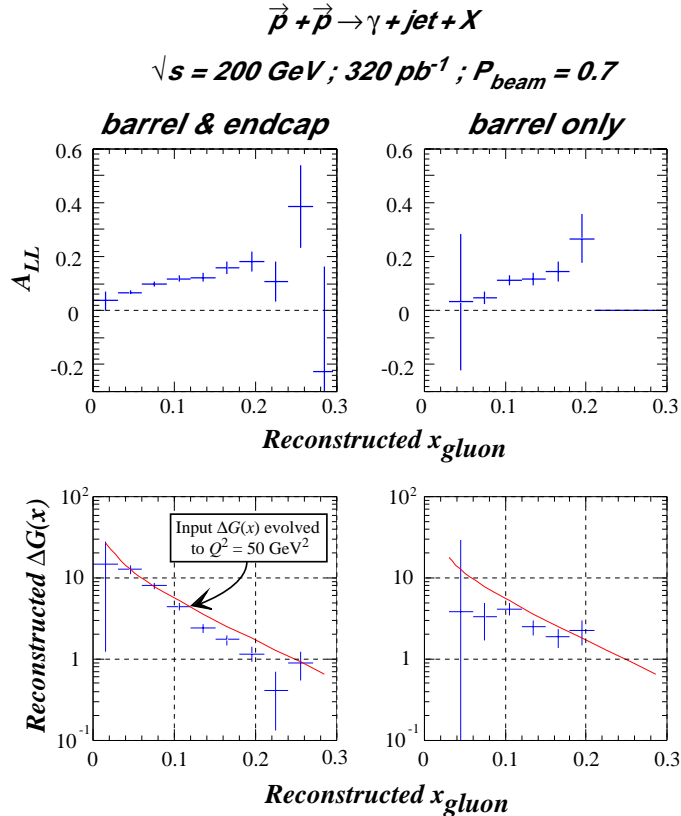$$\sqrt{s} = 200 \text{ GeV} ; 320 \text{ pb}^{-1} ; P_{beam} = 0.7$$

Figure 6: *Simulation results for the pp spin correlation A_{LL} and the gluon helicity distribution $\Delta G(x)$ extracted therefrom, for photon-jet coincidence events at $\sqrt{s}$=200 GeV. Simulations are shown for STAR with and without the proposed endcap EMC. The events analyzed have been subjected to cuts described in Ref. [3]. The error bars reflect counting statistics for an integrated luminosity of 320 pb^{-1}. The solid curves in the lower frames represent the theoretical input for $\Delta G(x, Q^2 = 50 (GeV/c)^2)$. The systematic deviations between the input and extracted gluon helicity distributions arise from simplifying assumptions in the data analysis, and are correctable via simulations, as discussed in the text.*

2.1.3 Dijet Production

Other processes that can be detected simultaneously with the direct photon production in STAR + EEMC offer complementary sensitivities to $\Delta G(x)$. For example, inclusive jet or dijet production has the advantage over photon production of much larger cross sections, but the disadvantage of several competing partonic subprocesses: both quark-gluon and gluon-gluon scattering contribute significantly [8], and will not be readily distinguishable experimentally. Furthermore, the resolution with which the colliding parton x-values can be determined is far cruder for dijet than for photon-jet coincidences. Nonetheless, models of $\Delta G(x)$ that are consistent with the photon results can be further tested by comparing their predictions to measured dijet asymmetries. Such comparisons, for two simultaneously measured channels, add a powerful internal consistency check to STAR's capabilities, because the theoretical backgrounds and the contributions of higher-order processes are likely to be quite different between the two.

Measurements of dijet asymmetries will be most useful in constraining structure function models if they span a sizable range in x_1 and x_2 values for the colliding partons and in partonic center-of-mass scattering angle, and hence in the expected *relative* contributions from *qg vs. gg* scattering. The EEMC expands the STAR acceptance for such dijet coincidences very significantly. At $p_T \sim 10$ GeV/c, a jet is typically spread over a cone of half-angle (in pseudorapidity η and azimuthal angle ϕ) $\sqrt{(\Delta\phi)^2 + (\Delta\eta)^2} \approx 0.7$, and it is desirable that both jets be fully enclosed within the detector acceptance to avoid certain systematic errors in the kinematic reconstruction of the partonic collision. As in the case of the photon-jet coincidences, the coverage gained provides critical access to (1) asymmetric partonic collisions, which will enhance the relative contribution from quark-gluon scattering, and (2) forward partonic c.m. angles, where the parton scattering cross sections grow

rapidly. Simulations show that the rate of dijet events with invariant mass above 20 GeV detected with STAR at $\sqrt{s}$=200 GeV grows by more than an order of magnitude when the EEMC is added.

2.1.4   Comparison to Other Measurements of Gluon Helicity Distributions

Measurement of the gluon spin distribution is a high-priority focus of a few approved experiments, and is under discussion at other laboratories. Among approved experiments, STAR would span the greatest range in x_{gluon}, with the smallest uncertainties, and have the only chance to make a meaningful direct determination of the integral ΔG. However, some of the experiments with more modest goals may begin taking data sooner. There is thus a sense of urgency to pursue an aggressive time schedule for completion of the EEMC.

The PHENIX collaboration at RHIC aims to extract $\Delta G(x)/G(x)$ also from direct photon detection in $\vec{p} - \vec{p}$ collisions [11]. However, their detector limits them to *singles* photon detection near mid-rapidity; the acceptance is too small for efficient jet detection. The absence of kinematic reconstructions on an event-by-event basis permits only a crude determination of the relevant x_{gluon} values, with greater sensitivity to k_T-smearing. The focus on mid-rapidity photons limits the minimum x_{gluon} value accessible to 2–3 times that possible with STAR + EEMC at the same bombarding energy. At $x_g < 0.1$ the statistical precision attainable with PHENIX is not as good as with STAR, because the dominant contributions come from lower-x, more weakly polarized quarks. Alternative reactions being considered to probe $\Delta G(x)$ with PHENIX – involving production of mesons with heavy valence quarks – are subject to greater uncertainty regarding the production mechanism and the cleanliness of the experimental signal.

The approved COMPASS experiment [12] at CERN will measure $\Delta G(x)/G(x)$ via production of charmed mesons in collisions of polarized muons with fixed polarized hydrogen and deuterium targets. Theoretical interpretability for that channel is comparably clean to the photon production at RHIC. However, COMPASS only spans the region $0.1 \lesssim x_{gluon} \lesssim 0.3$, and within that region will attain statistical precision 2–3 times poorer than STAR's measurements over the same range. Better statistics can be reached for an alternative signal based on hadron pairs, meant to indicate production of two jets. But at the CERN energies, this approach has interpretation uncertainties arising from LO background processes not involving gluons and from the fragmentation functions relating the detected hadrons to the supposed parent partons. The difficulties noted for COMPASS become more severe in the HERMES experiment at HERA, where the collaboration is presently using the same signals to measure gluon polarization at even higher x_g-values [13].

The contemplated experiments most competitive with STAR require a high-energy polarized electron − polarized proton collider, as is under discussion for HERA. At such a facility, dijet production in $\vec{e} - \vec{p}$ collisions, as well as detailed maps of Q^2-evolution in polarized DIS at very low x, could both provide theoretically attractive access to gluon polarization in the range $0.002 \lesssim x_{gluon} \lesssim 0.2$. The precision attainable on the deduced integral ΔG might be slightly better (± 0.2 statistical precision [14]) than with STAR. However, a decision about pursuing the technically challenging acceleration of polarized proton beams in HERA is unlikely to be made for a few more years. Hence, any ΔG experiment at such a collider would commence well after completion of the STAR measurement. An eventual comparison of ΔG results obtained by studying electromagnetic *vs.* hadronic processes over a range of Q^2 values is highly desirable, to provide important crosschecks on the validity of significant theoretical assumptions made in treating each case [14, 15].

2.2   Separating Quark and Antiquark Helicity Distributions

Another important open question about nucleon structure concerns the contribution of sea

quarks and antiquarks to the overall spin. The polarized DIS results, in the conventional interpretation (corresponding to assuming $\Delta G = 0$ in Fig. 3), suggest an appreciable helicity preference for strange sea quarks, *oppositely directed* to the proton's overall polarization. Is this conclusion valid, and if so, is the negative polarization shared by sea quarks and antiquarks alike, and by sea quarks of different flavor? Answers to these questions will contain clues to the physical origin of the sea, e.g., to the relative importance of processes in which virtual $q\overline{q}$ pairs are produced from gluons in the proton, as opposed to being associated with virtual π- or K-mesons – the Goldstone bosons which effect chiral-symmetry-breaking quark helicity reversals [16].
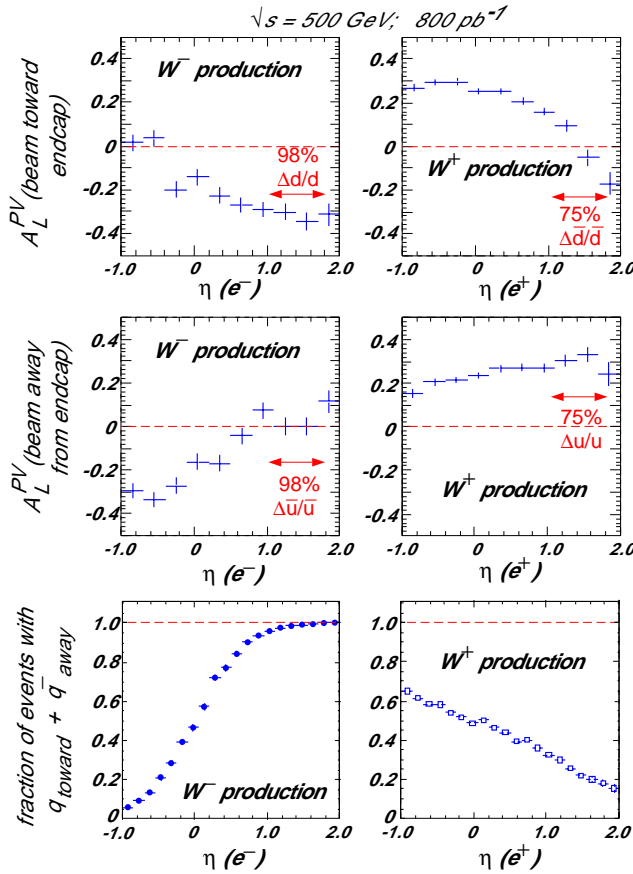

Figure 7: *Simulated single-spin parity-violating analyzing powers for W^- (left frames) and W^+ (right) production at $\sqrt{s} = 500$ GeV, plotted vs. pseudorapidity of the daughter $e^\mp$ detected in STAR + EEMC. The upper (middle) frames show the sensitivity to helicity flip of the proton beam headed toward (away from) the endcap, while the lower frames show the fraction of events where the colliding quark comes from the former beam. The averages of these fractions over the EEMC region are summarized by the percentages specified in the frames above. The error bars reflect counting statistics only, for an integrated luminosity of 800 pb^{-1}.*

In the case of u and d quarks, sea contributions can be distinguished in experiments that probe *anti*quark polarization. The cleanest antiquark probes involve Drell-Yan production of dilepton pairs or of intermediate vector bosons ($W^{\pm}$, Z^0) in $\vec{p} - \vec{p}$ collisions. The $W^{\pm}$ production is of special interest because it is flavor-specific: the dominant partonic processes, $u + \overline{d} \to W^+$ and $d + \overline{u} \to W^-$, allow independent measurements of $\overline{d}$ and $\overline{u}$ polarization. Because the weak production is parity-violating, one can sample the parton polarizations via *single-spin* longitudinal analyzing powers [17]. In principle, then, it becomes possible to determine the relevant quark and antiquark polarizations *separately* from the same data sample, by separately measuring the sensitivity to helicity reversal of the two colliding beams. Where possible, this separation allows a powerful calibration of the analysis, and indeed, of the overall RHIC spin program, against DIS by a direct measurement of quark polarization at x_{quark} values where the spin-dependent PDF's are already very well constrained by DIS. Such a comparison can verify not only the method used to extract the poorly known *anti*quark polarizations, but also the continuing validity of the Standard Model

for describing parity violation in weak processes at high p_T [8].

In practice, **separation of the quark ($\Delta q/q$) and antiquark ($\Delta\bar{q}/\bar{q}$) polarization sensitivities works best for W^- production, and requires acceptance in the EEMC region,** as illustrated in Fig. 7. $W^\pm$ production will be identified in STAR by detecting an isolated high-p_T electron (or positron) from the W decay, in events characterized by large missing p_T (corresponding to an undetected daughter neutrino) in the azimuthal region opposite the electron. The $e^{-(+)}$ are emitted preferentially parallel (antiparallel) to the left-handed $W^{-(+)}$ momentum direction. Hence, electrons detected in the endcap preferentially sample W^- produced in asymmetric $d\bar{u}$ collisions, which move toward the endcap themselves. In this kinematic regime, the structure functions strongly favor assignment of the d quark (at relatively high x, see Fig. 8) to the beam proton headed toward the endcap and of the (low-x) $\bar{u}$ to the other proton. As shown in Fig. 7, contributions from the two possible assignments are much more balanced in the W^+ case. Figure 7 indicates the statistical precisions attainable for the various parity-violating asymmetries with STAR + EEMC, and the values expected for one particular choice of the $\Delta q(x)$ and $\Delta\bar{q}(x)$ [7] (see also Refs. [17, 18]).
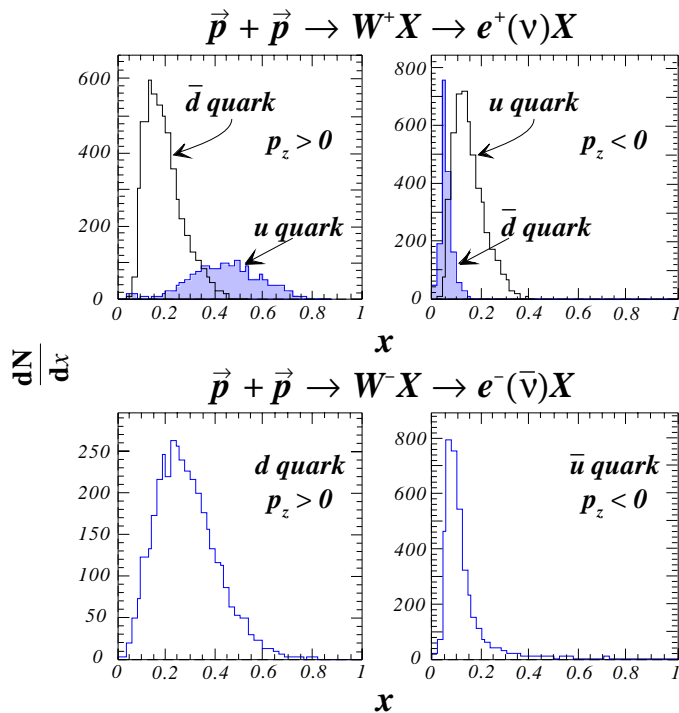
Figure 8: *The distribution of x-values for quarks and antiquarks probed by $W^\pm$ production yielding $e^\pm$ in the EMC endcap. In the W^- case, beam a yields the d quark and beam b the $\bar{u}$ 98% of the time, so the distributions for the alternative assignment are not shown. Results for both contributions are shown for W^+. The differences between $W^\pm$ results arise because the W is produced left-handed in each case, leading to preferential emission of electrons (positrons) parallel (antiparallel) to the W^- (W^+) direction.*

Measurements of $W^\pm$ production require good electron-hadron discrimination with STAR, as discussed further in Sec. 3.3. The performance expected with the proposed design is suitable. On the other hand, clean distinction of W^+ from W^- events will become problematic for $\eta > 1.5$, where STAR's time projection chamber (TPC) provides very limited resolution to discern the sign of the curvature of the very rigid $e^\pm$ tracks of interest. This issue is discussed further in Ref. [3].

2.3 Other Research Enhanced by the Endcap Calorimeter

2.3.1 Spin-Dependent Fragmentation Functions in Hyperon Production

Tests of spin substructure models can be extended, in principle, beyond nucleons to short-lived hadrons, if one can measure the polarization of such hadrons when they appear as substantial

fragments of a partonic jet. The case considered most extensively to date [19] is that of the Λ hyperon, whose weak parity-violating decay provides a self-analysis of the Λ's polarization. By measuring the polarization transfer at RHIC from one longitudinally polarized proton beam to Λ's produced inclusively at high p_T, one gains sensitivity to the *polarized fragmentation functions* for the Λ [19]. These functions measure the difference in probabilities for a parton of given helicity to fragment into a Λ of the same *vs.* opposite helicity. The functions depend on the flavor and mass scale of the final-state parton, and on the fraction z of the parton's momentum carried by the Λ. As pointed out recently by de Florian *et al.* [19], existing LEP data on fragmentation into polarized Λ's at the Z^0 resonance provide little constraint on the flavor-dependence of the polarized fragmentation functions, whereas RHIC measurements for the inclusive process $\vec{p}p \to \vec{\Lambda}X$ at $\sqrt{s} = 200$ or 500 GeV could distinguish clearly among possible scenarios. RHIC data for this process could thus elucidate whether the nucleon "spin puzzle" has an analog in the hyperon sector as well [20].

The STAR detector with the proposed EEMC is well suited for the relevant measurements. The pseudorapidity range $\eta_\Lambda \gtrsim 1$ yields the greatest sensitivity to the polarized fragmentation functions [19], simply because this region emphasizes asymmetric parton collisions where the polarized proton beam headed toward the endcap is most likely to contribute a highly polarized (valence) quark. The EEMC is needed to trigger on high-p_T jets in this region, while STAR's time projection chamber (TPC) will permit reconstruction of the Λ (and direct measurement of its longitudinal polarization and of its jet momentum fraction z) from its daughter proton and π^- tracks. At $p_T \sim 10$ GeV/c and $\eta \lesssim 1.5$, there is a high probability that the Λ will decay well within the active TPC volume. The EEMC would also serve another purpose important to interpret the results: by detecting correlated few-GeV γ's and π^0's, it could be used to tag Λ's that result from the decay of heavier hyperons ($\Sigma^0 \to \Lambda\gamma$ or $\Xi^0 \to \Lambda\pi^0$), to distinguish them from direct fragmentation Λ's. These different samples are likely to have quite different spin-dependent fragmentation functions, because the Λ *vs.* heavier hyperon wave functions have quite different internal quark spin coupling.

2.3.2 Searches for Physics Beyond the Standard Model

An exciting possibility at RHIC is to use parity violation in hard jet production to probe potential new interactions of very short range, beyond the Standard Model (SM). Parity violation does arise within the SM for quark-quark scattering, from interference between gluon- and Z^0-exchange. Predictions [21] for the resulting two-spin asymmetries (measuring sensitivity of the cross section to the simultaneous flip of both beam helicities) for jet production reveal SM effects $\gtrsim 1\%$ at $p_T > 50$ GeV/c. However, such hard collisions may also be sensitive to interference with amplitudes associated with new phenomena at a mass scale $\gtrsim 1$ TeV. Calculations have been performed [21] for two such classes of phenomena, associated either with quark compositeness or with a new heavy "leptophobic" Z' boson. The present limits on these phenomena still allow modifications to the parity-violating asymmetries that are several to many times larger than the uncertainties in the SM predictions arising from spin-dependent structure function ambiguities. With realistic measurement uncertainties, STAR $\vec{p}+\vec{p}$ experiments should attain sensitivities at $\sqrt{s} = 500$ GeV comparable to the best that can be reached in 2 TeV unpolarized $\bar{p}p$ collisions at the Tevatron [21]. The EEMC will provide an important increase in jet acceptance and, hence, in statistical sensitivity attainable, even for such high-p_T jets, because quark-quark scattering is very strongly forward-peaked in the partonic c.m. system [8].

2.3.3 Single-Spin Transverse Asymmetries

Sensitivity of the partonic processes to *transverse* polarization of one of the colliding beams

is not prohibited by parity conservation, as in the case of longitudinal polarization, but is rather suppressed by the chiral symmetry of QCD [22]. The mass terms in the QCD Lagrangian explicitly violate chiral symmetry, and can give transverse spin analyzing powers (A_T) of order m_q/p_T. For hard processes involving light quarks at RHIC energies, one expects vanishingly small A_T in leading-order perturbative QCD. It is important, at an early stage in the RHIC spin program, to test the assumed validity of perturbative QCD in the kinematic regimes of interest for the experiments described above, by measuring A_T for at least some of the processes considered. These measurements involve similar detection issues, and the same needs for the EEMC, as discussed for extraction of parton helicity distributions.

2.3.4 Quark Transversity Distributions in the Proton

Even if all the parton helicity distributions could be mapped out, we would still not have a complete picture of the nucleon's spin substructure. New and independent information is contained in the *transversity* distributions $\delta q(x, Q^2)$, which measure the difference in probabilities for finding quarks with spin orientation parallel *vs.* antiparallel to the spin of a *transversely* polarized nucleon [23, 24]. (There can be no transversity for the spin-one gluon). When expressed in a helicity basis, $\delta q(x, Q^2)$ is related to the probability of helicity flip between the emission of a quark by the nucleon and the reabsorption of a quark by the nucleon. It is expected to differ from the helicity distribution $\Delta q(x, Q^2)$ by virtue of the relativistic behavior of the quarks in the nucleon. The availability of transversely polarized proton beams at RHIC raises several possibilities for probing these so far unknown structure functions in leading-twist processes. Among the suggested approaches [24] for which STAR is particularly well suited are: transverse spin correlations (A_{TT}) in $\vec{p}_\perp \vec{p}_\perp \rightarrow Z^0 X \rightarrow e^+e^- X$; comparison of A_{TT} to A_{LL} for inclusive jet or dijet production; measurement of three-fold correlations of the form $(\vec{k}_{\pi^+} \times \vec{k}_{\pi^-}) \cdot \vec{S}_p$ in the process $p\vec{p}_\perp \rightarrow jet + X \rightarrow \pi^+\pi^- X$, with one transversely polarized beam and fragmentation pion pairs near the ρ-meson in invariant mass [25]. Each method has difficulties [24], not least of which is that it probes the product of a quark transversity function with another as yet unknown distribution. In any case, however, the addition of the endcap, by significantly expanding coverage for Z^0 and dijet events, places STAR in a good position to contribute meaningfully to transversity measurements as the subject matures.

2.3.5 The Unpolarized Gluon Distribution in Nuclei

Simulations of the early stage of ultra-relativistic nucleus-nucleus collisions indicate that gluons at low Bjorken x make the dominant contributions to the energy density of the system produced at mid-rapidity, and thus have strong influence on predicted signatures of the transition to a quark-gluon plasma (QGP) [26]. At the relevant x-values, the (unpolarized) distribution of gluons inside a nucleus may be strongly affected by "shadowing" [27]. The extent of shadowing must be measured in order to remove substantial ambiguities in present theoretical predictions of QGP signatures. Some information on the gluon structure function in nuclei is provided by the NMC experiment at CERN and by Fermilab experiments E665, E706, E772 and E789. However, the available data in the region of greatest interest $(0.01 < x_g < 0.05)$ tends to be limited either by systematic errors or by low statistics.

STAR with the endcap EMC can measure the relevant gluon densities via direct photon and jet production in unpolarized p + A collisions. It is most desirable to use the well understood quark distributions in the proton at $x_q > 0.1$ to probe the low-x gluons in the nucleus. Just as described above for the p-p case, the acceptance for such asymmetric partonic collisions relies primarily on detection of energetic photons or jets (at least in part) in the endcap. The results will have intrinsic

interest in testing our understanding of partonic interactions in nuclear matter, and will provide essential support for the interpretation of nucleus-nucleus collision data obtained at RHIC.

2.3.6 Polarized Gluon Distribution in the Neutron

It would clearly be of great interest to complement the measurements of gluon and antiquark helicity preferences in a longitudinally polarized proton with similar measurements for a polarized neutron. Such measurements may be feasible in a second generation of STAR spin experiments, if polarized ^{3}He beams can be successfully produced and accelerated at RHIC. Polarized deuteron beams would be difficult to handle, because the small magnetic moment demands unreasonably strong Siberian Snakes and spin rotators. However, the ^{3}He option appears to be a promising path for a future upgrade. The effects of depolarizing resonances for ^{3}He beams are currently being evaluated [28]. The maximum energy attainable for ^{3}He, ≈ 160 GeV/nucleon, would limit the feasibility of W production experiments, but would be quite suitable for direct photon production.

3 Requirements on EEMC Performance

For reference in subsequent subsections, it is useful to review the major subsystems of the STAR detector very briefly. STAR is housed inside a cylindrically symmetric room temperature solenoidal magnet with a 0.5 T field, as shown in the quarter section of Fig. 1. At its heart is a time projection chamber (TPC) that provides tracking and momentum analysis for many charged particles simultaneously, over the nominal pseudorapidity range $-2 \leq \eta \leq +2$ (15.4° to 164.6°). Typical electron drift times over the 2 m from the central plane to the endplanes of the TPC are 40 μs. The TPC momentum measurements provide STAR's only determination of charged hadron energies. Electromagnetic energy is measured primarily by calorimetry. The Barrel Electromagnetic Calorimeter (BEMC), presently under construction, is a Pb/scintillator sampling calorimeter $\sim$18 radiation lengths deep covering $-1 \leq \eta \leq +1$. It is the last detector layer before the magnet coils and includes a gaseous shower maximum detector (SMD) of moderate position resolution for γ/π^0 separation and e/hadron separation. Additional tracking is provided by a silicon vertex tracker (SVT) placed immediately around the beam pipe. The Central Trigger (scintillator) Barrel (CTB), located just outside the TPC and covering -1$\leq \eta \leq$1, is used for triggering. After a planned upgrade, the latter will also provide high-resolution time-of-flight information for improved hadron particle identification. Additional triggering capability on charged particle multiplicities in the region $1 \leq |\eta| \leq 2$ is provided by the multiwire chambers (MWC) in the endplanes of the TPC. The EEMC we are proposing would cover **one** poletip region of STAR.

The EEMC must have the following basic properties to meet the physics goals outlined above. It must cover the forward solid angle as fully as possible for $1 \lesssim \eta \leq 2$, within the space constraints imposed by the rest of the STAR detector. It must be thick enough to measure the energy of electrons and photons over a wide dynamic range, from < 1 GeV to > 100 GeV, with good resolution and a high degree of linearity. The segmentation must be sufficient to allow clean triggering on isolated high-energy photons or electrons, and to avoid significant multiple particle occupancy of the finest segments in $p - p$ and $p - A$ collisions. The physics demands place a high premium on γ *vs.* π^0 and electron *vs.* hadron discrimination. The detector response must be fast enough to permit easy distinction of particles arriving from different beam crossings (110 ns apart at RHIC). And the EEMC should provide position information for electrons and positrons with sufficient resolution to permit unambiguous matching to the corresponding charged-particle tracks in the TPC, even in the presence of pileup TPC tracks from hundreds of neighboring beam crossings. In the following subsections, we document in more detail the requirements we have considered in converging on an EEMC design.

3.1 Depth, Energy Resolution and Linearity

In order to accomplish the outlined physics program, the highest-energy particles for which the EEMC must provide reliable energy measurements are the electrons and positrons from $W^{\pm}$ decay. These extend up to $p_T = 40$ GeV/c, but will be superimposed on a hadronic background (discussed further in Sec. 3.3) that extends considerably further. In order to determine the background shape, one must detect electrons up to at least $p_T = 50$ GeV/c and $\eta = 1.75$, corresponding to 150 GeV $e^{\pm}$ impinging on the calorimeter. In order to identify the $W^{\pm}$ production signal clearly, it is important to see its sharp edge at $p_T = 40$ GeV/c, with an energy resolution (σ) no worse than 5%, and an even better absolute energy accuracy. These requirements suggest that the EEMC towers should contain at least 90% of the full electromagnetic showers even for 150 GeV electrons. To meet the shower containment criterion, we need a total calorimeter depth of at least 20 radiation lengths.

A calorimeter that meets the shower containment and energy resolution requirements for $W^\pm$ production will also satisfy the demands from direct photon production. The simulations in Figs. 2, 5 and 6 include direct photons in the range $10 \leq p_T \leq 20$ GeV/c. For these events, the dominant fraction of the statistical weight of the data is contained at photon energies below 50 GeV. Higher-energy photons are also of interest because they will allow higher p_T (hence, higher x_{gluon}) values to be probed in a run at $\sqrt{s} = 500$ GeV, thereby providing overlap in the x-ranges probed at the two bombarding energies. Comparison of $\Delta G(x)$ results from the two bombarding energies will provide important constraints on production mechanism uncertainties and on the Q^2-evolution of the gluon helicity distribution. The x-values for the colliding partons will be deduced from the measured p_T of the photon and the measured η values for the photon and its accompanying away-side jet. The instrumental resolution in measuring p_T is therefore important, and should be better than the physics contribution from k_T smearing [10], typically ~ 2 GeV/c.
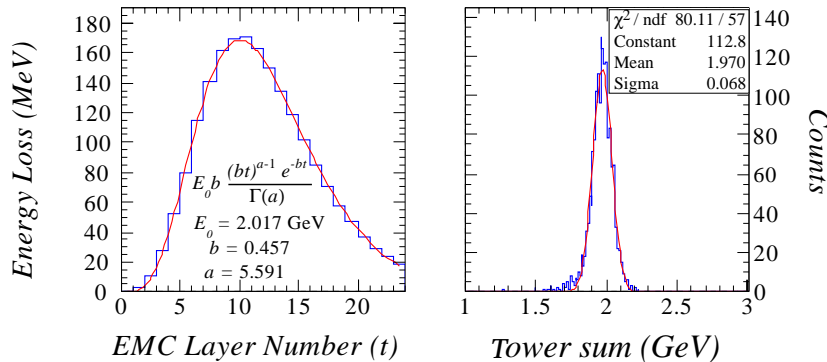
Figure 9: *GEANT simulation of the response of EEMC towers to monoenergetic 30-GeV photons, incident normally at the center of a tower. The distributions are averaged or summed over 2000 simulated events. (Left) Average energy loss in MeV within each 4-mm thick scintillator layer. The longitudinal profile is well fit by a Gamma-function distribution with the parameters shown. (Right) The event distribution of the energy deposition summed over all towers. The sampling fraction is 6.6%.*

The above performance goals will be met by the proposed EEMC design, which has, at normal incidence, towers with a total depth of 21 radiation lengths and a shower sampling fraction of 6.6%, values that closely match those used in the CDF endcap electromagnetic calorimeter [29]. The simulated energy deposition profile and total energy deposition spectrum for 30 GeV photons incident normally on this calorimeter are shown in Fig. 9. For normal incidence, the average energy leakage out the back of the endcap would be about 2% for 30 GeV photons and about 9% for 150 GeV electrons. Since the particles actually traverse the detector at an angle, they see 21.8 radiation lengths at η=2 and 27.6 radiation lengths at η=1. In addition the TPC end plates represent about 0.7 radiation length of material (on average) that must be traversed before particles reach the EEMC. Thus, the detector is suitable for the full energy range of electromagnetic showers required, while fitting within the preassigned integration volume.

We have simulated the energy resolution and linearity achievable with the proposed design, assuming that a minimum-ionizing particle (MIP) traversing a single (4 mm thick) scintillator layer will yield an average of 2 photoelectrons (pe). With this output, the energy resolution is still dominated by shower-to-shower fluctuations, rather than by photostatistics. A fit to our simulation results suggests an energy resolution $(\sigma_E/E)^2 \approx (14\%/\sqrt{E(GeV)})^2 + (2\%)^2$ over the entire relevant
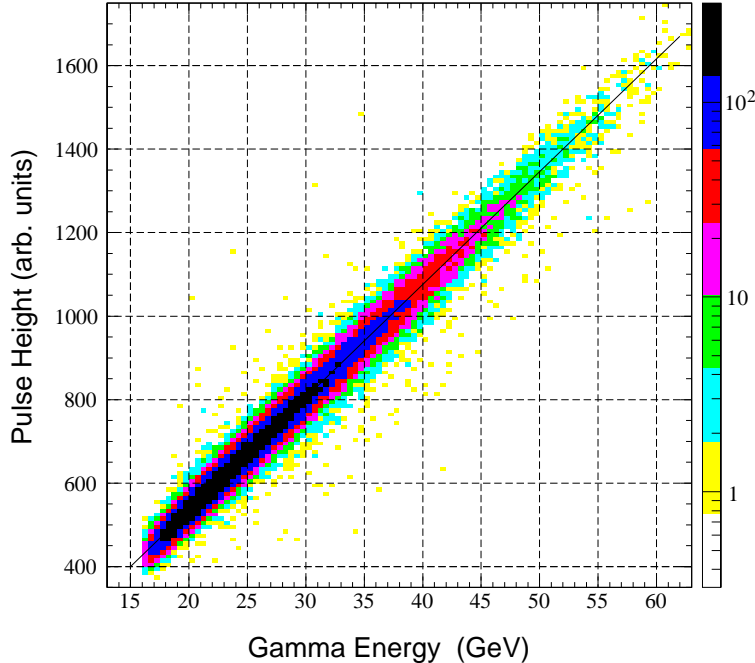
Figure 10: *Linearity of the endcap calorimeter response to photons over the energy range of interest for direct photon production at $\sqrt{s} = 200$ GeV. The simulation includes photons incident on all towers of the endcap. The pulse height reflects simulated ADC response with no corrections applied, but assuming perfect gain-matching among scintillator tiles within a given tower and accurate tower-dependent energy calibrations.*

energy range, including the effects of the longitudinal shower leakage at the upper end of the range. The energy-dependent fluctuation term will presumably be slightly worse in practice, due to effects such as tile-to-tile light output variations, which have not yet been included in the simulations. The (2%) constant term in the energy resolution is quite consistent with performance of other analogous calorimeters. The simulated linearity of the EEMC response is clearly sufficient for the ΔG measurements, as illustrated in Fig. 10. The small nonlinearity expected at the upper end of the energy range for $e^{\pm}$ from $W^{\pm}$ decay will be easily corrected to sufficient accuracy by simulations tuned to reproduce calibration measurements (see Sec. 8.2).

3.2 γ/π^0 Discrimination

A crucial issue in determining the polarized gluon structure function is the experimental distinction between directly produced photons and closely spaced photon pairs resulting from the electromagnetic decays of neutral mesons, especially π^0 and η. At the energies of interest, the most probable lab-frame opening angle between the two photons, $\phi_{\gamma\gamma}^{min} = 2\sin^{-1}(m/E)$, can be as small as 10 mrad. Furthermore, the mesons are produced with significantly larger cross sections than the direct γ's, as part of the fragmentation of hard-scattered quarks and gluons. Fortunately, the known quark and gluon fragmentation functions indicate only a small probability for a single π^0 or η to carry the majority of the momentum of the final-state parton, and even then, high-p_T mesons are generally accompanied by other charged particles or photons to form a jet. Hence, the first level of distinction between direct photons and $\pi^0(\eta)$ mesons is to apply an isolation cut, requiring minimal energy in accompanying charged particles or photons in a cone around the direct photon candidate. (The isolation cut also greatly reduces the contributions of fragmentation photons to the direct photon sample [30].) The efficacy of the isolation cuts is aided by the large acceptance of the STAR detector, but, as shown below, they are not sufficient to identify direct photons cleanly. It is therefore essential that the EEMC have a state-of-the-art shower-maximum detector (SMD)

17

to further distinguish single photons from photon pairs.

p + p √s = 200 GeV

10 GeV/c < p_T < 20 GeV/c

γ + jet in EMC; max{x_1, x_2} > 0.2
+ UA 2 isolation condition

+ cut on quality of SMD
fit to single γ

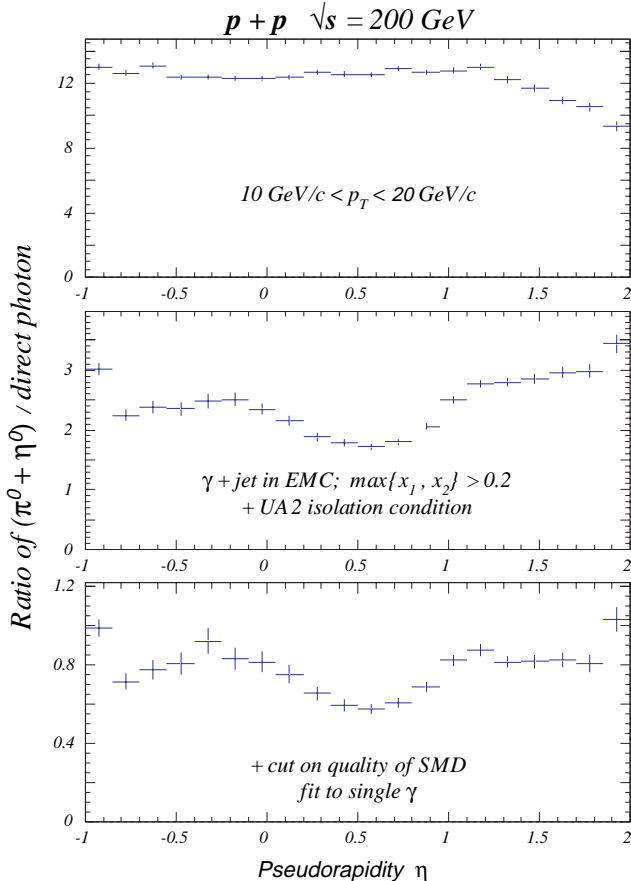*Ratio of (π⁰ + η⁰) / direct photon*

Pseudorapidity η

Figure 11: *Cross section ratio of $\pi^0(\eta)$ meson production to direct photon production in pp collisions at $\sqrt{s} = 200$ GeV, generated with PYTHIA under various conditions: (Top) limiting only the transverse momentum of the detected particle, $10 < p_T < 20$ GeV/c; (Middle) after application of conditions including an isolation cut described in the text; (Bottom) after additional application of direct meson suppression from the proposed SMD detector. For the purposes of this simulation, the SMD was placed after the fifth layer of the calorimeter, and the same type of scintillating-strip SMD (see Sec. 6) was assumed for both barrel and endcap.*

The ratio of total production cross sections for high-p_T $\pi^0(\eta)$ mesons vs. direct photons can only be estimated from data acquired with other collider detectors. Such estimates [31] suggest $\sigma_\pi : \sigma_\gamma \sim 5 : 1$ over the ranges $-1 < \eta < 2$ and $10 < p_T < 20$ GeV/c for $\sqrt{s} = 200$ GeV pp collisions, with little information on the dependence of this ratio on pseudorapidity or isolation cuts. To address these questions, we have simulated the production of π^0 and η mesons with the code PYTHIA [32], by examining all fragmentation products resulting from $2 \rightarrow 2$ partonic hard-scattering processes allowed in a pp collision. We compare this yield with that computed for direct photons, arising from $qg \rightarrow \gamma q$ (predominantly) and $q\bar{q} \rightarrow g\gamma$ or $\gamma\gamma$. The simulation result for the expected background:signal ratio is in qualitative agreement with the data extrapolation: $\sigma_\pi : \sigma_\gamma \approx 8 : 1$ and $\sigma_\eta : \sigma_\gamma \approx 4 : 1$. The variation of these ratios with pseudorapidity is small (Fig. 11). Figure 11 also illustrates the effect of an isolation cut, which reduces the net ratio from 12:1 to about 3:1, by removing 78% of the mesons *vs.* 14% of the photons. The isolation cone used (half-angle $\sqrt{(\Delta\eta)^2 + (\Delta\phi)^2} = 0.26$) was based on the UA2 analysis [33] of direct photon + jet coincidence yields in unpolarized $p\bar{p}$ collisions at $\sqrt{s}=630$ GeV. Events were rejected if they were accompanied by *any* additional charged particles or photons within this cone, independent of their energy deposition. We have not yet explored optimization of the isolation cut.

The SMD allows additional event-by-event discrimination between single photons and photon pairs on the basis of the measured transverse profile of the electromagnetic shower. In order to
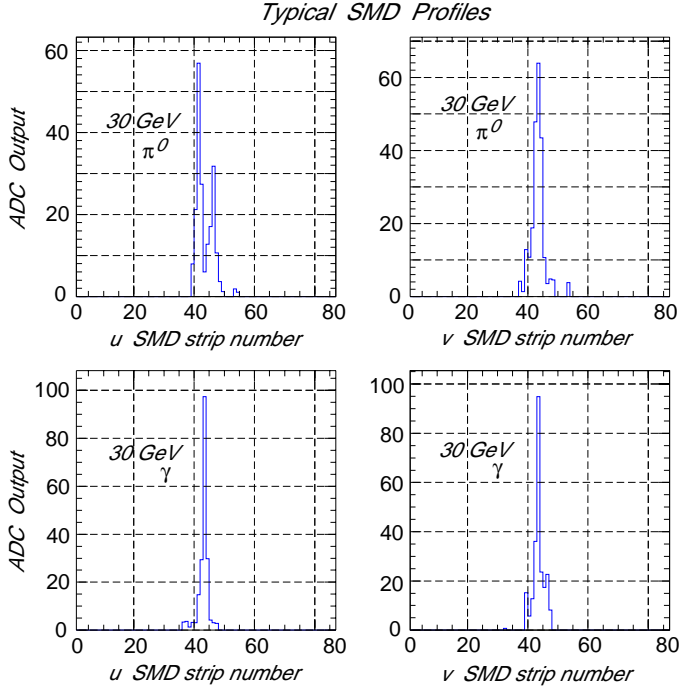
Figure 12: *Comparison of the simulated response of the SMD to a typical 30-GeV direct photon (below) and to a 30-GeV π^0 (top). The presence of the second peak in the SMD u-strip response for π^0 clearly indicates two closely spaced photons intercepted by the detector.*

reduce the hadronic background to acceptable levels, SMD cuts must be capable of reducing the π^0/γ ratio by an additional factor ≈ 4, over the entire photon energy range of interest. Experience in other detectors [34] suggests that such performance would be very difficult to achieve for 30-GeV photons with a gaseous SMD, whose response is difficult to simulate reliably. For this reason, we consider it essential to employ within the EEMC an SMD composed of scintillator strips (see Sec. 6), despite its additional cost. The response of the proposed SMD has been simulated with the code GEANT [35], assuming that the SMD is positioned after 5 radiation lengths of material within the EEMC, and that each scintillating strip generates an average of two photoelectrons per minimum-ionizing particle traversing its (maximum) depth. Typical responses for a single photon and a π^0 are illustrated in Fig. 12.

SMD discrimination against mesons is incomplete because of shower-to-shower fluctuations and very asymmetric meson decays, where one of the daughter photons has quite low energy. Optimal discrimination requires a sophisticated analysis algorithm. Here, we have made cuts (see Sec. 6.1 for details) based on the goodness of fit to the measured response with an adjustable function characteristic of the average response to single photons. This approach rejects $\approx 80\%$ of the simulated 30-GeV $\pi^0(\eta)$ events, at the expense of $\approx 20\%$ loss of single photons, a performance comparable to that achieved in experiments with the best existing collider detectors [34]. The optimal simulated discrimination is provided by an SMD built from two orthogonal planes of overlapping scintillator strips having a triangular cross section, as described in detail in Sec. 6. This design, developed as a preshower detector for the upgrade of the D0 calorimeter [36], stabilizes the lineshape of the transverse profile of the electromagnetic shower, by virtue of the sharing of energy loss between adjacent detector strips. With this design, the simulated background:signal ratio in STAR, after application of isolation and SMD cuts, is reduced to 0.6–0.8, with relatively little dependence on pseudorapidity, as shown in the last frame of Fig. 11. This background level is consistent with *running* experience with the CDF detector [34] at FNAL, if we allow for

extrapolation downward to the RHIC energies.

It is important to evaluate the effect of subtracting the remaining background contributions on the precision of information that can be extracted about the gluon polarization. Most of the information needed for this subtraction can be based on *measured* quantities, namely, on the yields (N^{pass}, N^{fail}) and spin correlation asymmetries (A_{LL}^{pass}, A_{LL}^{fail}) for those event samples that pass all cuts and that fail the final SMD cut. The only other quantity needed that is not directly measured is the probability P_m that a meson that passes all other cuts will also survive the SMD cut. In terms of these quantities, within each desired bin, the spin correlation associated with direct photon production can be extracted as follows:

$$A_{LL}^{\gamma} \;=\; A_{LL}^{pass} \;+\; \frac{(A_{LL}^{pass} - A_{LL}^{fail})}{[(\frac{N^{pass}}{N^{fail}})(P_m^{-1} - 1) - 1]}. \tag{2}$$

This equation assumes that A_{LL}^{pass} and A_{LL}^{fail} differ only because of the different mix of photon and meson events within the two samples; A_{LL}^{γ} and A_{LL}^{meson} must each have the same value within both samples, because neither the decay of spinless mesons nor the shower fluctuations can be influenced by the initial spin state of the proton beams. Our estimates of background subtraction errors in the simulated A_{LL} results are based on the above equation, with the values and statistical uncertainties of the four measured quantities determined by the simulations and an assumed uncertainty of $\pm 15\%$ in P_m (i.e., $P_m \approx 0.20 \pm 0.03$ for the present simulations). With these conditions and assumptions, the subtraction of the remaining meson background will then increase the error bars shown in Figs. 2 and 6 (which assumed no background) by a factor of 1.5–2.0, depending on the x_{gluon} range considered.

The meson SMD survival probability P_m can be extracted from simulations that have been tuned to reproduce the observed variation in the ratio N^{pass}/N^{fail} as the SMD cut is changed. Calibration of the SMD simulations will be greatly aided if the data acquired with STAR includes "tagged" samples of high-energy photons and π^0's; these should be obtainable from jets containing, respectively, π^0's that decay to two daughter photons detected in *adjacent* EEMC towers, and $\rho^{\pm} \to \pi^{\pm}\pi^0$ decays, where the π^+ momentum is deduced from the TPC. The simulations can also be constrained independently via the observed conversion probabilities in the preshower detector, within the pass and fail event samples. The preshower detector is a scintillator with good light output positioned after about one radiation length of absorber. This early in the stack, there is a significantly greater probability of conversion for (at least one of) the pair of photons from meson decay than for a single photon. Hence, the fraction of events in the pass and fail samples that are accompanied by a preshower signal is sensitive to the balance among photons and mesons within each sample. The importance of this crosscheck is likely to grow with increasing photon energy, as the discrimination power of the SMD diminishes. The above constraints appear sufficient to attain at least the assumed uncertainty of $\pm 15\%$ in P_m.

In $\vec{p}\vec{p}$ collisions at $\sqrt{s} = 500$ GeV, there is substantial physics interest in events with direct photons of energy above 50 GeV. This sample includes nearly all the direct photon production events corresponding to $x_{gluon} > 0.05$, and thus provides overlap in gluon polarization sensitivity with the $\sqrt{s} = 200$ GeV data. The overlap region will allow a powerful crosscheck on model assumptions made in extracting $\Delta G(x, Q^2)$ from the data, and may provide information on the evolution of the spin-dependent gluon distribution. The SMD will provide limited $\gamma - \pi^0$ discrimination power at such high photon energies (see Sec. 6.1). While our simulations suggest a ratio $(\pi^0 + \eta^0)/\gamma \lesssim 1$ even *without* SMD cuts at the relevant values $p_T > 20$ GeV/c, it is clear from the above discussion that the background subtraction still relies on producing two event samples with significantly different

meson-to-photon enrichments. For $E_\gamma > 50$ GeV, the *pass* and *fail* samples discussed above are likely to be replaced by ones based on a combination of SMD and preshower information. For example, for 60-GeV particles incident near the middle of the EEMC, simulations suggest that 80% (50%) of γ's (π^0's) will pass an SMD cut, while 50% (75%) of γ's (π^0's) will yield appreciable energy deposition in the first preshower layer. One could then produce a highly enriched photon sample by including events which pass the SMD cut **and** give no signal in the first preshower layer, or a highly enriched neutral meson sample via events that fail the SMD cut **and** do give a preshower signal. This combination can give background subtraction performance nearly as good as that obtained with the SMD alone near 30 GeV, *if* the preshower conversion probabilities can be calibrated as well as the SMD cuts.

3.3 Electron/Hadron Separation

The production of intermediate vector bosons will be signalled by detection of electrons and positrons at high p_T. Since the STAR detector does not provide good particle identification, the most important background for these weak signals arises from the abundant yields of charged hadrons at high p_T. As indicated by the simulated spectra in Fig. 13, the raw expected signal:background ratio within the STAR acceptance is only of order 1:30, even at the peak of the expected W decay spectrum. However, simple cuts, together with the selective response of the EMC's, appear capable of suppressing the hadronic background by several orders of magnitude, with minimal loss of W's. As illustrated in Fig. 13, one order of magnitude is gained by application of the same isolation cut discussed above for photons. A comparable, independent gain arises from a cut demanding large *missing* p_T in the event, as expected for the neutrino from W decay. The latter cut is more strictly a dijet rejection criterion, discarding events in which the e$^\pm$ candidate (at azimuthal angle ϕ) is accompanied by a jet with $p_T > 5$ GeV/c centered, within ± 1 radian, in the opposite azimuthal region, *i.e.*, $(\phi + \pi - 1, \phi + \pi + 1)$.

Additional hadron suppression is provided by the calorimeter response. The spectra in Fig. 13 are plotted against the *generated* p_T value, rather than against the transverse energy E_T that would actually be measured in the EMC. As illustrated in Fig. 14, for given p_T, the measured E_T is systematically smaller for hadrons than for electrons, so that the *observed* spectra will already be much more favorable than shown in Fig. 13. Over the η range where the TPC provides good momentum resolution, further hadron suppression can be gained by demanding a strong correlation between p_T measured in the TPC and E_T measured in the EMC, as indicated by the diagonal line in Fig. 14. Additional discrimination, applicable even for $\eta \gtrsim 1.5$, where the TPC resolution is substantially deteriorated, can be based on the ratio of energy depositions in the preshower *vs.* total calorimeter depth. The combination of these conditions based on EMC response should lead to at least another order of magnitude gain in e$^\pm/h^\pm$ ratio.

With all of the above cuts implemented, W$^\pm$ production should dominate over charged hadron production throughout the region $E_T \gtrsim 25$ GeV/c. It is important to distinguish the W's clearly over a range of E_T, because the Bjorken x-values of the colliding partons can be determined event-by-event from the combination of E_T and η of the detected e$^\pm$.

3.4 Triggering and Segmentation

The simulations presented in this proposal are based on integrated $\vec{p} + \vec{p}$ luminosities that have been established as standard values for the RHIC spin program: 320 pb^{-1} at $\sqrt{s}$=200 GeV and 800 pb^{-1} at 500 GeV. These integrated luminosities correspond to 10 weeks of running time at each energy, with roughly one third of the time lost to overhead and problems, at the ultimate
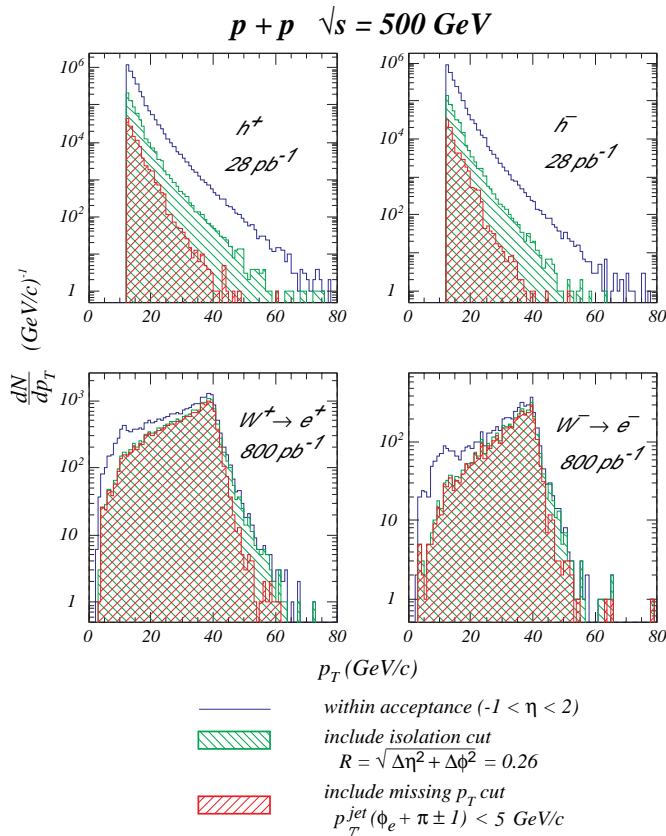
21

p + p   √s = 500 GeV

Figure 13: *Simulated (with PYTHIA) p_T spectra for positive and negative hadrons and for positrons and electrons from $W^\pm$ decay falling within the STAR + EEMC acceptance for $\sqrt{s}$=500 GeV pp collisions. The hadron spectra correspond to an integrated luminosity of 28 pb^{-1} (with a p_T cutoff of 10 GeV/c imposed in the simulations), while the W decays correspond to 800 pb^{-1}. The included hadrons are p, K^+, π^+, and e^+ from π^0 Dalitz decay, or their antiparticles. The hadron yields are plotted against the generated values of p_T, rather than against the smaller transverse energies that would be measured for them in the EMC's. The shaded and cross-hatched spectra show the results of applying first an isolation cut and then a missing p_T cut to the events, as described in the text. These two cuts leave a signal/background ratio of $\approx$ 1:2 for W^+ and 1:3 for W^- production at $p_T \approx$ 30 GeV, which can be improved by a further 1-2 orders of magnitude by cuts associated with the EMC response.*

luminosities expected for the polarized proton collisions: 8×10^{31} cm^{-2}s^{-1} at 200 GeV and 2×10^{32} cm^{-2}s^{-1} at 500 GeV. At these full luminosities, minimum-bias pp collisions will occur at total rates of $\approx$ 4 MHz and 12 MHz, respectively. In contrast, the TPC information cannot be read out at rates exceeding about 60 Hz. Thus, a fast hardware trigger must effect a large reduction in the rate of collisions processed.

The barrel and endcap EMC's will play the essential role in defining hardware triggers suitable for the spin program. The hard photons and electrons of interest can be identified relatively cleanly by their characteristic large energy deposition in a narrow region of the calorimeters. Indeed, the simplicity of the trigger logic is optimized if the majority of electromagnetic showers from single photons or $e^\pm$ are contained fully within a single calorimeter tower, while jets are spread over many such towers. Since typical shower radii (to contain 95% of the energy deposition near the depth of maximum shower development) are roughly 2 cm, this criterion places a lower limit on the desirable scintillator tile transverse dimensions of about 8 cm. A similar limit is imposed by considerations of the minimum bending radius for the optical fibers that will be used to transport light from the tiles to the tower phototubes. These minimal transverse dimensions correspond, near $\eta = 2$, to a tower acceptance of approximately 0.1 unit in η and 0.1 unit in azimuthal angle ϕ. In our proposed design, we maintain $\Delta\phi = 0.1$ for all the EEMC towers, but allow $\Delta\eta$ to evolve from 0.1 at $\eta = 2$ to about 0.05 at $\eta = 1$, yielding a total of 720 EEMC towers to cover the entire endcap acceptance.

With this segmentation, a trigger decision based on transverse energy deposition in a single
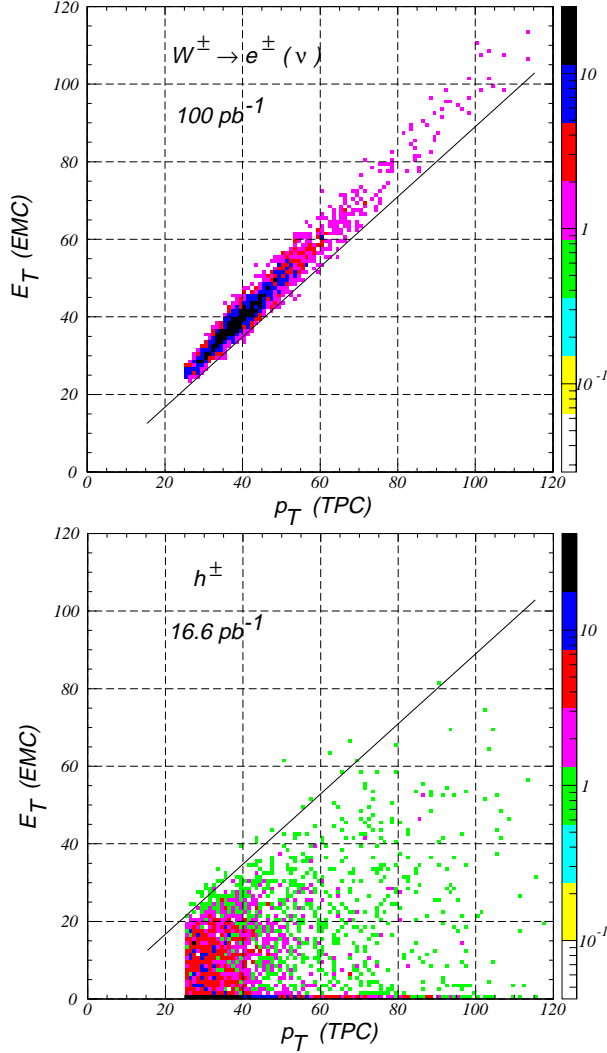
22

Figure 14: *The simulated correlations of energy measured in the EMC with momentum determined from the TPC for W decay daughters and for hadrons. The straight line represents a cut used for electron/hadron separation. The simulations included only events with $p_T > 25$ GeV/c, and do not yet take into account the serious deterioration in TPC momentum resolution at $\eta > 1$.*

calorimeter tower is quite effective. Our simulations suggest that the STAR level 0 hardware trigger rate for pp events, at the full luminosities indicated above, will be reduced to ≈ 30 Hz at $\sqrt{s} = 200$ GeV and ≈ 460 Hz at 500 GeV, simply by demanding that one or more calorimeter tower in the barrel or endcap regions register at least 5 GeV of transverse energy. Taking transverse shower leakage into account, such a trigger provides very good efficiency for recording direct photon events with $p_T \geq 10$ GeV/c. The rates can be further reduced by more than an order of magnitude by demanding, in addition, a minimum of 10 GeV transverse energy in a small (e.g., $\Delta\eta \times \Delta\phi = 0.2 \times 0.2$) patch of the calorimeter containing the single tower with the highest recorded energy, as illustrated in Fig. 15.

The above trigger would discriminate against most of the abundant dijet events, because jet energies are typically spread over a much broader patch of the calorimeter, and are concentrated in hadrons to which the calorimeter response is much weaker. Thus, a separate jet or dijet trigger will be needed. The most promising jet trigger appears to be one exploiting the correlation between two characteristics of the typical jet: localized enhancements in electromagnetic energy (as measured in the EMC's) and in charged-particle multiplicity (as measured in the Central Trigger Barrel for

23

$p+p$ $\sqrt{s} = 200$ GeV $(PYTHIA$ $5.7)$

Direct Photon Production, $\hat{p}_T > 10$ GeV/c $(9$ $pb^{-1})$

Jet Production, $\hat{p}_T > 5$ GeV/c $(0.05$ $pb^{-1})$
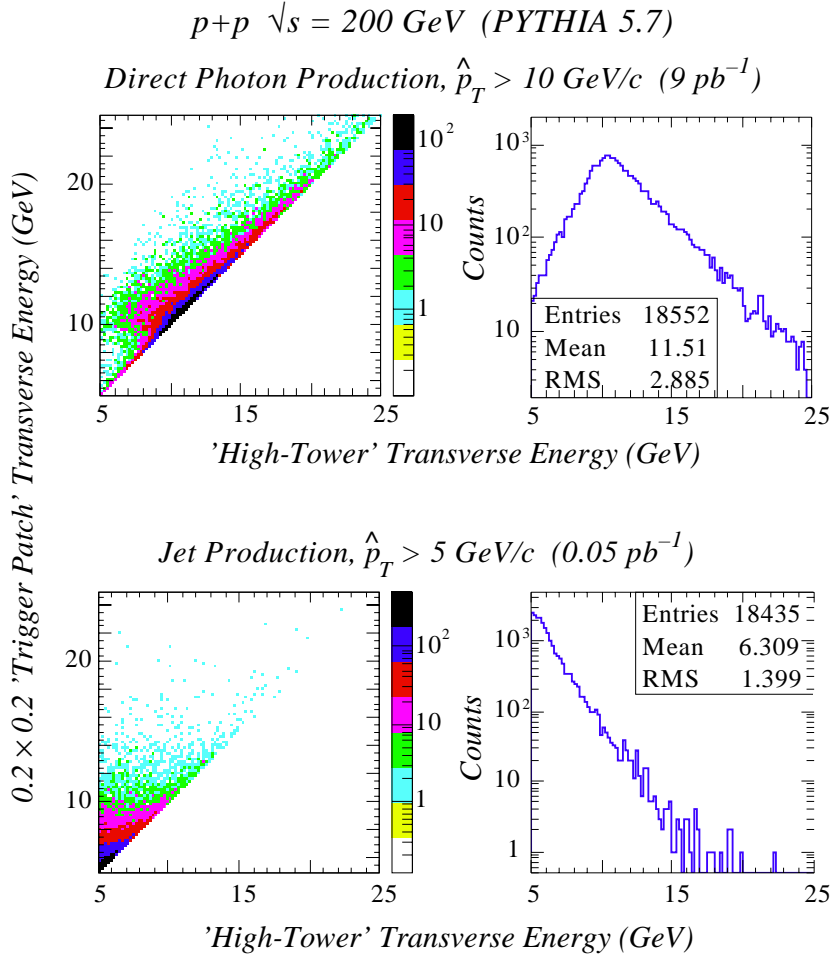
Figure 15: *Simulation results for the distribution of pp hard collision events as a function of the maximum energy deposition in a single EMC tower and the energy deposition in a $\Delta\eta \times \Delta\phi = 0.2 \times 0.2$ trigger patch containing the high single tower. The correlation between these two energies are shown in the left-hand frames, and the projected spectra for high-tower energy on the right. Only events with a minimum p_T of 10 GeV/c (5 GeV/c) at the partonic collision level were generated for the direct photon production "signal" (jet production background). A trigger requirement of 5 GeV energy deposition in the high tower and 10 GeV in the trigger patch would pass the vast majority of direct photon events of interest, while rejecting most jet events, leading to acceptable trigger rates.*

$|\eta| \leq 1$ and in the Multi-Wire Chamber at the end of the TPC for the endcap region). Correlated conditions can be imposed on these measured quantities on a patch-by-patch or sector-by-sector basis in STAR's Level 1 trigger. Preliminary simulations suggest that such correlated conditions can readily reduce the minimum-bias event rate by three orders of magnitude, while retaining trigger efficiencies well in excess of 50% for dijet events generated (with the code PYTHIA [32]) from partonic collisions at $p_T \geq 10$ GeV/c. Further background trigger rate reductions could be effected (also at Level 1) by requiring jet-like clusters in two detector patches at roughly opposite ϕ-values. The resulting rates would be acceptable for early dijet runs at reduced $\bar{p}p$ luminosities. However, at the enhanced luminosities needed for the photon and W production programs, dijet trigger rates will have to be reduced further, for example, by prescaling those triggers corresponding to the relatively abundant dijets near the lower end of the accepted p_T range.

The proposed EEMC segmentation into 720 projective towers ensures low occupancy for the tens of products expected for typical $p - p$ and $p - A$ collisions. In contrast, the typical tower occupancy will be substantial for central Au-Au collisions. However, the envisioned usage of the EEMC for A-A experiments will be confined to providing information on coarse energy deposition (e.g., from an anomalous multiplicity of π^0's) summed over extended regions in η and ϕ, so that the segmentation is still deemed adequate.

3.5 Contribution to Jet Identification

Jets are identified operationally as clusters of particles depositing large cumulative transverse energy E_T in a confined solid angle. For the purpose of simulations reported here, we have considered jet cones of half-angle $\sqrt{(\Delta\eta)^2 + (\Delta\phi)^2} = 0.7$, and required a minimum jet energy of 5 GeV [37]. Fluctuations in jet characteristics make their absolute cross sections sensitive to these parameters, but as long as the fluctuations are spin-independent, polarization observables should not exhibit similar sensitivity to details of jet identification. It is the substantial cone angle that makes the large acceptance of the STAR detector so essential for jet reconstruction.

While STAR does not have a hadron calorimeter, the momentum of charged hadrons within the jet can be determined with comparable resolution from the TPC tracks, whereas that of neutral hadrons that decay electromagnetically will be determined from the barrel and endcap EMC's. Corrections will have to be applied for the unmeasured momentum of other neutral hadron (n, $\bar{n}$, K_L) components. Appreciable uncertainties in jet momentum determination arise from fluctuations in the fraction of momentum carried by such undetected particles (including also those falling within gaps in the EMC coverage) and, especially in the endcap region, from the TPC resolution. However, these STAR-specific resolution contributions remain significantly smaller than a fundamental limit imposed by the physics of parton fragmentation: even with perfect detector resolution, events generated with PYTHIA exhibit a 30% (FWHM) spread in the correlation of jet energy with that of a single final-state parton in the hard collision (see Fig. 16).

It is important to emphasize, however, that the jet momentum is not necessary to reconstruct the Bjorken x-values of the colliding partons for each γ-jet coincidence event. For this purpose, it is sufficient to use the central jet *direction* (i.e., pseudorapidity η_{jet}), which is determined with much better resolution than the momentum (see Fig. 17), and has a more direct connection to the behavior of a single parton. In particular, if we assume two-parton kinematics, neglecting any *transverse* momentum of the colliding partons in the initial state, then we have:

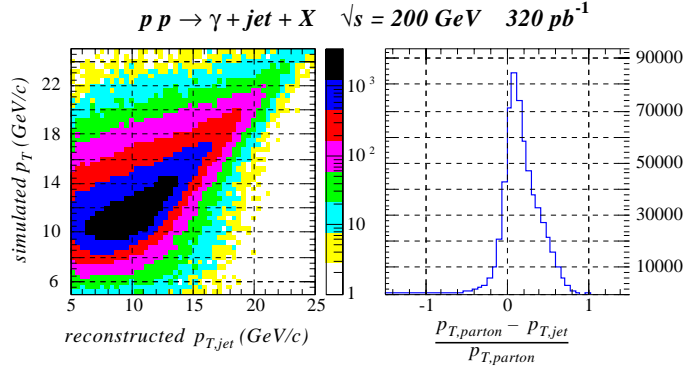$$x_{1(2)} = \frac{p_T(\gamma)}{\sqrt{s_{pp}}}[\exp(\pm\eta_\gamma) + \exp(\pm\eta_{\text{jet}})]; \tag{3}$$

Figure 16: *Comparison of reconstructed jet momentum with generated parton momentum in simulations of direct photon production at $\sqrt{s} = 200$ GeV. Events are selected by requiring a photon with $10 < p_T < 20$ GeV, satisfying the UA2 isolation cut for the photon. The accuracy of the UA1 jet finder reconstruction is determined by comparing p_T for the recoiling parton in the $2 \rightarrow 2$ LO QCD photon production process to the reconstructed jet p_T. For events where more than one jet is identified, the comparison is made to the highest p_T jet.*

$$|\cot\theta^*| = |\sinh(\frac{\eta_{\text{jet}} - \eta_\gamma}{2})|, \tag{4}$$

where we use the (EMC) momentum measurement for the photon only, and θ^* is the photon angle with respect to the incident quark in the partonic c.m. frame. The resolution of the above reconstruction is typically $\delta x_{1(2)} \simeq 0.02$ (FWHM). The corresponding resolution is quite a bit worse for dijet events, since there we must rely on p_T measurements for the jets.

3.6 Calibration Precision and Dynamic Range

Systematic errors in the x-values reconstructed for the colliding partons, *e.g.*, via eq. (3), give rise to systematic errors in the extracted spin structure information. The reliance of the x-values on p_T measurements for photons or very energetic $e^\pm$ (where the TPC resolution is limited) thus places a high premium on the absolute energy calibration of the EMC response. We have assessed the accuracy level needed by reanalyzing the simulated photon-jet coincidence events with the introduction of a $\pm 5\%$ miscalibration of the EEMC energy scale. We have then fitted the extracted $\Delta G(x)$ values, like those in Fig. 2, with the functional form used in the Gerhmann-Stirling [7] curves in Fig. 4. This procedure allows us to evaluate the effect of miscalibration on the inferred integral ΔG. When simulated results from both 200 and 500 GeV runs are included, a 5% miscalibration introduces a $\approx 10\%$ change in the integral. Thus, in order to keep the energy calibration effect smaller than the (probably dominant) $\pm 10\%$ systematic error expected from the absolute calibration of the beam polarization at RHIC, it is important to plan for an energy calibration to $\pm 2 - 3\%$. The measurement of differential cross sections falling rapidly with increasing p_T imposes a similar limit [38].

The calibration requirement is not beyond the state of the art for similar calorimeters, which seems to be $\approx 1\%$ [33, 34]. However, it has significant implications for electronics and run procedures. It is extremely useful for calibration purposes to keep the peak for minimum-ionizing particles (which will deposit ~ 20 MeV in a typical tower) within the spectrum for each tower during data-taking. This requires a minimum of 12-bit ADC ranges for the towers. Calibration

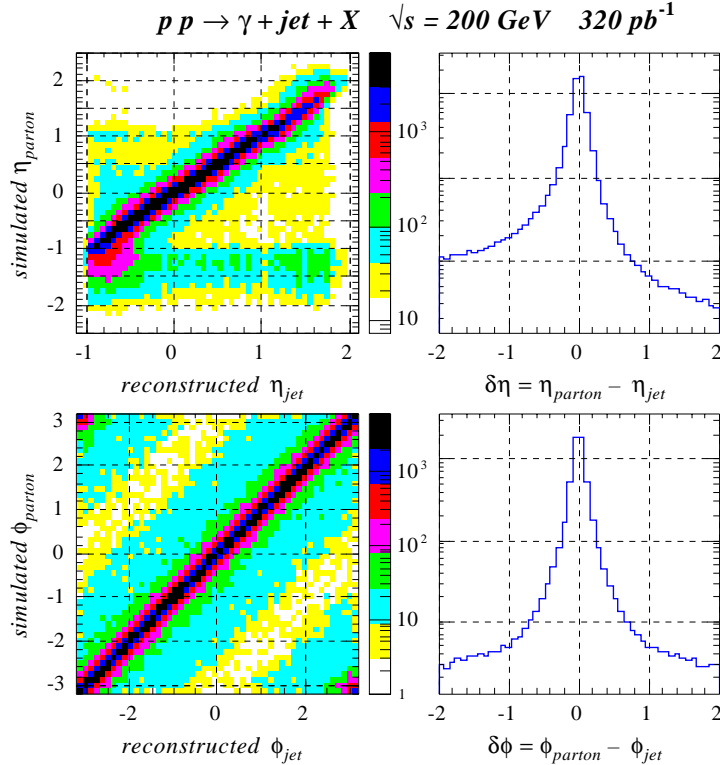**$p\,p \to \gamma + jet + X$ $\sqrt{s} = 200\ GeV$ $320\ pb^{-1}$**

Figure 17: *Comparison of reconstructed jet direction with generated parton direction in simulations of direct photon production at $\sqrt{s} = 200$ GeV. Events are selected by requiring a photon with $10 < p_T < 20$ GeV, satisfying the UA2 isolation cut for the photon. The accuracy of the UA1 jet finder reconstruction is determined by comparing η and ϕ for the recoiling parton in the $2 \rightarrow 2$ LO QCD photon production process to the reconstructed jet values. For events where more than one jet is identified, the comparison is made to the highest p_T jet. When the recoiling parton is beyond the acceptance of the barrel or endcap EMC (e.g., at $\eta < -1$), the highest-p_T jet is often uncorrelated with the generated parton.*

points at higher energies can be provided during STAR data acquisition by tying the EEMC response for electrons and positrons to the corresponding momenta measured in the TPC. However, the deteriorating TPC resolution will impose an η-dependent upper limit on the p_T values at which such cross-calibrations can be effectively performed (*e.g.*, $\approx 5-10$ GeV/c for $\eta = 1.5$). Calibrations above this effective limit can be accomplished by reconstructing correct invariant masses for decays such as $J/\Psi \to e^+e^-$, $\rho^\pm \to \pi^\pm\pi^0$ and $Z^0 \to e^+e^-$, where the momentum of the coincident decay daughter can be measured well by the TPC or by otherwise calibrated portions of the EMC. Some of these decay calibrations might require dedicated running with specialized triggers. In addition to these calibrations *during* production running, it is clearly important, via cosmic ray and test beam results, to provide a sufficiently good calibration *beforehand* to set the ADC range and trigger thresholds appropriately. Transfer of test-beam calibrations to the final calorimeter configuration will require incorporation of some form of radioactive source or light-pulsing system within the EEMC. The details of all these calibration needs are under continuing study.

Calibration points over a very wide range of pulse heights will be needed to establish the linearity of the calorimeter response over the range of energies needed for the physics program. This range runs from few hundred MeV photons from asymmetric π^0 decays (also needed to monitor few percent leakage of 10 GeV photon showers into neighboring calorimeter towers) through 150 GeV electrons ($p_T = 40$ GeV/c at $\eta = 2$) from W^- decay. The simulation results in Fig. 10 demonstrate at least that the calorimeter design yields a quite linear response over the energy range of interest for direct photon production at 200 GeV. The high degree of linearity observed in Fig. 10, for events spanning the entire area of the endcap, arises in part from compensating dependences of the sampling fraction on photon energy and on angle of incidence. We will have to make corrections

for expected nonlinearities at higher energies, arising from shower leakage out the back of the EEMC ($\approx$ 8% at 150 GeV and $\eta = 2$). Of course, nonlinearities can be introduced as well by gain mismatches among different scintillating tiles within a given tower or in the electronics, and these effects have been neglected in the simulations to date.

The presently envisioned use of the SMD is to enable a shower-shape analysis to discriminate between showers in a single EEMC tower produced by *single photons* and those produced by closely spaced *photon pairs*, arising from the decay of energetic $\pi^0(\eta^0)$ mesons. As well, a shower-shape analysis can aid in the distinction between $e^\pm$ and charged hadrons. Typical showers produced by charged hadrons have a larger transverse extent than do showers produced by $e^\pm$ of the same energy. That distinction is important for the clean detection of $e^\pm$ daughters arising from the decay of the J/ψ meson, the $W^\pm$, the Z^0 or heavy quarks (charm and bottom). A feature of the shower-shape analysis is that the overall energy deposition within the SMD planes does not need to be accurately determined. Simulation studies have determined that *random variations* of the readout gains of individual strips can be as large as $\sim$30% without compromising the discrimination between γ and $\pi^0(\eta^0)$ deduced from the shower-shape analysis. *Systematic* differences of the readout gains of *adjacent* SMD strips must be kept below $\sim$10%, since more sizable differences can mimic the discontinuities in the distribution of deposited energy versus strip number that signals the presence of a second shower. It is expected that this accuracy of the individual strip gain calibration can be met using minimum-ionizing particles (MIP's) and photon-induced showers, for photons produced by the decay of low-energy π^0, where the two photons are detected in separate EEMC towers. Other applications of the SMD, presently not envisioned, may impose more severe calibration requirements.

The required calibration of the preshower-scintillator readout is to determine the distribution of pulse magnitudes and the detection probability when a MIP is incident on the detector. For either $\gamma/\pi^0(\eta^0)$ or $e^\pm/h^\pm$ discrimination, the preshower detector will provide two different event samples: those with two or more MIP's, and those with either no particles or a single MIP, passing through the scintillator. Hence, one relevant calibration of the preshower detector is provided by carefully measuring its response to single MIP's, provided by energetic charged hadrons that do not shower in the EEMC. For γ/π^0 discrimination via the preshower detector, it will be important in addition to calibrate the photon conversion probability in STAR material upstream of the preshower layers. Since the extent of this material varies widely with η, ϕ and event vertex location, the calibration must be performed as a function of these geometrical parameters. In order to limit the contribution from meson background subtraction to the systematic error in spin correlations extracted for direct photon production at $p_T > 20$ GeV/c, it will be useful to measure these conversion probabilities to a typical precision of ± 0.02. This precision would make the systematic errors from background subtraction smaller than the likely statistical errors from background subtraction. The conversion probability calibrations will be done with the "tagged" photon (from π^0 decay) and π^0 (from $\rho^\pm$ decay) samples mentioned above.

3.7 Rate Capabilities, Time Response and Sorting out TPC Pileup

At the maximum envisioned luminosities, minimum-bias $\vec{p}$-$\vec{p}$ collisions will occur roughly once per RHIC beam crossing. It is then essential that the time response of EMC components be suitable to distinguish one beam crossing from the next (separated by 110 ns).

Even when the trigger rate has been reduced to the desired level, the slow drift time ensures that the TPC will record track segments arising not only from the beam crossing which generated the trigger, but also from uncorrelated events that occur within $\approx \pm 400$ bunch crossings. At

28

full luminosity, this pileup will lead to somewhere between 1000 and 4000 undesired tracks. The resultant TPC occupancy will then be comparable (though less dense near the center) to that for a single central Au + Au collision, which, fortunately, the TPC was designed to resolve. As detailed in Ref. [39], the vast majority of undesired tracks can be eliminated rapidly because they fail by large margins to line up with the EMC and Central Trigger Barrel hits recorded during the trigger beam crossing, or with physically reasonable vertex locations. Finer matching can be done in subsequent analysis by combining TPC with SVT information to achieve vertex resolution better than 1 mm (roughly 1% of the interaction diamond length) and by using the SMD for electrons to provide good spatial resolution ($\approx$ 2.5 mm for the endcap) on the EMC hits. With these resolutions one can even discriminate effectively against tracks from multiple events *within the same crossing*. The analysis in [39] suggested that pileup tracks that cannot easily be distinguished from the desired tracks should yield less than a 1% contamination. We are planning more sophisticated simulations, incorporating all presently envisioned STAR components and presently implemented reconstruction algorithms, to reevaluate the TPC pileup elimination.

The pileup does require that serious pruning be performed on the TPC information before writing an event to tape, in order that the maximum foreseen data acquisition bandwidth not be exceeded. The pruning will be done in the Level 3 trigger [40] already under development for STAR. The imposition in Level 3 of higher-level correlated conditions on the information from various detector components is expected to reduce the event rate for pp running from $\approx$ 60 Hz at the input to 10–20 Hz at the output. Still, an additional reduction by an order of magnitude in event *size* will be needed to reach acceptable data rates (below 20 Mb/s). This will require the elimination of most pileup tracks (*e.g.*, those that clearly do not point toward the interaction diamond) in Level 3 software. In addition, it may require that only the TPC clusters identified at Level 3, and not the raw TPC hit information, be stored for the surviving tracks. The latter option might lead to a slight deterioration in TPC resolution achievable for pp running. The enhanced pp luminosities that will necessitate the event size reduction will become available only in year 3 or 4 of RHIC operation; optimal Level 3 algorithms will be developed in the intervening period.

3.8   Coverage Gaps

The transverse profiles of detected γ and $e^{\pm}$ showers will straddle the boundaries of adjacent towers for a significant fraction of the events. Just as we require 2–3% absolute energy calibration to extract ΔG at the design precision level, we must also avoid any systematic underestimates of electromagnetic energy by $\gtrsim$2%, as might be introduced by shower pulse height loss in gaps between active elements. For this purpose, it is desirable to keep dead areas within the active EEMC acceptance to $\lesssim$2% of the area of a typical shower profile. This goal can be met if the gaps between adjacent scintillating tiles (and also the grooves in which optical readout fibers are seated) have a transverse dimension $\lesssim$1 mm. (Reduced light collection efficiency for particles striking scintillating tiles between the fiber groove and the tile edges can be corrected by a position-dependent pulse-height calibration, with the aid of shower profile information from the SMD.) This requirement disfavors a design based on many independent modules (*e.g.*, each spanning 30° in ϕ), since it would be difficult to maintain such small gaps between modules.

The coverage gaps will be unavoidably larger between the two proposed EEMC halves, and between the EEMC and the STAR barrel EMC. In practice, this means that the fiducial volume used in analyzing γ and $e^{\pm}$ events will have to exclude a few cm near the small η edge of the EEMC acceptance, while small corrections to shower energy will have to be made for showers spanning the much smaller gap between the two EEMC halves. The gap between EEMC and BEMC will

29

be sufficiently large ($\Delta\eta \approx 0.09$, as dictated by STAR integration volumes) that it will necessitate corrections to the total energy of jets spanning this gap. However, as already pointed out in Sec. 3.5, the jet momentum resolution is poor in any case. The jet *direction* determination, which is critical for reconstructing parton kinematics via Eqs. (3–4), should be little affected by the loss of a small fraction of the total jet energy in the gap region. Nonetheless, it is clearly important to minimize this gap in the EEMC design, to the extent possible within STAR integration requirements.

4 Mechanical Design of the EEMC

4.1 Overall Layout and Segmentation

In order to satisfy the requirements outlined in the preceding section, while maintaining reasonable cost and compatibility with STAR's barrel EMC, we have chosen a traditional Pb sampling calorimeter for the EEMC design, with the geometry illustrated in Fig. 18. Twenty-three layers of lead and twenty-four layers of plastic scintillator, arranged in an alternating pattern, give a total depth of 21 radiation lengths $(21X_0)$, sufficient to provide energy resolution $(\sigma_E/E)^2 \approx (16\%/\sqrt{E})^2 + (2\%)^2$ up to >100 GeV. Neglecting non-normal incidence (i.e., essentially for $\eta \to \infty$), the average energy leakage out the back of the endcap would be about 2% for 30 GeV photons and about 9% for 150 GeV electrons. Clearly, the non-normal incidence helps a bit in this regard.
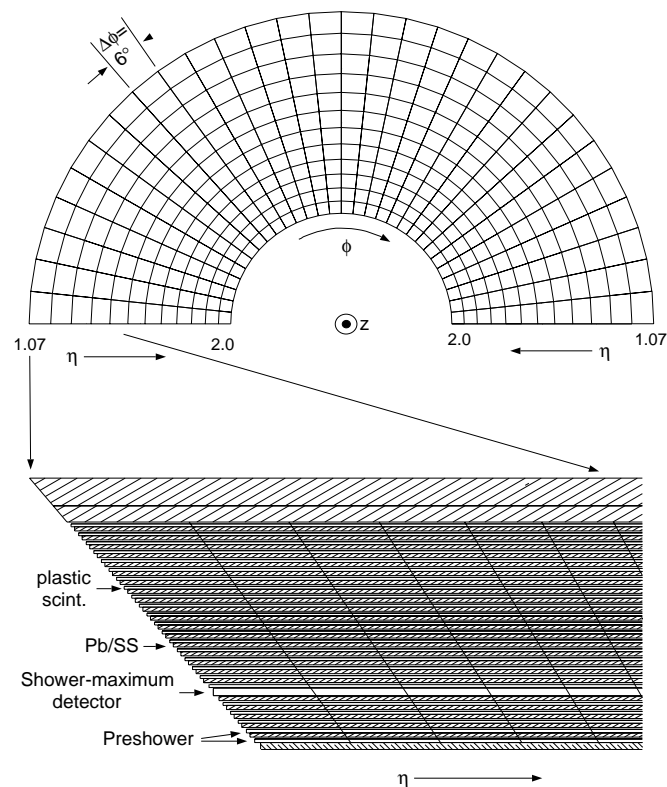

Figure 18: *Proposed tower structure of the EEMC. Frame (a) shows the subdivision (into a total of 720 towers, half of which are shown) in pseudorapidity and azimuthal angle. Frame (b) indicates the depth profile of the projective towers, each with 23 layers of lead/stainless steel absorber and plastic scintillator. The space left for the shower-maximum detector (SMD) is indicated.*

The calorimeter volume is divided into 720 projective towers, ensuring low occupancy for the tens of products expected for typical $p - p$ and $p - A$ collisions. The light output from each of the 24 scintillator layers within each tower is routed via optical fibers to a common photomultiplier tube mounted outside the magnet. The first two scintillator layers are also read out separately, through additional fibers, as a "preshower" detector to help distinguish electrons from hadrons and γ's from π^0's, via differences in their initial shower development. The absorbing layers comprise 4.7-mm thick Pb sheets clad with stainless steel. The scintillator tiles are each 4 mm in thickness, with the exception of the preshower layers, where the thickness is increased to 5 mm to compensate for the sharing of light output between two optical fibers. There is on average ≈ 1 radiation length of material associated with the TPC in front of the calorimeter. A highly segmented state-of-the-art scintillator hodoscope consisting of 2 crossed planes (see Sec. 6 for details) is placed near the depth

of maximum shower development to provide fine position resolution, needed especially to resolve the two close-lying photon showers characterizing π^0 and η^0 decay.

The endcap calorimeter is an annulus of approximate inner radius $\approx$75 cm, outer radius $\approx$215 cm and depth $\approx$36 cm. The inner and outer radii grow with depth, as indicated in Fig. 1, to define constant pseudorapidity. The actual range covered is $1.07 \le \eta \le 2.0$, leaving a small gap between the endcap and barrel calorimeter, needed for services to exit the solenoid. (Simulations indicate that this gap necessitates small corrections to measured jet properties, but does not compromise the physics goals of this proposal.) The full annulus will be divided into two halves for ease of assembly and transport, with each half segmented as shown in Fig. 18. Each of the towers mentioned above spans approximately 0.1 unit in azimuthal angle ϕ and from 0.057 to 0.102 units in η. The gradual change in η segmentation (the small and large angle edge of each tower defines a constant ratio in pseudo-rapidity: $\eta_{high}/\eta_{low} = 1.0536$) is made to maintain smoothly varying transverse dimensions for each scintillator tile, always exceeding a minimum of 8 cm. This minimum transverse size is driven by the minimum bend radius (3 cm) of the readout fibers, and also strongly influences the transverse shower leakage at maximum η. For example, $\sim 95\%$ of the energy deposition for 30 GeV photons at the 5th layer is contained within a cone of radius 2.0 cm. This means that the majority of showers near maximum η will be shared among two or more towers. On the other hand, the gaps between adjacent towers in our design are minimal, and the SMD does not follow the tower geometry, but is arranged in 30° sectors, and should clearly indicate the centroid of shared showers. A cross section showing the layout of the towers *vs.* depth is also shown in Fig. 18.

Details of the EEMC conceptual design, as presently envisioned, are provided in the following sections.
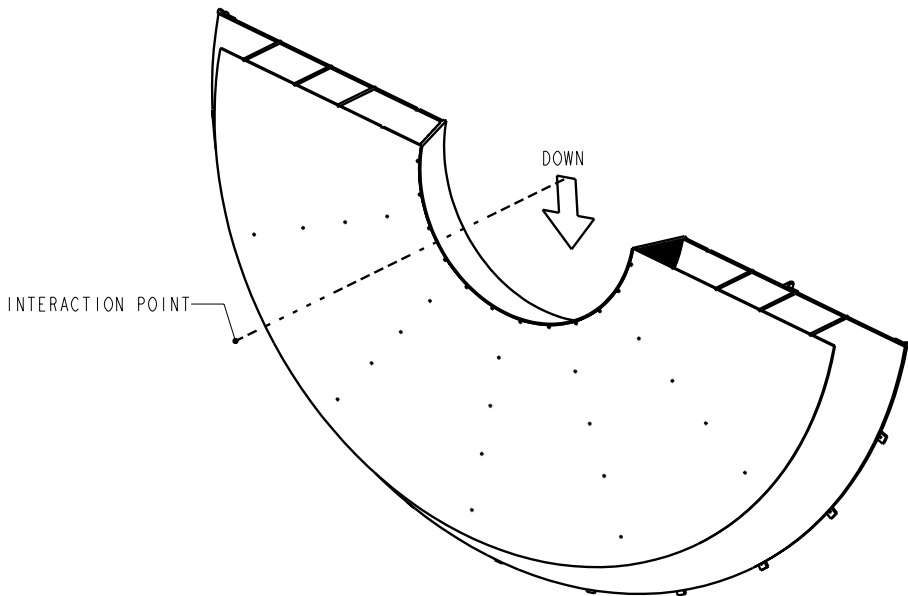
4.2 Mechanical Structure

Figure 19: *A front perspective view of the bottom half of the EEMC.*

The EEMC must include a strong structure that allows the detector to be assembled horizontally and then lifted and rotated to hang vertically on the pole tip of the STAR magnet. On the other

hand, structural members must not generate large dead regions in the detector. One way of addressing this problem is to provide a strong back plate and a central hub on which most of the detector weight hangs. Our intention is to take over such a design strategy, used by both D0 [41] and CDF [29]. A 7/8" thick stainless steel backplate, with some additional bracing at crucial points, will be welded to a 1/2" wall conical tube, whose inner surface is near the boundary of the EEMC integration volume, 1" inside $\eta = 2$. (Note: non-magnetic types of stainless steel are necessary throughout in order not to perturb the magnetic field of the solenoid.) The lead sheet's weight, when mounted on the detector, is carried primarily by the hub which transfers the load to the backplate. The EEMC is split into two halves along a line 15° from horizontal, to allow for easier handling and staging in construction, as shown in Fig. 19. The top and bottom halves take advantage of different features on the STAR poletip to provide primary support of the weight. A mounting ring attached to the backplate of the bottom half will rest on the edge of a recess cut in the inner face of the poletip to house a correction coil as shown in Fig. 20. The top half of the calorimeter will be hung on a 4" diameter pin near the top of the poletip. (There is currently a plug in a hole used for the original lifting fixture of the poletip which can be modified for our purposes [42].) Brackets will attach to the outer radius of the calorimeter back plate to allow bolting to the outer bolt circle already present in the poletip (see Fig. 20). A clearance of 1/2" from the correction coil will be maintained as discussed further in Section 9. The strength of the backplate and hub, as well as expected deflections, are discussed in Sect. 4.3.

In order to attain the necessary depth of the EEMC in radiation lengths, within the space constraints imposed by STAR and at reasonable cost, while maintaining the desirable difference in response (see Fig. 14) to electromagnetic particles *vs.* hadrons, we have chosen Pb as the primary radiator material. However, Pb is a difficult material to work with. It is not particularly strong and tends to creep over time if stressed. To solve these issues we intend to follow a technique used at CDF [29], laminating the Pb with stainless steel. That is, a half annulus of 4.7-mm thick Pb is clad by epoxying 0.5 mm stainless steel to the surface, on each face. In addition, 1" diameter stainless steel inserts will be placed in the lead and spot welded to the stainless steel sheet at points around the outer circumference and on radial lines every 30°, in order to provide solid points to transfer the load to the other structural members. Tie rods will pass through a 3/8" aluminum front plate of the EEMC, and the 23 layers of lead/steel sheets and intervening stainless spacers, to support the lead radiators and maintain the separation between them needed for insertion (without compression) of the scintillator tiles.

At the inner circumference, the Pb/SS sheets will fit on machined steps in the support hub (see Fig. 21). A stainless steel ring will be spot-welded in place at the inner radius of each Pb/SS radiator sheet and then to the inner hub surface. The rings and hub will be keyed to provide primary support of the Pb sheets when the EEMC detector is vertical on the poletip. The steps on the hub will also align the Pb sheets in depth. The front 5 layers of Pb/SS radiators, i.e., those in front of the shower maximum detector, will be fastened to the hub with bolts rather than welded, to allow future access to the SMD which must be built into the mechanical structure. In its entirety, the stainless steel inserts and ring provide a structure in which all the large loads are carried primarily by stainless steel and the Pb just serves as the filler in the laminated plates. Deflections of the Pb should be small enough to allow insertion of the megatiles after assembly of the mechanical structure. Details of finite element analyses performed are provided in section 4.3.

The full EEMC will have an outer diameter of about 5 meters and weigh $\approx$28 tons. We intend to segment the detector into two halves along a line deviating from the horizontal by 15°, in order to match the EEMC 30° sectors to those of the TPC. In particular, the TPC end planes contain fast multi-wire chambers (MWC) that provide particle multiplicities for use in the hardware (level 0)
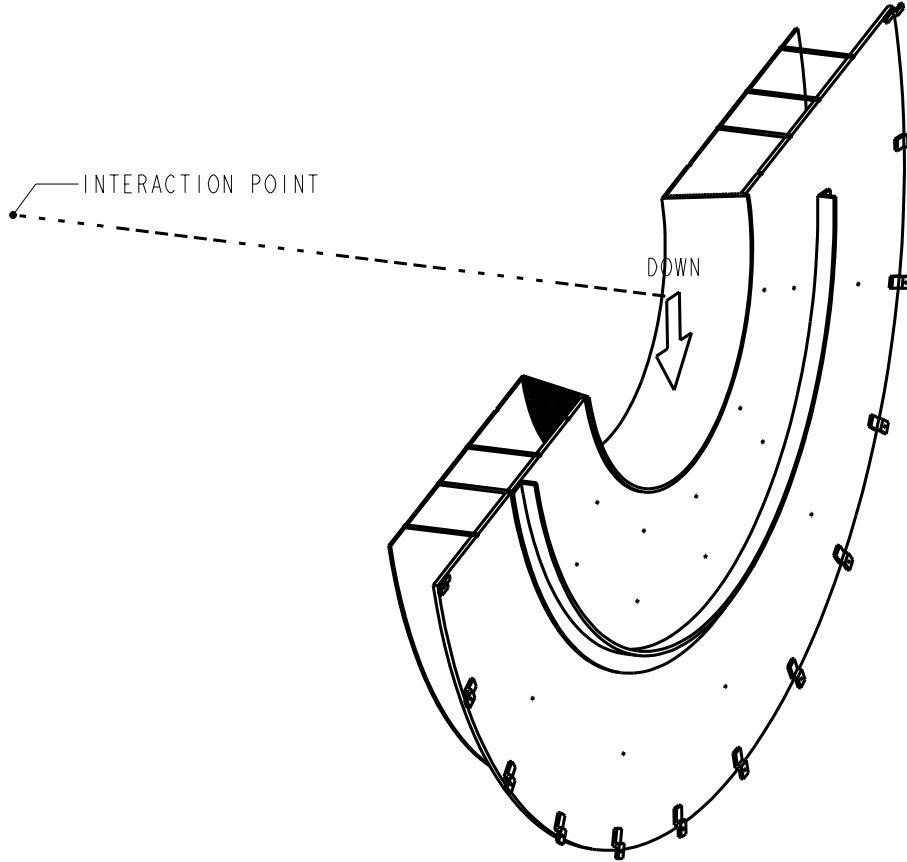
Figure 20: *Backplate of the EEMC, showing the bolt circle by which it will get attached to the poletip and the mounting ring that will sit on the inner circumference of the poletip.*

trigger. For jet triggers we will want to correlate EEMC and MWC multiplicities within common 60° azimuthal sectors in the hardware trigger. The division into two halves complicates the structural design issues slightly but will make assembly, handling and testing considerably more convenient. It will also allow for a staged approach in construction.

4.3   Structural and FEA Calculations

We have begun to study the mechanical structure of the proposed EEMC design using standard engineering estimates and finite element analysis (FEA) [43]. At this point we have done initial FEA calculations on the Pb/SS plates and the backplate/hub/frontplate/tie rod systems. We are currently in the process of using these calculations to refine the designs and minimize deflections. So far, only estimates have been made regarding the mounting to the poletip, but these will be followed up shortly with FEA calculations.

Figure 22 shows a calculation of deflections of the rear or largest Pb/SS radiator plate loaded by gravity when the detector is laid down horizontally for assembly. A clearance of 1 mm, over and above the thickness of a megatile and its associated optical fiber guide, is left in the space between radiator plates so that the megatiles can be inserted easily after the mechanical structure is assembled. The issue is to verify that this clearance is enough. (Note that in general the plates
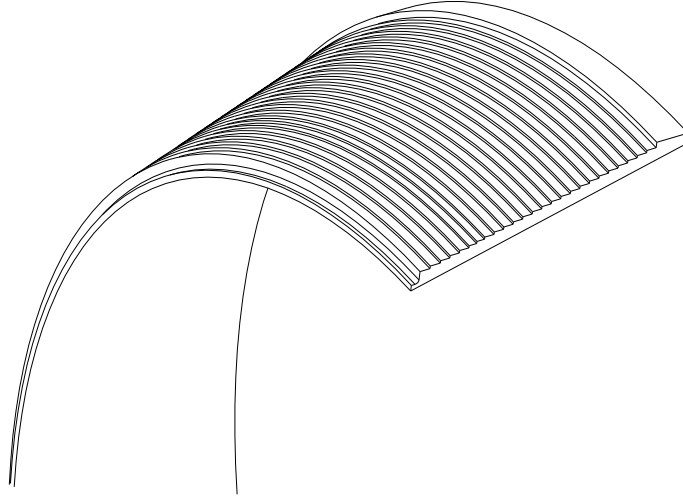
Figure 21: *The inner hub, showing machined steps on which the Pb/SS radiator sheets will be fit and welded.*

will deform in the same direction by roughly the same amount so that the gap should be maintained for all but the last layer.) Early on, the calculations revealed that it would be necessary to provide angled tie rods at the outer circumference midway between the tie rods on radii separated by 30°. The calculation in Fig. 22 assumes the use of two tie rods on each 30° radial line, plus one angled tie rod passing along the outer edge midway between each pair of 30° radial lines. The Pb/SS plate is constrained to have no deflection at each active tie rod location and at the inner circumference. The maximum calculated deflections are already less than the 1 mm clearance in the design. Further work will be done to optimize the number and positions of tie rods along each radial line. Evaluation of the stresses in the stainless steel sheets show they are largest near the tie rods, approaching 1/3 of the yield strength. FEA calculations have also been done for the vertical orientation of the EEMC, but deflections and stresses are then considerably smaller than in the horizontal (assembly) orientation and appear not to be an issue.

The second set of FEA calculations performed to date are related to the strength of the backplate and hub assembly. These are intended to carry the weight of the detector and support it off the magnet poletip. A baseline calculation of the bottom half of the detector is shown in Fig. 23. Here a 1/2" wall conical hub is attached to a 7/8" backplate. Both are of stainless steel. A 3/8" aluminum front plate is attached to the hub. Tie rods of 1 cm diameter are located at the intended positions. (Note that in the actual detector these will be somewhat constrained from bending by the Pb/SS radiator plates, which are not included in this calculation.) The back plate is constrained from moving at 12 points around the outer circumference, corresponding to bolts that will be placed into the outer bolt circle on the poletip. It is also constrained at points where an unconstrained calculation indicated that the back plate would push against the poletip surface. The maximum deflection of 5 mm occurs at the top inner corner, near where the hub attaches to the back plate. The primary tendency is for the hub to fall forward due to the weight of the detector, deflecting the back plate out away from the poletip, as can be seen in the edge view of Fig. 24. Some cross-bracing between the front and back plate at the outer diameter was added to help prevent the front plate from translating downward as the cone bends. Though these deflections are not large, we are
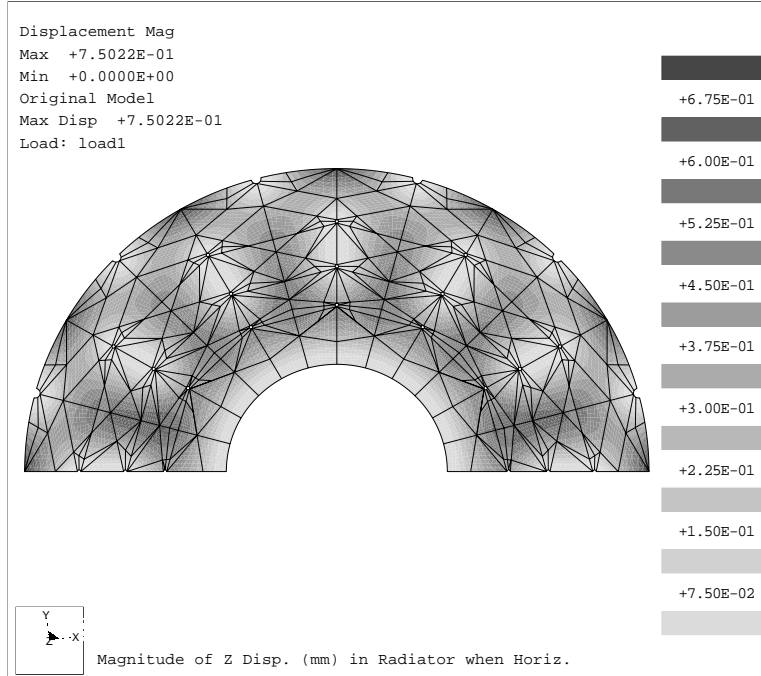
```
Displacement Mag
Max  +7.5022E-01
Min  +0.0000E+00
Original Model
Max Disp  +7.5022E-01
Load: load1
```

+6.75E-01
+6.00E-01
+5.25E-01
+4.50E-01
+3.75E-01
+3.00E-01
+2.25E-01
+1.50E-01
+7.50E-02

Magnitude of Z Disp. (mm) in Radiator when Horiz.

Figure 22: *Results of an FEA calculation on the rear (largest) Pb/SS radiator plate with the gravitational load perpendicular to the plane of the plates. This corresponds to the detector lying in a horizontal position for assembly. The deflections are specified in mm.*

working to reduce them. We are currently investigating stiffening the back plate locally, bolting it to the poletip along the upper edge, and further cross-bracing at the outer circumference. We expect an optimization of these approaches to reduce the deflections by a factor of 2.

We have not yet performed FEA on the mounting scheme. Hand calculations reveal that 4.5 sq. in. of steel material are needed to support the load of one half the detector, assuming 20kpsi shear yield strength and a safety factor of 3. There are 36 1/2-13 tapped holes for bolts on each half of the poletip face. It would require 32 of these bolts to provide the needed shear cross section, indicating that it will be quite difficult to use these holes to support the full load. This has led to separate mounting schemes for the two halves, where the load is transfered to features on the poletip and the bolt holes are used only to hold the calorimeter modules against the surface. For the bottom half of the EEMC a section of a ring will be welded perpendicular to the back plate at a radius where it will capture the edge of a recess machined into the poletip for the correction coil. This provides appreciable surface area and there is sufficient clearance to the coil, as shown in Fig. 25. This ring provides the primary support of the lower load. For the top half we will use a 4" diameter hole near the top of the poletip, which was originally used for lifting the poletip into place on its holding fixture. This hole is currently filled with a plug which can be removed and reworked to add a stainless steel pin extending out of the surface of the poletip on which the backplate can be hung for primary load support. Again, the bolts around the outer circumference serve to hold the upper half calorimeter against the poletip.

The FEA calculations have revealed no major problems that would compromise these design concepts. Work is ongoing to optimize details.
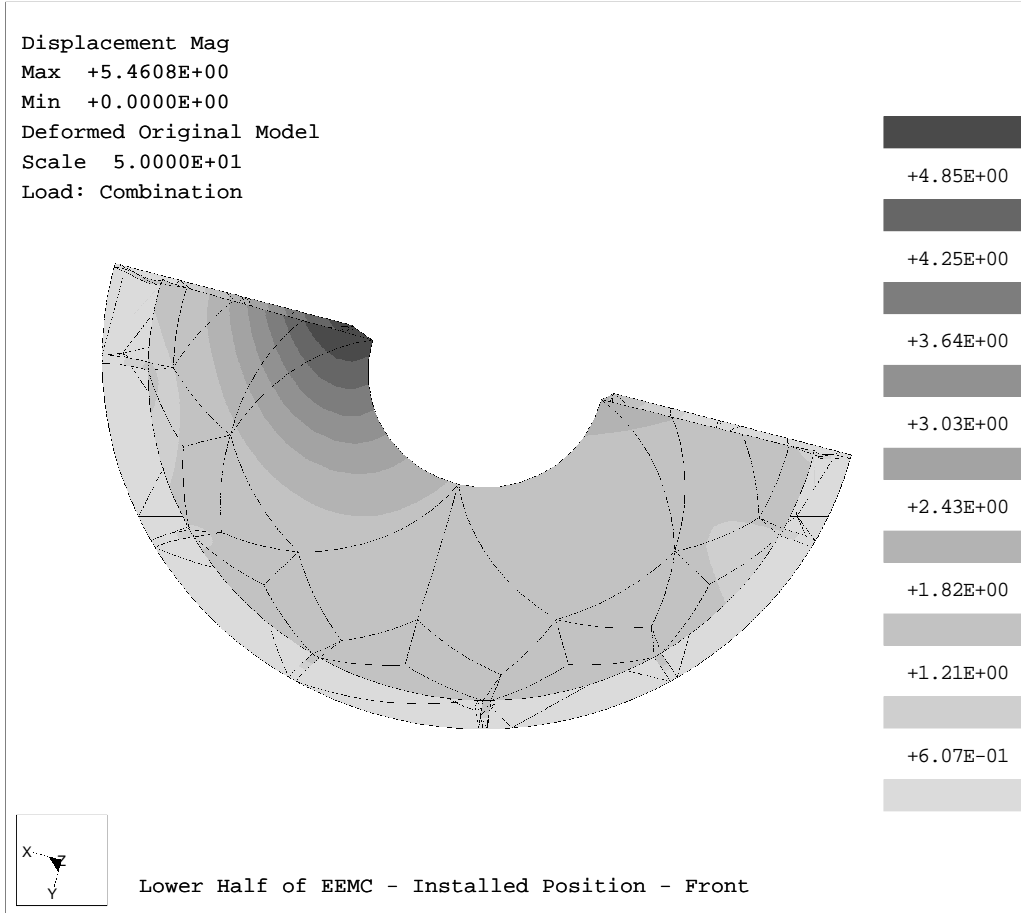
```
Displacement Mag
Max   +5.4608E+00
Min   +0.0000E+00
Deformed Original Model
Scale  5.0000E+01
Load: Combination
```

+4.85E+00

+4.25E+00

+3.64E+00

+3.03E+00

+2.43E+00

+1.82E+00

+1.21E+00

+6.07E-01

Lower Half of EEMC - Installed Position - Front

Figure 23: *Results of an FEA calculation on the backplate, hub, front plate and tie rods for one half of the detector. The calculation is for the lower half detector hung as if on the poletip with a 15° rotation of the upper edge away from horizontal. The hub is loaded with both a vertical gravitational load as well as the moment due to the center of mass displacement. The deflections are specified in mm.*

4.4   Depth Budget

A cross section of the layers of the EEMC is shown in detail in Fig. 26. There are 23 layers of Pb/SS laminate that serve as the primary radiators and an aluminum front and stainless steel back plate for mechanical integrity. The sampling at each layer is done with a scintillator whose light is collected and transported by a wave length shifting (WLS) fiber. A standard layer in this design comprises Pb/stainless steel (SS) laminate (4.68 mm Pb, clad by two 0.5 mm stainless steel sheets, for a total of ~0.85 radiation lengths) followed by a 4mm thick scintillator tile, a 1.6 mm plastic sheet for fiber routing and 1 mm of clearance. The whole assembly represents 21 radiation lengths at normal incidence.

Three of the EEMC layers are configured in a special way:

1) The first two layers of scintillator immediately after the front support plate are each read out by two independent fibers. One fiber in each case is routed to the phototube that measures the total light produced by the tower. The second fiber from each of these layers is read out separately,
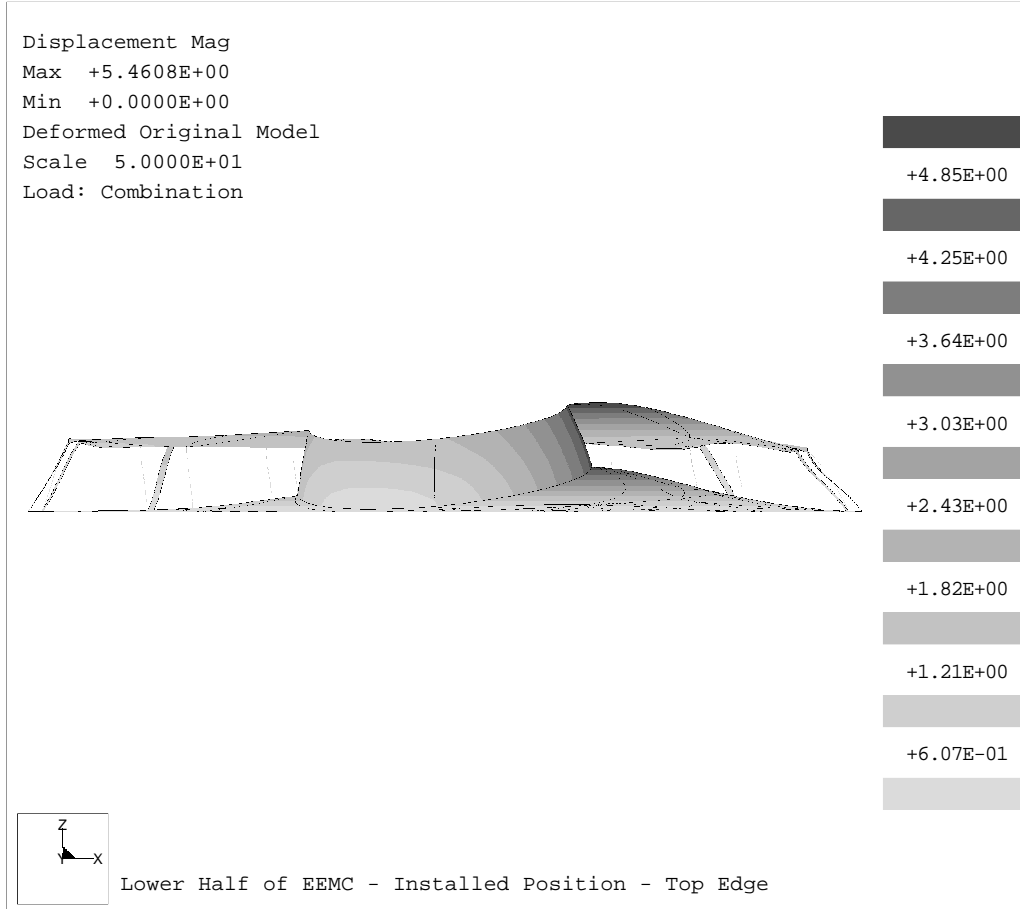
```
Displacement Mag
Max   +5.4608E+00
Min   +0.0000E+00
Deformed Original Model
Scale  5.0000E+01
Load: Combination
```

```
                                          +4.85E+00

                                          +4.25E+00

                                          +3.64E+00

                                          +3.03E+00

                                          +2.43E+00

                                          +1.82E+00

                                          +1.21E+00

                                          +6.07E-01
```

```
Lower Half of EEMC - Installed Position - Top Edge
```

Figure 24: *Results of the same FEA calculation as in previous figure. The view is edge-on, looking at the inner surface of the hub from above. Deflections have been magnified by 50 in the drawing, so the shape and direction can be seen. The deflections are specified in mm.*

to form a preshower detector, to aid in γ/π^0 and e/hadron discrimination. The scintillators in the first two layers are increased slightly in thickness (5mm) to account for the lower light output in each fiber when two are used on the same tile. The same 1.6 mm plastic layer and 1 mm clearance are provided in these layers.

2) The third special layer will be placed about 5 layers deep in the detector. This layer includes a shower maximum detector (SMD) in addition to a standard 4 mm scintillator layer. The SMD will comprise two planes of orthogonally oriented scintillating strips, with WLS fibers running down axial holes in each one (see Sec. 6 for details). In addition, there are layers between the scintillator planes used for fiber routing. The entire SMD assembly, including scintillator layers, substrates, and fiber runs, will use 21 mm of depth.

The front plate is 3/8" aluminum and the back plate 7/8" stainless steel. Finally, 1.3 cm is left between the poletip and back plate for mounting hardware and additional stiffening members for the back plate.

The entire depth of the proposed design is thus 35.6 cm, to be compared to the integration space allowed by STAR, whose depth is 37.465 cm. Thus, there is almost 2 cm of unused space in
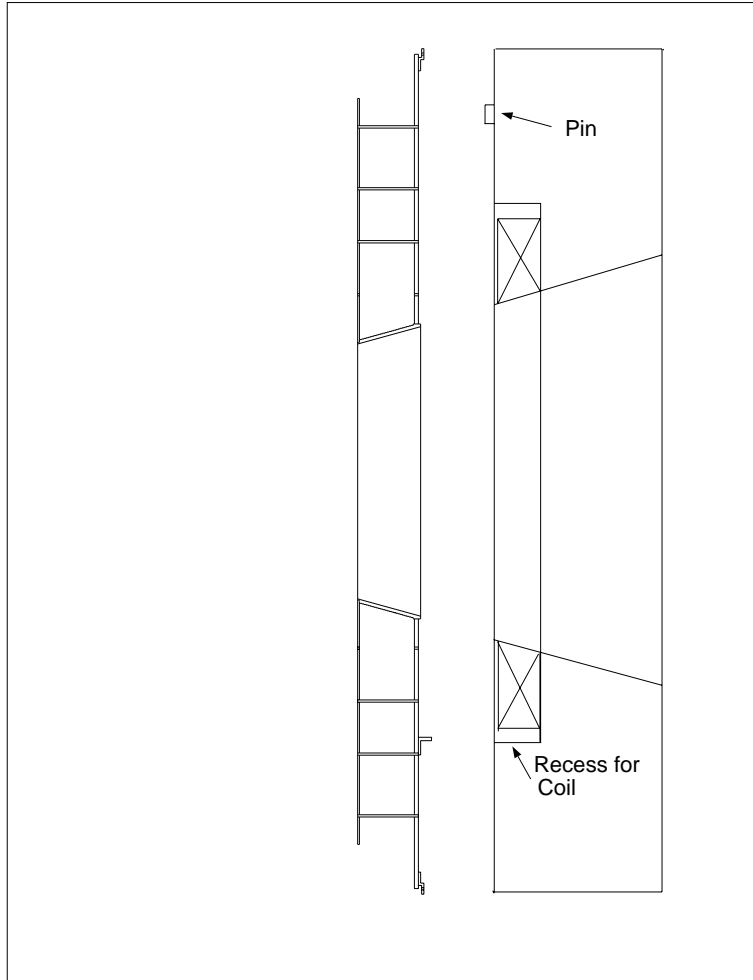
Figure 25: *Details of capturing the outer circumference edge of the poletip cutout for support of the main load of the lower calorimeter half. The pin for support of the upper half is also shown*

the present design. This leaves sufficient flexibility for additional structural features, or increases in thickness of selected layers, that may be needed as the design matures.

4.5   Staging, Assembly and Installation Plans

The splitting of the detector into two halves allows the assembly to be staged, as may be dictated by work loads, budgets or installation windows. The assembly procedure for one half is envisioned as follows:

1) The back plate and hub are welded together and any final machining of the assembly completed.

2) The tie rods are inserted in the back plate and then Pb/SS radiator plates are placed one by one on the hub and over the tie rods with appropriate spacers. The plates are welded to the hub.

3) This process continues until after the 6th radiator layer from the front is installed. At this point the SMD layers are installed, via a procedure described in Sec. 6.2. Since these layers have fibers crossing the 30° tie rod boundaries they cannot be inserted later.
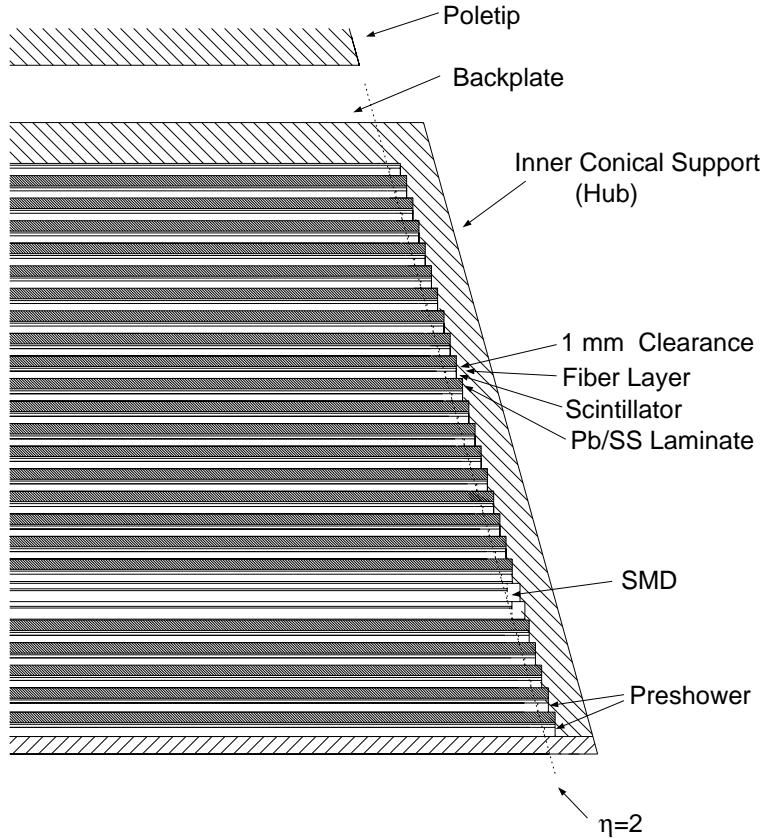
Figure 26: *A cut through the EEMC near $\eta=2$. The mechanical structure as well as the absorber scintillator layers are shown.*

4) The front 5 radiator plates are installed in a manner similar to the others, except that bolts are used to fasten them to the hub. This is necessary to allow future access to the SMD.

5) The front plate is bolted on to the hub and to the tie rods, completing the mechanical structure. Angled tie rods at the outer circumference are added. These are needed to minimize deflection of the radiator sheets at the outer circumference for megatile insertion.

6) The megatiles are inserted into the mechanical structure. A 30° sector consists of two 12° megatiles which are inserted first and then pushed out to engage the tie rods, and a single 6° megatile inserted last into the center between the other two. Temporary brackets are used to support the Pb sheets at the outer edge during megatile insertion. Note that all fibers were routed to a connector at the outer edge of the megatile during megatile assembly.

7) Fibers to SMD strips terminating on the outer circumference are inserted into the SMD and the connector fastened to brackets nearby.

8) The assembled detector can then be tested with cosmic rays or radioactive sources.

The fully assembled detector halves will be transported to Brookhaven National Lab via air ride truck after attaching suitable transportation fixtures. Sufficiently large fork trucks are available at BNL to transport a detector half to a location where crane access is available. The back plate will be stiffened with I-beams for the lift from horizontal to vertical. Lifting fixtures will be attached to the back plate and central hub for lifting by overhead cranes. (The lifting fixtures will be inspected and tested to BNL standards prior to the lift.) The west STAR magnet pole tip will be held from its lifting carriage at a convenient place in either the Wide Angle Hall or West Assembly Hall. The overhead crane will lift the EEMC half from the floor to hang vertically. The poletip carriage

can tip the poletip forward or backward from vertical by $\pm 5°$ to match small misalignments from vertical in the EEMC lifting. The crane will move the detector so that the ring captures the coil cutout in the poletip for the lower half, or so that the upper half sits on the protruding 4" pin. Very fine motion adjustments can be made with the poletip lifting carriage. Alignment pins will be used in poletip bolt holes to enforce alignment during the procedure. Fastening the 12 bolts will then secure the detector to the face of the poletip. Note that the lower EEMC half will need to be installed first.

5 Tower Optical Systems

5.1 Scintillator Megatiles

As summarized earlier, the calorimeter is segmented into 720 projective towers by dividing each scintillator layer into tiles which align properly with the corresponding tiles in front and behind to form the towers. Light from the 24 tiles (one from each scintillator layer in depth) within each tower is summed in a single phototube. In each layer, a single $6°$ ϕ slice contains 12 tiles of different size to provide the η segmentation, spanning the entire range $1.07 \leq \eta \leq 2.0$. (The gap from the barrel EMC coverage, which ends at $\eta \approx 0.98$, corresponds to a region needed to bring utilities and support structures to the central STAR detectors, see Fig. 1). As shown in Fig. 18, the tile segmentation produces projective towers spanning 0.1 in azimuthal angle (ϕ) and a continuously varying pseudorapidity range ($\Delta\eta$ from 0.057 to 0.102, with η increasing by a constant factor of 1.0536 across each tile). In addition, in order that the towers be projective to the interaction point (i.e. define fixed η with depth), the tiles within each tower grow in size with increasing depth.

The segmentation will be produced using megatile construction as developed and used for CDF [44] and adapted for the barrel EMC in STAR [38]. In this technique, a large piece of scintillator, a $6°$ or $12°$ wedge in ϕ (one or two tiles wide) for our EEMC, is machined with a router most of the way through its depth (0.01" material remaining) in order to separate one tile from the next. The isolation grooves (0.035" wide) are filled with TiO_2 loaded epoxy [45] to give good optical isolation from the adjoining tiles, as well as to restore the mechanical strength. A black magic marker is used to draw a line on the back side, where a thin bridge of the scintillator is left joining adjacent tiles, to complete the optical isolation. The edge of the megatile is painted with TiO_2 reflective paint and the large surfaces top and bottom are covered with white Tedlar plastic to complete a diffuse reflective surface for each tile.
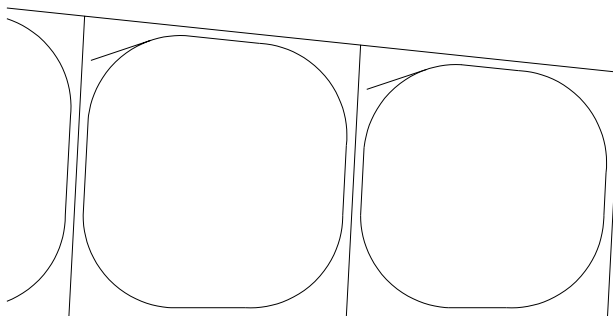

Figure 27: *Schematic of sigma groove positions on a megatile.*

A standard layer of the endcap calorimeter will use 4 mm thick Kuraray SCSN81 polystyrene scintillator. (The front two layers are used as the preshower. They have 2 WLS fibers and their thickness is increased to 5 mm to correct for the reduced light output in an individual fiber when sharing the scintillation light with another.) The Kuraray scintillator is chosen because of its reasonable cost, high quality and consistent dimensional tolerances. Sigma-shaped grooves are machined into each tile to capture 0.83 mm diameter wave length shifting (WLS) fiber. The groove is 0.030" wide by 0.079" deep. A circular shaped key 0.042" in diameter is widened in the bottom of the groove with a ball mill to capture the fiber. The grooves are 2 mm from the edge of the tile except in the corners where a 3 cm radius is maintained. An example of the groove path in a tile is shown in Fig. 27.
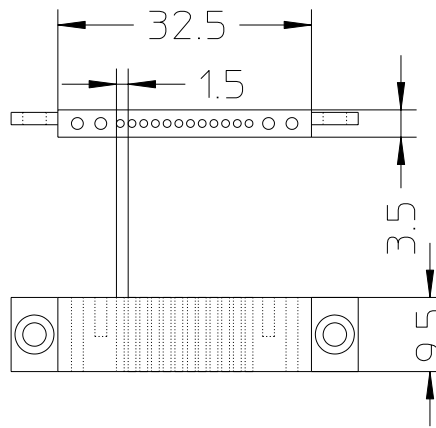

Figure 28: *Schematic of a 12-fiber connector. Dimensions are in mm.*

A 1.6 mm thick layer of plastic with machined grooves will be placed on top of each EEMC megatile to serve as a fiber-routing layer. All WLS fibers will be routed to the outer edge of the megatile, where the 12 fibers are attached to a multifiber optical connector similar to those developed for CDF [46]. For the preshower (the first two megatiles), each tile has two fiber grooves, and so 24 WLS fibers run to two connectors at the outer edge of each of these megatiles. It appears that we will have to design and have a 12-fiber connector injection-molded commercially. We have contacted two other groups currently in the process of doing this and will build on their experience. The dimensions of the connector we are envisioning are shown in Fig. 28. Tape will be used to cover the fiber-routing grooves, capturing the fibers. An ~1 mm O.D. thin walled tube will be placed in a groove in the fiber routing layer to allow a radioactive source to be inserted into the megatile for testing purposes.

Preliminary tests of light output with our prototype megatiles, using the SCSN81 scintillator and planned WLS fiber, indicate that we should be able to maintain our light output requirement of 2 p.e./MIP when actual fiber run lengths and optical connector attenuation are factored in. In a small fraction of the total tile count, where the fiber runs are longest, achieving the required light signal may require fusing of clear fiber to the WLS fiber before reaching the connector at the

outer edge of the megatile. We are currently in the process of making a 12 tower prototype as discussed in detail in Sec. 6.4. The prototype employs 12-tile megatiles similar in geometry to a 3 × 4 tower section of the EEMC near $\eta=2$. These megatiles are being cut on a CNC mill. Thus, we already have some machining (although EEMC megatile machining will be performed on a high speed router not yet available) and gluing experience with megatile production.

Connector

1/16" Fiber
Routing Layer
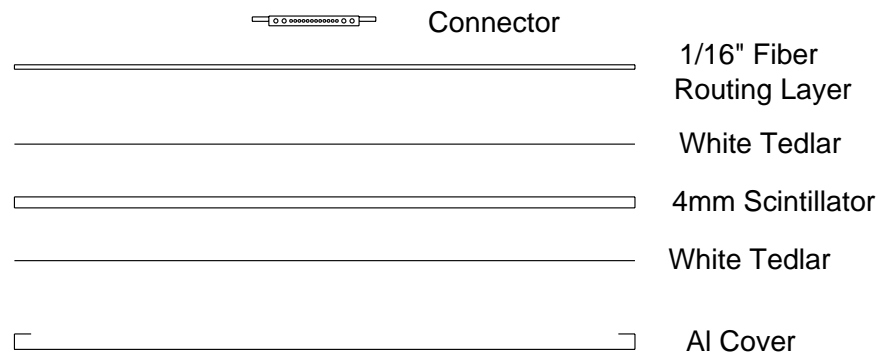
White Tedlar

4mm Scintillator

White Tedlar

Al Cover

Figure 29: *The components of a megatile assembly. These consist of the scintillator megatile, white Tedlar cover sheets, a 1/16" plastic fiber routing layer, an aluminum cover layer and a black Tedlar outer cover (not shown) to make the assembly light tight*

Finally, we will have a thin ($\approx0.008"$) aluminum sheet metal cover plate manufactured to protect the side of the megatile opposite the plastic fiber routing sheet. It will have edges that curl around the sides of the megatile and up on top of the plastic routing sheet to hold the assembly together. The components of a complete megatile assembly are shown in Fig. 29. The megatile will be extended about 1/4" beyond the active area at both $\eta=1.07$ and 2.0 to provide a region where screws can be used to fasten the fiber routing sheet, scintillator sheet, connector and sheet metal cover together. This assembly will then be enclosed in black Tedlar plastic cover sheet to make it light-tight. These assemblies will then slide between the Pb/SS layers after the mechanical construction. There will be two 12° and one 6° megatile assembly in each 30° sector of a detector

44

layer. The 12° assemblies will go in first and small cutouts in their edges will align them against the tie rods. A 6° assembly will then be inserted between the two 12° assemblies, thus holding them against the tie rods. Each assembly will have tabs as part of the sheet metal cover which can be fastened with a screw to the adjacent radiator layer. In the center of the tile, the same epoxy used for the isolation grooves will be used to attach the Tedlar and plastic fiber routing layer to the scintillator.

5.2 Optical Fibers

Light will be transported from the scintillator tiles to phototubes (PMT's) mounted on the outer face of the STAR poletip by a combination of WLS and clear fibers, as shown in Fig. 30. The WLS fiber will be Kuraray multiclad Y11 (200ppm) S-type fiber, 0.83 mm in diameter. It will be polished at both ends and mirrored with sputtered aluminum on the end in the tile. The longest WLS fiber run to the edge of a megatile is about 1.6 m for the large-η tiles. We expect the light intensity reaching the end of such a fiber to be equivalent to about 3.5-4.0 p.e./MIP. The light output of the tiles will scale with the ratio of the fiber length to area of the tile, ℓ/A. The variation is about 10% from the front to rear of the detector. This will be corrected, at least in part, by varying the length of the WLS fiber path in the fiber-routing layer with depth of the layer in the EEMC. For example, the paths in the prototype detector under construction are varied by 21 cm from front to back, to compensate for ℓ/A scaling. To the extent that thermal fusing of clear to WLS fiber is used to limit light attenuation from the tiles at highest η, the length of the WLS vs. clear fiber can be further adjusted with depth to compensate for ℓ/A scaling in these cases.
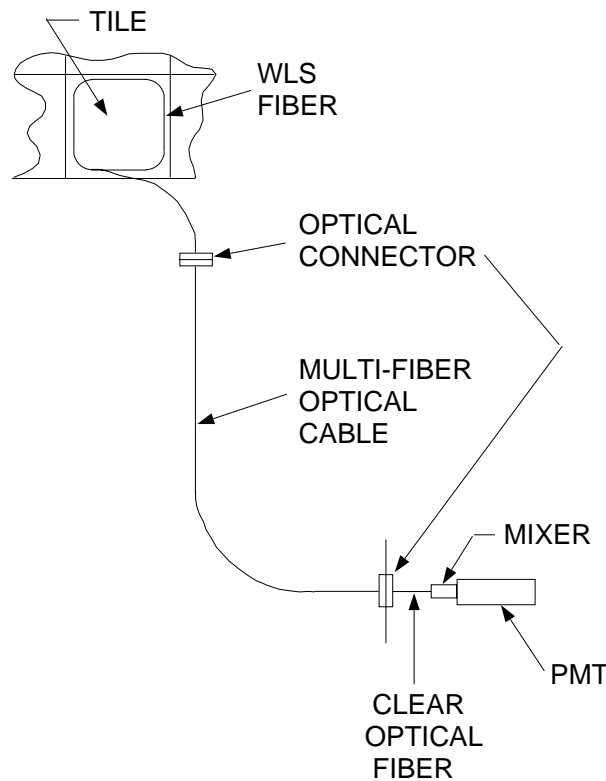
Figure 30: *Schematic illustration of the optical readout system for the EEMC. The scintillator tile is read out by a WLS fiber, which is coupled via a clear fiber ribbon cable to a patch panel attached to the PMT boxes. At the patch panel the clear fibers will be rebundled to group towers rather than megatiles together. For a small fraction of the tiles, it may be necessary to fuse the WLS fiber to clear fiber before reaching the first connector.*

The light will be transported from the megatile-edge connectors to the PMT boxes via clear

45

0.93 mm diameter Kuraray double clad fibers, joined into ribbon cable bundles with a plastic coating, and terminated with commercially injection-molded connectors at both ends. These fibers will be routed after the detector is mounted on the poletip. Fiber ribbons leaving the edge connector of a megatile will turn to travel back toward the poletip along the outer edge of the EEMC, to the point where they will exit through the services gap at $\eta \approx 1$. They then run on to the outside surface of the poletip where they enter PMT boxes described below. Details on the amount of space at the $\eta \approx 1$ gap needed for the fibers are provided in Sec. 9.2. The longest run of fiber from megatile edge to the PMT boxes is for the megatile at 6 o'clock. This is estimated to be 2.5 m, with up to an additional 1 m inside the PMT box. These fiber runs are very similar in length to those quoted for the CDF endplug upgrade, where sensitivity exceeding the design goal of 3 p.e./MIP has been achieved [44]. Estimates from our early prototypes indicate that we can expect > 2 p.e./MIP light signal output. At 2 p.e./MIP the simulated energy resolution of a tower is still dominated by shower to shower fluctuations and not by photostatistics.

Megatile Layer 1

Megatile Layer 24

Tower 1

Tower 12

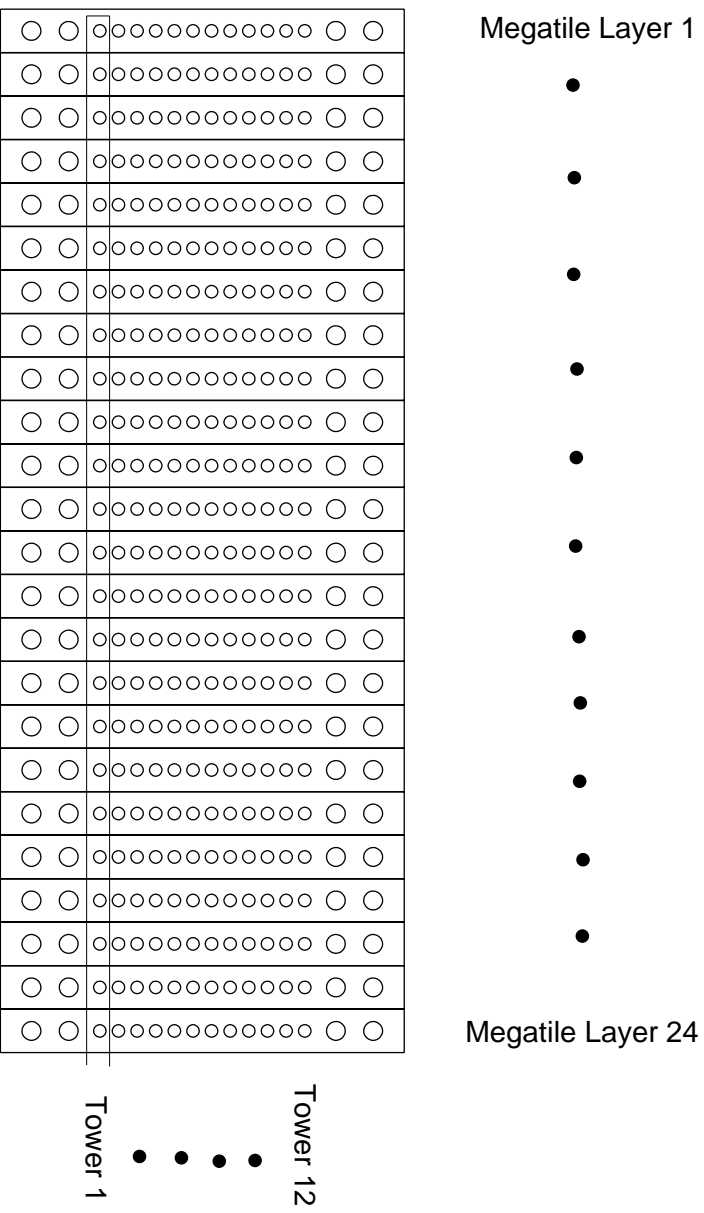Figure 31: *Schematic diagram of the optical fiber layout at the PMT box patch panel. Fiber ribbons enter in columns corresponding to single megatiles, but exit along rows to single tower PMT's. Alternatively, the fiber ribbon from a given megatile can be connected to a separate patch at the PMT box, from which fibers run within the box to special calibrated high-gain PMT's used for diagnostic studies of individual tiles.*

Tower fibers are naturally routed from the detector grouped by megatile. They need to go to the PMT's grouped by tower. The transformation between groupings will occur at the patch panel into the PMT boxes. This regrouping is quite natural when the 24 fiber ribbons containing the fibers from all tower tiles (neglecting the preshower, which will be handled separately) within a given 6-degree sector are collected, one above the other, into two groups of 12 ribbons. Each group can then be viewed as a 12 x 12 matrix of fibers, each column (incoming ribbon) corresponding to one megatile and each row to one tower as illustrated in Fig. 31. The 24 fibers, plus one or two diagnostic fibers from a separate patch mated to light pulser input, will then be routed inside the PMT box to the appropriate tower tube. Each tower PMT will have a light guide or mixer to equalize the photocathode illumination from the various input fibers. Each PMT box will contain an additional connector, from which all 12 fibers are routed internally to a special, calibrated high gain PMT used for diagnostic purposes. Any individual tile within a single megatile can then be tested by correlating the diagnostic PMT output with that from the 12 corresponding tower tubes, each of which will still collect light from the remaining 23 layers in the tower.

5.3 PMT's, Bases and High Voltage Distribution

Light-tight cooled boxes for the PMT's will be permanently mounted on the outside surface of the poletip, in a configuration described in more detail in Sec. 9.1. The 24 fibers from each tower are routed to a single-anode PMT, which gives a signal proportional to the total energy deposited by the shower within that tower. The tubes are required to have high gain ($\gtrsim 2 \times 10^5$), good linearity ($\pm 2\%$) over a large dynamic range, and low noise (dark current <5 nA). We believe Burle 83101 tubes meet our needs and have ordered these for the prototype currently under construction. We are also considering other potentially lower cost tubes, such as the EMI 9125 and a number of choices from Hamamatsu. The high voltage for these tubes will be generated in Cockroft-Walton type bases using the same system as planned for the BEMC.

Measurements have been made of the magnetic field on the back of the poletip near where the PMT's will be placed. These are discussed in more detail in Sec. 9.2. It is clear that the tubes will have to be shielded from the field in a steel box and wrapped in mu-metal shields. Calculations show that the tubes can be effectively shielded.

5.4 Preshower Detector

The decision to read out the first two tiles within each tower independently as a preshower detector is based on the differences in initial shower development between single photons and π^0's, and between electrons and hadrons. Two WLS fibers will be inserted into the σ-groove for each of these tiles, and they will transport light to two separate phototubes: the usual PMT for the tower to which the tiles belong, plus a dedicated channel of a multi-anode PMT (MAPMT) for independent readout of each preshower tile. The preshower megatiles will be made thicker than the other tower megatiles, as needed to compensate for the light loss caused by the parallel readouts, thus enabling us to maintain proper gain matching of these layers to the rest of the tower. Since the energy deposited in the first two layers is only a small fraction of the total tower energy deposition, the precision of gain matching of the preshower layers is less critical to the overall resolution and linearity requirements than is gain matching of tiles nearer the maximum shower development.

The dynamic range, resolution and linearity demands on the preshower layers are much less stringent than on the towers as a whole. Therefore, the light from the preshower layers can be routed to 16-anode PMT's, whose performance criteria (and cost per channel) are relaxed in comparison with the tower PMT's. The same model tubes, Hamamatsu H6568, will be used for this purpose as

for the SMD (see Sec. 6.3 for details). A total of 96 such MAPMT's will be needed for the preshower layers, leaving one input on each MAPMT free for a light pulser to monitor gain stability. Fiber routing from the relevant tiles to the MAPMT's will be very similar to that described above for the towers, but without the need for the megatile-to-tower rerouting at the PMT box.

For $e^{\pm}/h^{\pm}$ discrimination, we will compare the summed energy deposition in the two preshower layers to the total energy recorded from the corresponding tower. Use of the preshower to distinguish γ's from π^0's at high energies (to supplement the SMD information) is more delicate. The present plan is to use the energy signal from the first layer alone for this purpose, since the probability that at least one of the two photons from π^0 or η^0 meson decay converts upstream of this layer will be significantly larger than that for a single photon of the same energy as the meson. On average, particles heading toward the EEMC will traverse about 0.7 radiation lengths of material upstream of the first EEMC scintillator tile. Our simulations show that 30–70 GeV photons then have roughly 50% probability to deposit appreciable energy in this first layer, while the corresponding probability for π^0's over the same energy range is 75% (as expected from the combinatorics of the two photons). This difference in conversion probabilities, if used to supplement the SMD discrimination that remains at such high energies (see Sec. 6.1), would provide adequate means for meson background subtraction from the direct photon yield. However, the amount of material upstream in STAR has rather wide variations with η, ϕ and event origin, and it is not yet clear if these can be calibrated sufficiently well to allow reliable determination of the conversion probabilities event-by-event.

Because of the above concern, we are also considering an alternative layout of the preshower. In this approach, we would make the first *five* scintillating layers into preshower layers, each of 5 mm thickness with two fibers reading them out in parallel. The summed energy of the first five layers could then be compared to the full tower sum for somewhat improved γ/π^0 distinction. The pulse height sum for layers 2-5 would be performed still in a single MAPMT channel, in order that this approach not add readout channels, but only additional fibers. This approach will be considered seriously only if forthcoming bench tests demonstrate clearly that addition of a second readout fiber does not cause significant resolution deterioration for the full tower sum.

5.5   Diagnostics and Quality Control

Quality control tests will be performed during manufacture of all active components and diagnostic systems will be built into the assembled detector for online tests. Records of all tests will be stored in a data base for future reference.

For the megatile scintillators the delivered scintillator sheets will be checked for thickness variations. Samples will be cut off the sheets in unused corners for light output testing. The completed megatiles will be tested tile by tile for light output and crosstalk with a radioactive source and PMT running in current mode. The tiles are required to have <10% rms light output deviation in order to limit the stochastic term in the energy resolution to the required value. The light output characteristics of the WLS fiber are measured after the procedures of mirroring, gluing in the connector and polishing are complete. The clear fiber bundles are also tested for light transmission after gluing in the connector and polishing. It is expected that the rms variation will be about 2.5% of the average transmission. Cables with any fiber deviating by more than 10% will warrant inspection and possible reworking. Photomultiplier tubes will also be tested for gain characteristics before installation.

Final testing after assembly will be done with cosmic rays. The detector will be left in the horizontal position and existing wire chambers and scintillators will be used to trigger and track cosmic rays into a subsection of the detector. This subsection of the detector will be multiplexed

into an array of 24 phototubes so that individual tiles can be read out. A similar test setup is currently being developed at IUCF for the testing of completed barrel EMC modules.

A number of diagnostic devices will be built into the detector and readout systems. A tube for inserting a radioactive source will be placed in the fiber routing layer of each megatile. This will allow a source to be inserted above any individual megatile by hand for testing. (We do not envision automatic insertion for calibration purposes.) An LED system will be used to pulse the phototubes as a diagnostic of tubes and electronics. This will monitor drifts of the phototubes and associated electronics independently of the scintillator and fibers. As described previously, the PMT boxes on the poletip will each have at least one diagnostic PMT of sufficient gain and resolution to see a clear single photoelectron peak in the response. A 12-fiber connector will connect to this tube, to allow diagnostics on individual tiles in one megatile, the multiplexing being decoded with the help of the remaining 23 tiles in each tower.

With these systems we believe we can deliver a calorimeter that meets requirements and maintain it over the years.

6 Shower Maximum Detector

6.1 Performance Simulations and Choice of Scintillating Strips

As explained in Sec. 3.2, state-of-the-art performance in γ *vs.* π^0 discrimination, at least up to energies ~ 40 GeV, is *critical* for attaining the primary physics goal of determining ΔG for the proton. For this reason, the performance simulations and bench tests on which we have based our choice of technology and the detailed design for the proposed shower-maximum detector (SMD) are important to describe in some detail. We have concentrated in these simulations and tests on scintillating strips, as opposed to gaseous counters, because of the experience in other collider detectors [34, 47] that the shower profiles measured with gaseous counters are always considerably broader than simulations. Gaseous SMD's have provided useful γ/π^0 discrimination up to perhaps 20 GeV [34], but not beyond. This experience is consistent with the (cost-driven) choice to use a gaseous SMD in the barrel EMC for STAR, where the vast majority of direct photons of interest have energies below 20 GeV. But for the endcap, the higher photon energies, the reduced coverage, and the concentration on $p-p$ and $p-A$ (but not $A-A$) collision occupancies, make a scintillator SMD a clear, and economically feasible, choice.

The basic idea of an SMD is to obtain a good measurement of the transverse shape of an electromagnetic shower, in order to distinguish events arising from a single photon from those induced by a pair of closely spaced photons, produced in the decay of a high-energy neutral meson. One method of making this distinction is to perform a moment analysis of the SMD response [48]. As has been shown previously, algorithms based on moment analyses of SMD data for a single event work well below $E \sim 10$ GeV, but are not as effective above ~ 20 GeV, because of the smaller spatial separation between the two photons from π^0 (η^0) decay and the shower-to-shower fluctuations of the transverse profile for different events.

An alternative method for analyzing the SMD data is to attempt *peak fits* to establish whether one or more than one photon initiates the electromagnetic shower. Thus, we have analyzed GEANT simulations of the energy deposition for single photons and π^0's in scintillating strip arrays, by attempting to fit each shower profile with a *single lineshape* consistent with the average simulated response to a single photon. For example, Fig. 32 shows the average energy loss in two orthogonal SMD strip layers for 30-GeV single photons normally incident on the EEMC. For this particular simulation, the SMD was positioned just after the fifth EEMC converter layer. It comprised long plastic scintillating strips of triangular cross section, similar to those developed for the D0 preshower detector [36] and to those illustrated in Fig. 37. In cross section, each strip was assumed to have a triangular base of 1 cm and an apex height of 4 mm, similar, but not identical, to the geometry we have finally chosen. The strips have orthogonal orientations in the two planes (labeled u and v) of the SMD.

The average energy deposited in the u (v) plane, integrated over all strips, is 74 (72) MeV for a normally incident 30-GeV photon and 4 mm thick layers. The v plane sees slightly less energy, and correspondingly, a slightly broader transverse profile, because the u plane in front of it absorbs the low-energy electron component of the shower and introduces appreciable multiple scattering. The average energy deposition in both planes increases roughly linearly with $\sqrt{E_\gamma}$, consistent with the statistical variation in the number of secondaries: for example, a normally incident 90-GeV photon deposits an average energy of 144 MeV in the u-plane. The transverse shower profile can be fitted by the sum of three common-centroid Gaussians, with independent widths and scaling. The narrowest Gaussian has $\sigma \approx 0.5$ strips, while that for the second Gaussian is ≈ 3.1 times greater. As seen in Fig. 32, this gives a reasonable description of the simulated transverse profiles.
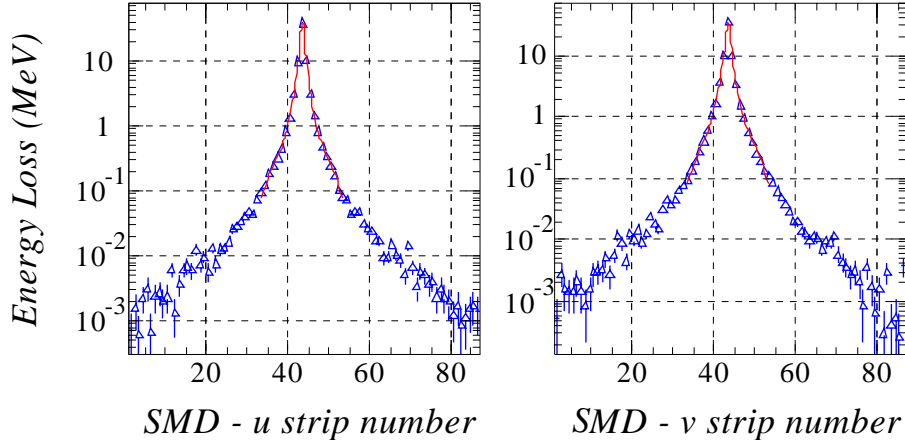
Figure 32: *Simulated response of the SMD to monoenergetic 30-GeV photons normally incident at the center of an EEMC tower. Plotted is the average energy loss in MeV through the SMD u and v planes. The v plane is assumed to sit directly behind the u plane, while both are located after the fifth converter sheet of the EEMC.*

Better descriptions of the average profile are available, but are not suitable for the analysis of the SMD profile from *single events*, where the extended tails in the average profile are not uniformly populated. These tails arise from the small probability for large-angle bremsstrahlung, producing small secondary peaks which can be significantly displaced from the primary energy deposition in the individual-event profiles. In the average response, this secondary peak structure is smoothed into extended tails.

In simulating the SMD response to individual photons and π^0, the assumed light output from the strips, and consequent limitations from photoelectron statistics, are critical. In the simulation results presented below, we have assumed that a MIP traversing the maximum height of one triangular strip would yield two photoelectrons, on average. (Bench tests on prototype strips, described in Sec. 6.4, indicate that we should be able to surpass this estimated output. For added margin, we have decided to use an apex height of 5 mm in the EEMC, as opposed to the 4 mm height assumed in the simulations.) The actual number of photoelectrons generated for a given strip in a given event is chosen randomly by Poisson statistics from a distribution consistent with the appropriate average, and the resulting pulse height is generated randomly by applying a Gaussian MAPMT response to each photoelectron. Thus, the important effects of photostatistics are fully included in the simulations.

Typical simulated EEMC and SMD pulse heights for individual 30-GeV photon and 30-GeV π^0 events are shown in Fig. 33. It can be seen here that shower-to-shower fluctuations, combined with limited photostatistics, can often give rise to small apparent secondary peaks in the transverse profile even for single photons. These fluctuations, together with the occurrence of very asymmetric π^0 decays, provide a fundamental limit to the γ/π^0 discrimination. The limited statistical precision further implies that the event-by-event profile analysis cannot support fits with as complicated a lineshape as used in Fig. 32 to fit the *average* single-photon response, or with two independent peaks. Thus, we have fitted each simulated shower profile with a single lineshape, taken as the sum of *two* common-centroid Gaussians with adjustable widths (within limits) and amplitudes.
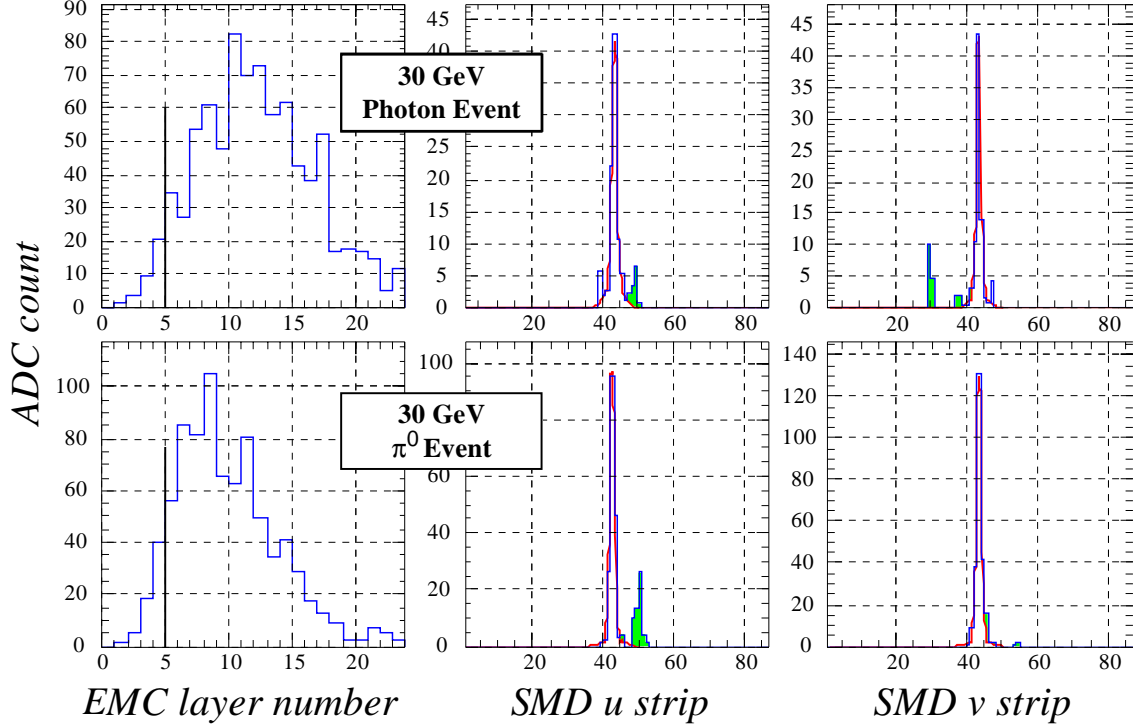
Figure 33: *Simulated ADC output from the EEMC and the SMD u, v planes for a normally incident 30 GeV photon (top) and a 30 GeV π^0 (bottom). The vertical line in the plots on the left indicate the position of the SMD within the stack. The π^0, in this particular event, decayed into 26.5 GeV and 3.5 GeV photons, with an opening angle ≈ 14 mr. The plane of the decay happened to be perpendicular to the SMD u strips, so that no secondary peak is seen in v. The particular γ event considered has a small secondary peak due to bremsstrahlung. The fitted lineshape in each case is similar to that found for the average SMD response to a single photon, but with parameters adjusted to best fit the data for the single generated event. The shaded portion of the SMD response in each case shows the 'sided' fit residual defined in the text.*

We then perform a 'sided' moment analysis of the fit residual distribution, defined by:

$$\mu_t - 40 < t < \mu_t - 2\sigma_t \ \Rightarrow \ R_-(t) \equiv D(t) - F(t);$$

$$\mu_t + 40 > t > \mu_t + 2\sigma_t \ \Rightarrow \ R_+(t) \equiv D(t) - F(t);$$

where t refers to either of the two transverse coordinates measured by the SMD (u, v); μ and σ are the centroid strip number and 'narrow' Gaussian rms value from the single peak fit; $D(t)$ refers to the data and $F(t)$ to the fitted values for strip numbers within the indicated ranges; and $R_\pm(t)$ are then the sided residual distributions. The maximum zeroth moment from each SMD plane, $R_{0,t} = \max[R_{0+,t}, R_{0-,t}]$, is then found and is used to discriminate between direct γ events and direct π^0 (η^0) events. The integration range used to determine $R_{0\pm}$ is important to consider. The range must be large enough to distinguish between single and di-photon events that are within the same EEMC tower. However, extending the range too far could result in too high an average occupancy in the SMD region involved in the discrimination, causing loss of direct photon events.

52

Figure 34 shows the discrimination between single and di-photons via the correlation between the zeroth moment of the SMD sided fit residuals, summed over the u and v planes (*i.e.*, $R_{0,u}+R_{0,v}$), and the integrated pulse height in the fitted single peaks, again summed over u and v. The events populating these histograms were generated by PYTHIA for the $pp \to \gamma + jet + X$ and $pp \to \pi^0(\eta^0) + jet + X$ reactions at $\sqrt{s} = 200$ GeV, subject to the cuts indicated in the middle frame of Fig. 11, but otherwise spanning the entire STAR detector and relevant particle energy ranges. A two-dimensional gate on this correlation, such as that indicated by the curves in Fig. 34, is capable of rejecting 80% of the mesons, while retaining 80% of the single photons. The net effect on background reduction is shown in Fig. 11.
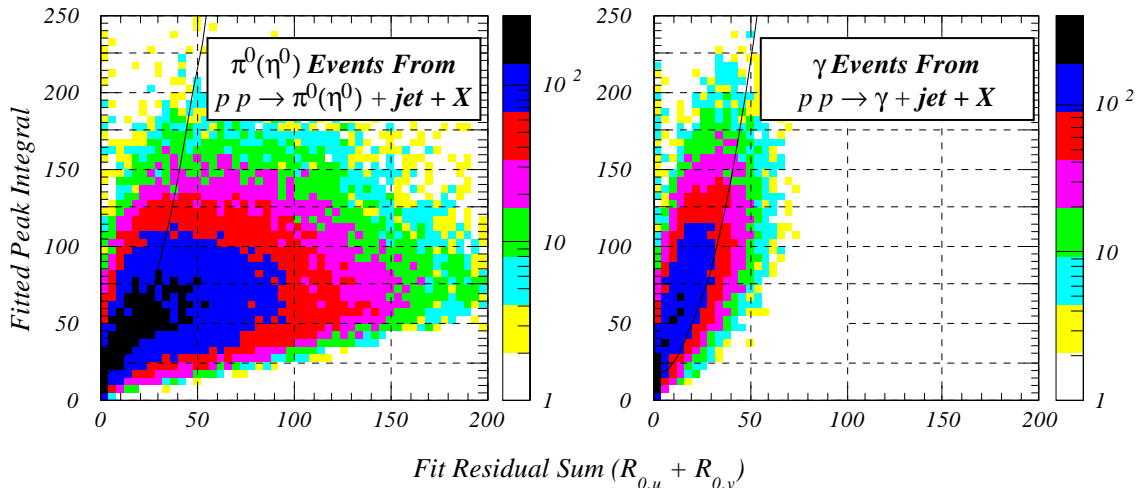

Figure 34: *The two-dimensional distributions of SMD response used in the analysis to distinguish between γ and π^0 (η^0) events detected in the EEMC, following the algorithm described in the text. Events were generated for the two reaction types shown corresponding in both cases to an integrated luminosity of 43 pb^{-1}. Only events satisfying all the kinematic cuts indicated in Fig. 11 are included in this figure. The curve shown was used as a cut to identify the neutral mesons, in order to end up with the final meson/photon ratio shown in the bottom frame of Fig. 11.*

Figure 35 shows the distribution of relative energy sharing between the two photons for those π^0 (η^0) events that pass the SMD photon identification based on the solid curve in Fig. 34. The distribution is sharply peaked at the energy sharing variable $z_\gamma = \pm 1$, corresponding to maximal asymmetry in the energies of the daughter photons. This indicates that the *fake direct photons* from neutral meson decay are the cases that most closely resemble real single photons, since one photon from the meson decay is of quite low energy. There is little in the detailed design of the SMD that can significantly reduce this source of confusion: very asymmetric meson decays closely resemble single photons whose showers include a small secondary bremsstrahlung peak.

On the other hand, the smooth background in Fig. 35 near $|z_\gamma| \approx 0$ corresponds to fluctuations in the depth at which one of the two photons first converts into an e^+e^- pair. Clearly, this problem could be alleviated, while simultaneously improving the statistical definition of the shower profiles, by placing the SMD deeper within the EEMC. However, counteracting this improvement is the growing width of the showers vis-a-vis the spatial separation of the two daughter photons. To decide on the optimal depth and the energy range over which the SMD will be useful for γ/π^0
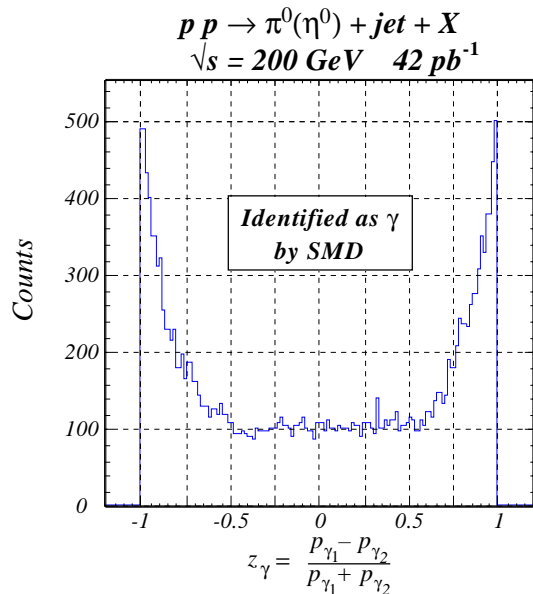
p p → π⁰(η⁰) + jet + X
√s = 200 GeV   42 pb⁻¹

Figure 35: *Photon energy sharing distribution for* π^0 (η^0) *mesons that pass* all *cuts (including SMD) identifying them as direct photons.*

discrimination, we have performed simulations for a number of depths, incident energies and η-values. The results, a sample of which are shown in Fig. 36, suggest an optimal depth somewhere between the 5th and 6th layers; since these simulations did not properly account for non-normal incidence, or for the material in STAR upstream of the EEMC, we have chosen the position after the 5th radiator sheet (see Fig. 26) for our EEMC design. To simplify the comparison in Fig. 36, the optimal cut for distinguishing photons from neutral mesons has been adjusted (slightly) for each incident energy and SMD depth, in order to maintain a constant γ retention fraction. We observe that the simulated gain of a factor ≈ 4 in meson/photon ratio provided by the SMD for $E_\gamma \lesssim 40$ GeV deteriorates to a factor of 2–3 at 50 GeV, and rapidly for still higher energies. Thus, the preshower detector remains important for background subtraction at the photon energies corresponding to $x_{gluon} > 0.05$ at $\sqrt{s} = 500$ GeV.

Additional simulations have been performed to compare the performance of scintillating strips with rectangular *vs.* triangular cross section (keeping the total channel count constant, *i.e.*, considering rectangular strips of 5 mm width). The triangular cross section provides slightly better performance. This is understood to arise from that fraction of single photon events where the peak shower energy deposition (corresponding to the 'narrow' Gaussian used in the fits) falls essentially completely within a single rectangular strip, complicating the peak fitting. The triangular geometry ensures energy sharing between at least a pair of adjacent strips for all events, and thus acts to stabilize the fitting lineshape needed.

6.2   Strip and Fiber Layout and Assembly

Based on the simulations described above, we have converged on the SMD design illustrated in Fig. 37. It is to be made from extruded plastic scintillator strips of triangular cross section (1 cm base by 0.5 cm apex height), organized into orthogonal u and v planes. Light from each strip will be transported through a 0.83-mm diameter WLS fiber that runs axially along its length, through a 1.0-mm diameter hole created during the extrusion. Scintillating strips of similar design have been developed and used successfully by D0 [36] as a tracking preshower detector. In D0 the strip readout is done with Visible Light Photon Counters (VLPC), resulting in output exceeding
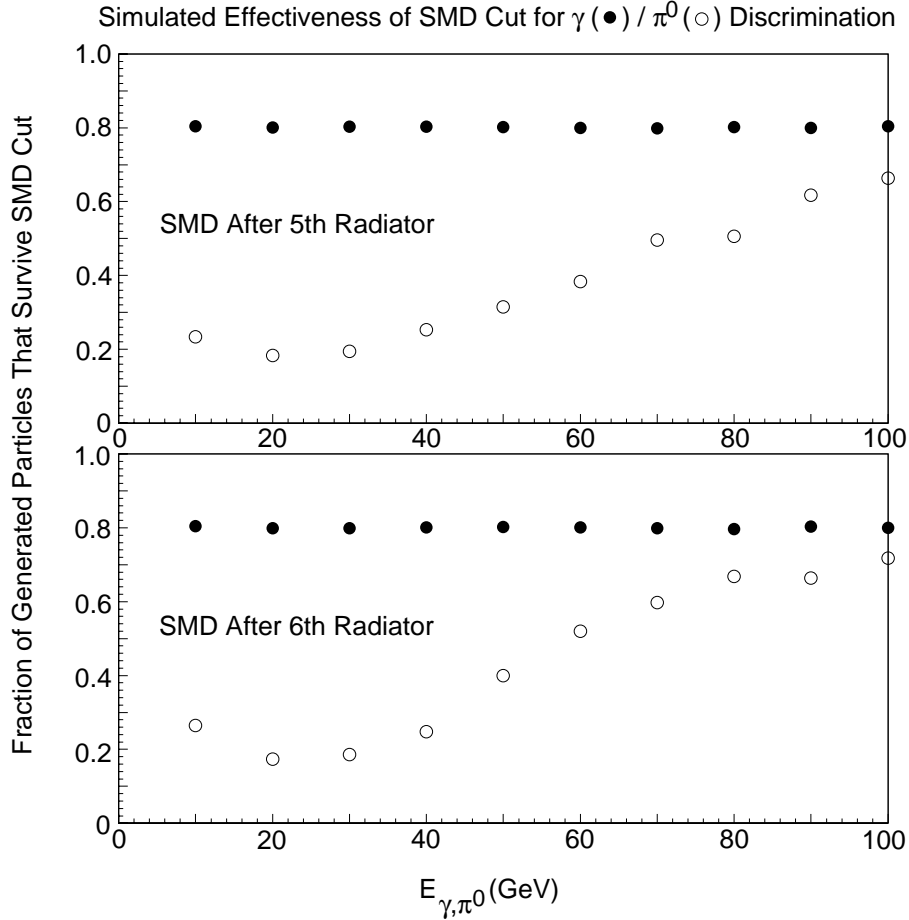
54

Figure 36: *Simulation results for the fraction of γ's and of π⁰'s that survive the SMD cut, as a function of particle energy and at two different SMD depths within the EEMC. The SMD cut has been adjusted in each case to retain a constant 80% of the γ's. The results here correspond to η = 1; near η = 2, the π⁰ suppression is slightly worse at the lower energies, but slightly better at the highest energies included in the figure.*

10 photoelectrons per MIP traversing the thickest part of the triangular cross section. Such good photostatistics are essential to reap the benefits of the excellent position resolution available, in principle, from the energy sharing of a MIP between adjacent strips. In our application, any such use of the strips for tracking individual MIP's is secondary, so excellent position resolution is less of a concern than stable characterization of electromagnetic shower profiles, where many MIP's are involved. Hence, we are able to accept the lower quantum efficiency associated with multi-anode phototube (MAPMT) readout ($\approx 20\%$ *vs.* $\approx 80\%$ available with VLPC's).

Maintaining an angle of 90° between the strip orientations in the two SMD layers maximizes the likelihood of detecting the second photon shower from a neutral meson decay (*e.g.*, see Fig. 33), hence, optimizes the γ/π^0 discrimination. For ease of assembly, and to limit the strip lengths, the SMD scintillators will be segmented into 30° sectors, as shown in Fig. 37. In order to maintain as much symmetry as possible between the u and v layers, the two planes will normally be laid out with $\pm 45°$ strip orientation with respect to the radial line bisecting each sector. This arrangement
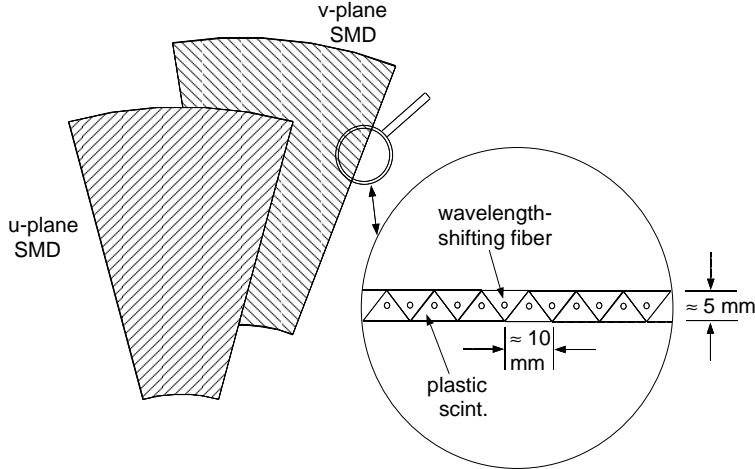
Figure 37: *Schematic layout of one 30° sector of the proposed SMD. Each of the two orthogonal planes will be constructed from triangular scintillating strips extruded with an axial hole for the wavelength-shifting fiber.*

requires a total of 300 strips per layer per sector, the longest of which are 126 cm. The proposed budget allows for all sectors to be constructed in this way, giving a total SMD channel count of 7200 (although our present plan – see below – calls for a somewhat different strip layout and slightly lower channel count in the end sectors of an EEMC half). The number of elements per plane of the SMD is thus five times greater than the number of EEMC towers, but a typical shower will yield appreciable pulse height in 5-10 strips within each plane; hence, occupancies in the SMD strips and in the EEMC towers will be comparable, both small for $p-p$ and $p-A$ (but not for $A-A$) collisions.

Strips that terminate near the structural tie rods, spaced periodically along the dividing lines between adjacent sectors, will have to end a little early to permit routing their fibers around the tie rods, leading to a very small dead space in the SMD layer. Other very small dead spaces will be introduced by eliminating the few scintillating strips in each layer that would have lengths under 5 cm, where the light output becomes marginal.

Roughly half of the WLS fibers for the SMD will exit their respective strips at the outer circumference ($\eta = 1.07$) of the sector, but the remaining half will exit at the radial edges that form the dividing lines between adjacent sectors. The latter fiber runs necessitate a depth alternation between adjacent sectors of the SMD, and a change in fiber-routing scheme for the two sectors that form the ends of a 180° half-annulus of the EEMC. As illustrated schematically in Fig. 38, the staggering in depth by several mm allows fibers from one sector to be routed to the outer circumference through a plastic fiber guide seated just below or above the neighboring layer of scintillating strips. In the scheme illustrated, all fibers exit their strips in the "natural" direction, headed toward the outer circumference, *i.e.*, toward the clockwise (counterclockwise) adjacent sector for the u (v) plane, as labeled in Fig. 37. This layout maintains complete symmetry between the u- and v-plane fiber runs until one reaches the end sectors, where the symmetry is unavoidably broken.

The end SMD sectors in each EEMC half have to be treated differently than the rest, in order to avoid fiber runs beyond the ends of the azimuthal range of the half. The current plan for these sectors, as illustrated in Fig. 39, is to reorient the scintillating strips to run at +15° and −75° with respect to the radial bisector, rather than at ±45° as in all other sectors. The fibers in one plane ($v1$ and $u6$ in Fig. 38 and Fig. 39) then all exit at the outer circumference, while in the other plane ($u1$, $v6$), a small number exit at the outer circumference, but most exit into the natural
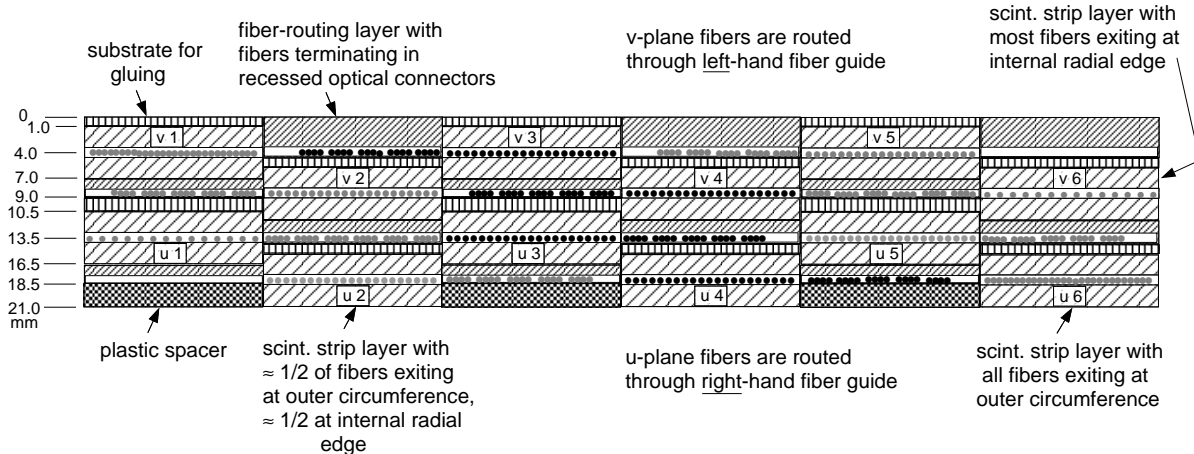
56

Figure 38: *Schematic depth layout (not to scale) of the SMD layer for one EEMC half-annulus. The drawing shows both the active scintillator layers (broad diagonal cross-hatching) and the plastic fiber-routing layers (fine diagonal cross-hatching) with which they alternate. Active layers in adjacent 30° sectors are staggered in depth to facilitate the fiber routing. The fiber-routing guides will have machined or extruded grooves in which the fibers are inserted. Fibers are represented in the diagram by the small filled circles, with black-grey color coding to facilitate identification of the association between fiber-routing layers and scintillator layers. Also shown are 1.0-1.5 mm thick aluminum substrates (vertical cross-hatching) envisioned for mounting the scintillating strips during their assembly, and plastic spacers (checkerboard pattern) to fill out the depth. The special fiber layouts needed in the end sectors (1 and 6) are described in the text.*

fiber-routing guide. The total number of $u + v$ strips in each end sector would then be reduced from 600 to 520. Advantages of this overall fiber-routing scheme are that it (1) avoids overcrowding of fibers within any fiber guide, (2) avoids sudden reversals in the direction of light flow between adjacent strips within a common sector, (3) avoids fiber-routing at the inner circumference, near the detector hub, and (4) maintains a reasonably constant fiber length, within the range 1.3–1.7 m from mirrored end to outer circumference, for all the fibers that exit at radial edges from all sectors.

There are also some potential disadvantages of the proposed fiber-routing scheme. We need to simulate the effect of occupancy distribution changes caused by the proposed reorientation of strips in the end sectors, to make sure that they do not cause deterioration in the γ/π^0 discrimination. The large number of fibers that would exit their strips directly at the outer circumference, leading to short individual fiber runs beyond the outer circumference, might be susceptible to damage during assembly. In contrast, the fibers routed through the fiber guides will terminate in "protected" optical connectors recessed just inside the outer circumference, and only more robust fiber bundles will exit the active volume. (The fiber guides and aluminum substrates indicated in Fig. 38 will end a couple of cm before the outer circumference to allow for mounting of these recessed, 3.5-mm thick, optical connectors.) We are also considering other possible fiber-routing schemes, which would address the above potential drawbacks, but introduce different problems.

We presently envision the fiber runs from the strips to the outer circumference of the SMD layer to be done entirely with wavelength-shifting (WLS) fibers. The maximum length run is 1.7 m, and the resulting attenuation should still allow us to exceed the 2.0 photoelectrons/MIP assumed in our

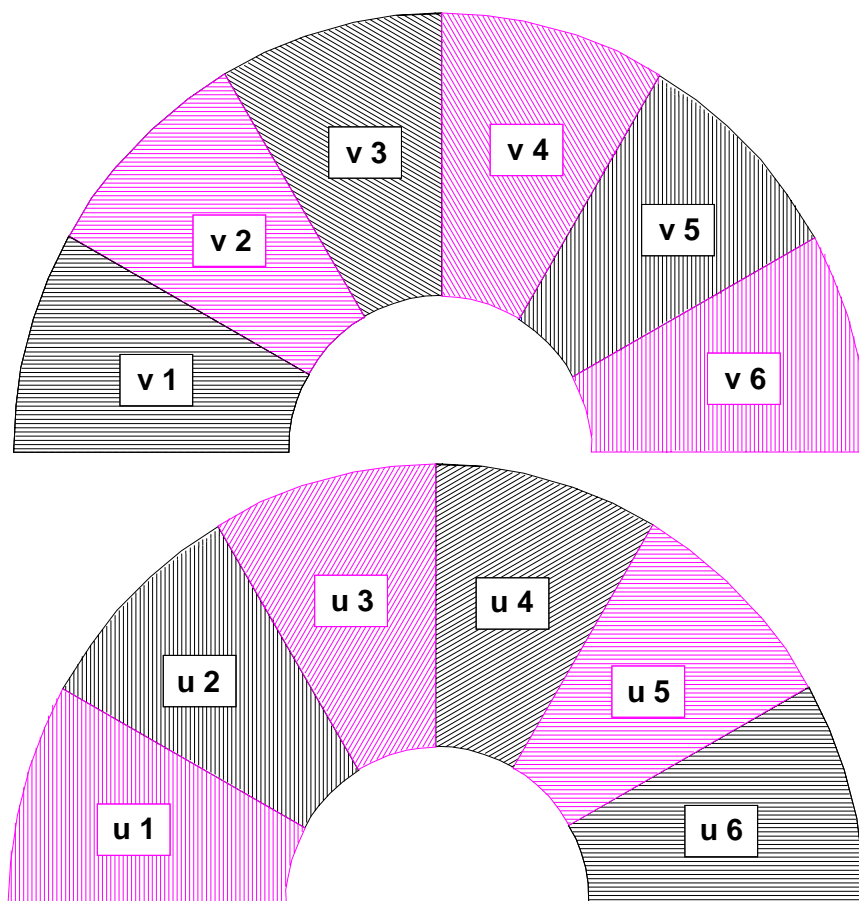**SMD Strip Layout for One Half EEMC**

Figure 39: *Schematic layout of the scintillating strips within each sector of one EEMC half-annulus, illustrating the proposed change in orientation in the end sectors. This scheme allows all optical fibers to exit either at the outer circumference or at an internal radial sector edge, but headed toward the outer circumference.*

SMD simulations. (See Sec. 6.4 for an account of measured light output for the proposed strips, fibers and phototubes.) However, as the design is finalized, we will consider the possibility of fusing clear fibers to the WLS fibers shortly after they exit the scintillating strips, if necessary to limit light attenuation. The WLS fibers routed through the plastic fiber guide layers will terminate in optical connectors recessed just inside the active SMD volume. Those exiting at the outer circumference of the scintillating strip sectors will terminate at connectors located within the fiber-routing volume at $\eta < 1.07$, slightly outside of the SMD volume and closer to the back edge of the EEMC. In both cases, we will use the same design of 12-fiber optical connectors (see Fig. 28) to be used for all the fibers from scintillating tiles. From these connectors, the light will be further transported to MAPMT's mounted on the outer surface of the STAR poletip via clear 0.93-mm diameter optical fibers. The clear fibers will be bundled in ribbons that run along the outer edge of the EEMC in the manner described in Sec. 9. The SMD fiber ribbons will be attached after all deeper megatiles have been inserted into the EEMC, and will run above the fiber ribbons from the deeper megatile layers and below those from layers nearer the front.

As shown in Fig. 38, a total depth of 21 mm is allowed for the SMD. This budget assumes that each scintillating layer, once wrapped, assembled and glued, will have a depth of 6 mm, plus 1.0-1.5 mm additional for a substrate used to hold the strips in place during the gluing. Adjacent sectors are offset longitudinally by 4.5-5.0 mm to allow for fiber routing and recessed optical connectors, sandwiched within the fiber routing space near the outer circumference. Fibers from a given sector will normally occupy about half the azimuthal range in the adjacent fiber-routing space.

The "interlocking" nature of the SMD sectors indicated in Fig. 38 necessitates assembly of the SMD layer as a whole with the EEMC mechanical structure horizontal, but the front five layers of radiator removed. First, the deepest active layers and their adjacent fiber routing layers ($v1$, $v3$, $v5$ in Fig. 38) must be laid down. After all the fibers from these layers are properly inserted in their respective grooves, the fiber-routing guides will be covered, and the next layer can be laid down, and so forth. This assembly procedure implies that the SMD will not be easily removable from the fully assembled EEMC, as will individual megatiles.

6.3   Multi-Anode Photomultiplier Tubes

The SMD scintillating strips will be read out via 16-anode phototubes (MAPMT's) that will, like the single-anode tower phototubes, be mounted on the outer surface of the STAR poletip. The more modest resolution, gain-matching and linearity demands of the SMD, compared with the towers, permit this efficient solution for handling the high channel multiplicity. The 7200 strips envisioned for the SMD u and v planes combined will require a total of 480 MAPMT's (40 per sector), since we envision devoting one anode per tube to a light-pulsing input for diagnostic purposes. (An additional 96 of the same model MAPMT's will be used for the preshower detector readout.) MAPMT tests performed previously for CDF [49] and HERA-B [50], as well as our own tests, show that the Hamamatsu H6568 tube should meet our requirements. In particular, initial bench tests performed with extruded plastic scintillating strips of approximately the geometry we intend to use, the relevant wavelength-shifting optical fibers, and Hamamatsu H6568 MAPMT's, have demonstrated (see Sec. 6.4) that this arrangement should yield typically 2–3 photoelectrons (after further attenuation in clear fibers and optical connectors) per MIP traversing the apex height of the triangular strips, providing adequate photostatistics for our planned SMD application.

The Hamamatsu H6568 MAPMT has a bialkali photocathode with the anode divided into 16 pads of 4×4 mm^2 each. The tube is of the head-on type, with a metal envelope at the cathode potential. The outer dimensions of the PMT are 30×30 mm^2 and 45 mm deep. The

12-stage metal channel plate dynode system allows for good single-photoelectron resolution. The quantum efficiency of the H6568 photocathode with borosilicate window has a broad plateau in the wavelength region between 300 and 500 nm, with a maximum value of 20%. The tube can be operated with negative high voltage for DC-coupled anode output, with gain as high as 1.5×10^7 at the maximum operating voltage of 1000 V. The other PMT characteristics, such as dark current (1 nA), pulse rise time (0.8 ns) and transit time spread (0.3 ns) are also satisfactory.

The previous studies [49, 50], as well as our own measurements, have demonstrated that the response of a single PMT anode to light from a 1 mm diameter optical fiber is uniform within 10% when the fiber is moved within a 1.5×2.0 mm^2 region of the corresponding photocathode pixel. Pixel-to-pixel gain variations are manageable: the minimum pixel response was 56% of the maximum pixel response. Mean crosstalk has been measured as 0.7% between nearest neigbor anodes and only 0.2% between diagonal neighbors.

The Hamamatsu tube comes with a built-in base. We will use the commercial C.A.E.N. SY527 high voltage distribution system to provide bias to the 576 (SMD + preshower) MAPMT's. The anode output signals from each tube are provided at two 16-pin connectors.

The technology of MAPMTs continues to develop. Most recently, Hamamatsu has begun marketing the H7546, a 64-anode MAPMT, having a cost per channel that is significantly less than for the H6568, described above. To assess the suitability of this new MAPMT for our application, comparisons of the performance of the Hamamatsu H7546 (64-anode MAPMT) and the Hamamatsu H6568 (16-anode MAPMT) were made. For the tests, a wavelength shifting optical fiber was inserted into a triangular cross section scintillator strip, and electrons from a collimated ^{90}Sr source were used to produce scintillation light. The optical fiber was aimed at the center of different pixels of each MAPMT, enabling measurement of the total charge produced by the associated anode, and the neighboring anodes (crosstalk). From these tests, the following was found:

- The single photoelectron resolution was more than two times better for the H6568 than for the H7546.

- There was evidence for variation of the quantum efficiency across the face of the H7546, whereas the quantum efficiency was constant for the H6568.

- The two tubes exhibited comparable crosstalk probability, but the average crosstalk *amplitude* was found to be larger for the H7546 than for the H6568.

In addition, the alignment tolerance of the optical fiber relative to the pixel must be better for the more densely packed 64-anode MAPMT than for the 16-anode tube. For these reasons, the 16-anode MAPMT has been chosen for the readout of the SMD and the preshower detector.

6.4 SMD Prototype Tests

We view the SMD as a critical component of the EEMC, which must perform at state-of-the-art levels to attain the physics goals of the proposed ΔG measurement. Extruded plastic scintillating strips of essentially the geometry we propose have been used successfully by the D0 experiment [36], but with different readout and for a different purpose. We therefore view it as essential to perform early beam tests of the γ/π^0 discrimination capability of our planned SMD with the MAPMT readout. For this reason, we have already obtained a number of suitable scintillating strips, wavelength shifting fibers, and MAPMT's for bench tests of performance with radioactive sources and cosmic rays. We are currently fabricating a prototype of a small section of the entire EEMC, including an SMD region comprising 160 SMD strips, and making arrangements for beam tests of

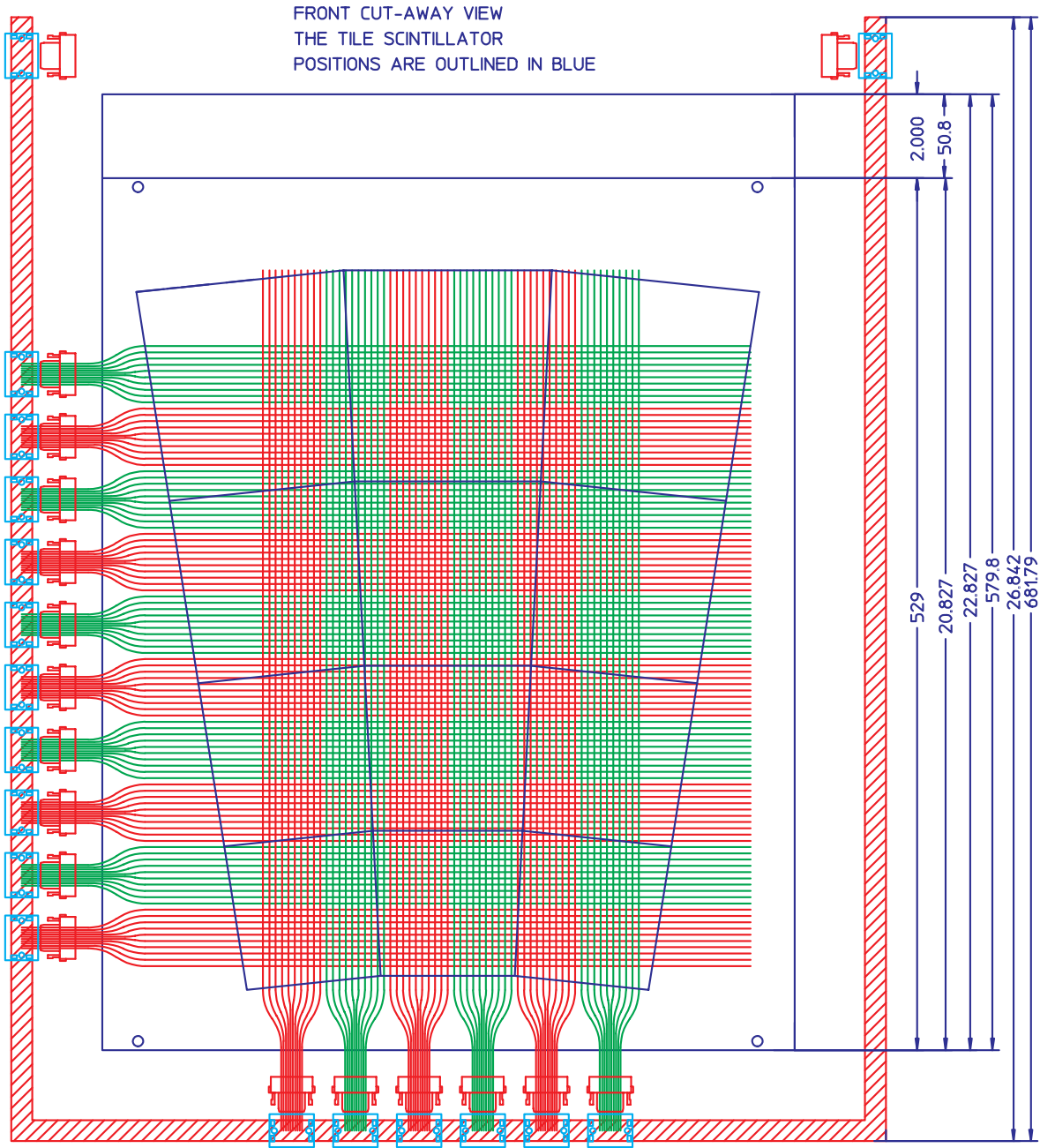Figure 40: *Schematic layout of one layer of the prototype EEMC section currently being fabricated. Superimposed on the 3 × 4 tile structure is the wavelength shifting fiber layout for light collection from the SMD strips. The SMD strips comprise two orthogonal planes of extruded plastic scintillating strips of triangular cross section, covering most of the active area of the scintillating tiles.*

this device during summer, 1999. The beam tests will be carried out at Jefferson Laboratory in parasite mode, using the scattering of a tagged 5.5 GeV photon beam. The scattering, triggered by a recoil detector set up for the JLab RADPHI experiment, will provide a sample of several GeV photons and π^0's incident on the EEMC prototype, which can be used to calibrate simulations of the entire EEMC, but especially the SMD, performance.

The layout of the prototype detector layers is shown in Fig. 40. It consists of a 3×4 tower section of the EEMC, corresponding to the four η segments closest to $\eta = 2$. The η segmentation was based on an earlier design for the entire EEMC; thus, it corresponds closely, but not exactly, with the tile sizes described in Sec. 5 of this report. The 3×4 section provides two towers that are completely surrounded by active detector, thereby allowing us to evaluate transverse shower leakage. Simple Pb sheets, without the proposed stainless steel laminate, will be used as the radiators in this prototype. The 12 scintillating tiles within each of the 24 layers of the prototype are being prepared with the same sort of megatile construction envisioned for the full-size EEMC, providing some initial experience in carrying out the relevant machining at IUCF, where the eventual megatile machining will take place. The prototype SMD (see Fig. 40) will contain 60 x by 100 y strips, sufficient to test simulations of SMD performance, although they will not have quite the same orientation with respect to the tower structure as planned in the full-size EEMC.

Measurements of the light output of the triangular strip scintillators have been performed using cosmic-ray muons. A side view of the apparatus used for the tests is shown in Fig. 41. A hardware trigger is generated by a fast coincidence between the anode signals from PMT's detecting light from scintillators A and B. Timing information from the delay-line-readout multiwire proportional chambers and pulse heights from A,B and the test scintillators are recorded for each event. Tracking of cosmic ray muons is performed in the analysis software, enabling coarse localization of the position at the test scintillator and the angle of incidence.

The response of triangular cross section scintillator strips (obtained from the D0 group) to incident cosmic ray muons has been measured. The material we received has a transverse profile in the shape of an equilateral triangle, with the apex-to-base distance of 0.5 cm. The strips are wrapped in two layers of 25 micron thick aluminized mylar, to reflect scintillation light produced by ionizing radiation. The scintillation light is collected by a 0.83-mm diameter WLS optical fiber inserted through a hole running axially through the scintillator, formed during the extrusion process. The 130-cm long WLS fibers are mirrored at one end; the other end is mounted directly onto a single-anode Burle 83101 PMT. For the tests, four 43-cm long scintillator strips were mounted in a pyramid structure within a light-tight box, as shown in Fig. 41. The advantage of this scheme is its ability to select incident cosmic rays that primarily go through the thickest part of the triangular strip.

Figure 42 shows the pulse height distribution for the top strip within the pyramid under two different sorting conditions. The distribution in the upper half of the figure requires no pulse height in the L, R or B scintillators. For these events, most of the time, no pulse height is observed in the T scintillator. For 0.5% of these events, the dark current response of the T PMT is accidentally coincident with the cosmic-ray trigger. The resolution in the single photoelectron response of the PMT is clearly visible. In the bottom half of Fig. 42, events are selected requiring non-zero pulse height in the B strip, and no pulse height in strips L or R. This sample predominantly corresponds to cosmic rays traversing the T strip from its apex to its base. These distributions are well represented by a Poisson distribution, establishing the probability of observing n photoelectrons for a given mean number N, convoluted with a Gaussian distribution representing the response of the PMT to n photoelectrons. By fitting such a function to the measured data, the mean number of photoelectrons corresponding to a minimum ionizing particle traversing the thickest part of the
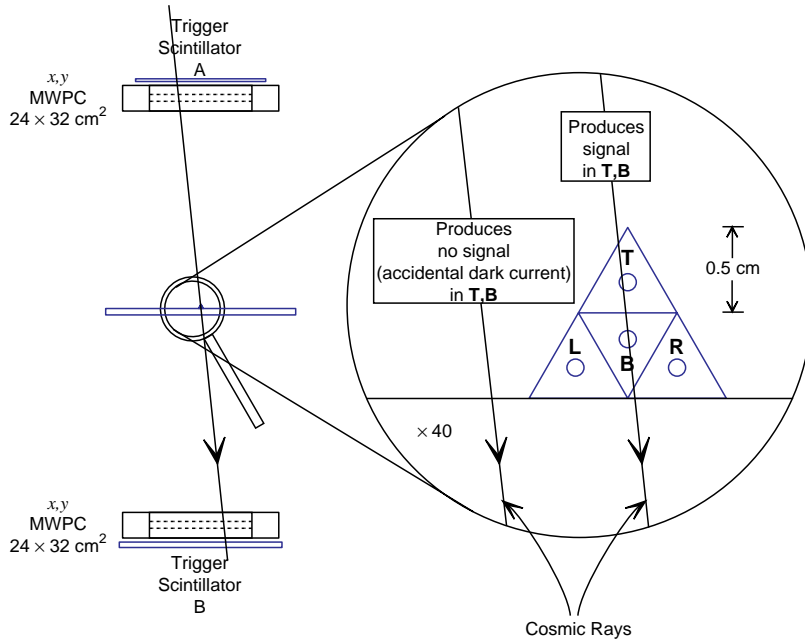
Figure 41: *Schematic of a test stand used for testing scintillating strip detectors planned for the shower-maximum detector. Scintillation light is collected from the strips using wavelength-shifting optical fibers, mirrored at one end. Tracking of cosmic rays is performed using delay-line readout multi-wire proportional chambers. The transverse profile of the scintillating strip layout used in the tests described below is also shown. The test stand has also been used to examine light output from single scintillator tiles and megatiles.*

63

scintillating strip is deduced to be 5.09 ± 0.04.

Figure 42: *Results from cosmic ray tests of the light output from triangular cross section scintillating strips, in the geometry shown in Fig. 41. In both panes, the pulse height from the T strip is shown under different sorting conditions. (Top) The T pulse height distribution for events with no pulse height in the B, L or R scintillators. The pulse height distribution corresponds to dark current in the PMT, accidentally coincident with the cosmic-ray trigger. (Bottom) The T pulse height distribution for events with no pulse height in L or R, and large pulse hei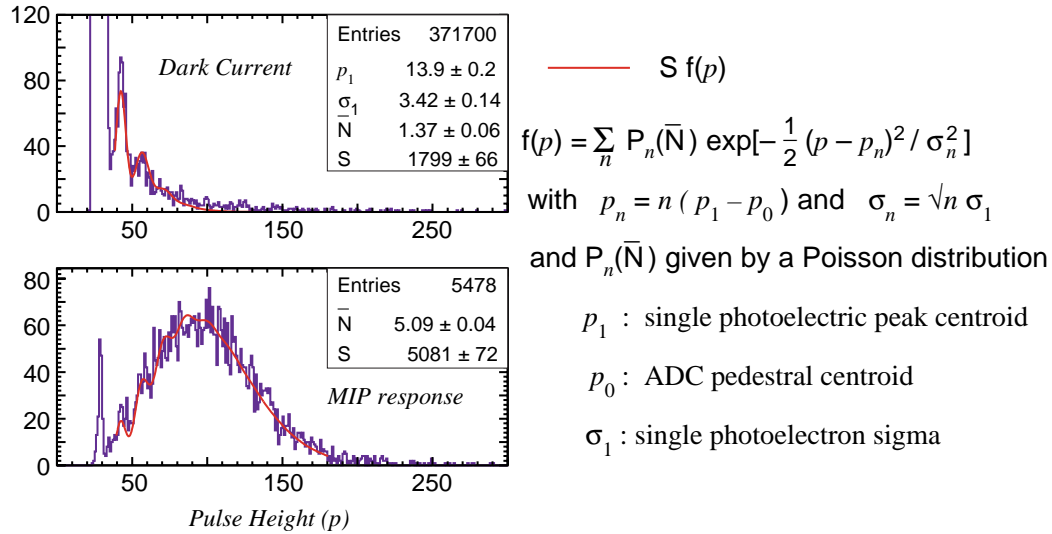ght in the B strip. These requirements primarily select events that go through the 5-mm base-to-apex thickness of the T scintillator. The mean number of photoelectrons deduced from this distribution is 5.09 ± 0.04.*

Allowing for the additional light attenuation expected from optical connectors and clear fiber runs when the SMD is assembled within the EEMC, we should still attain 2–3 p.e./MIP for final performance, to be compared with the 2.0 p.e./MIP assumed in the simulations shown in Figs. 33–36. This performance is furthermore very consistent with the 11.0 p.e./MIP actually attained in D0 with VLPC's, whose quantum efficiency is four times greater than that of the PMT's. Note that the Hamamatsu MAPMT to be used has the same quantum efficiency as the Burle tube used (because of its higher gain) for these bench tests on individual MIP's.

The tests of the prototype EEMC and SMD detector are essential to establish the veracity of the GEANT-based simulation of electromagnetic showers. Questions to be addressed in the in-beam test of the prototype include:

- Do the measured average transverse shower profiles agree with the simulations shown in Fig. 32?

- Are the measured shower-to-shower fluctuations in the transverse profile in agreement with simulations for incident photons and for incident π^0's?

- Does the measured light output from the strips scale with $\sqrt{E_\gamma}$? Can this scaling be used to provide an accurate *in situ* calibration of the full-scale SMD when it is mounted in the STAR detector?

In addition to providing crucial performance tests of the SMD, in-beam tests of the prototype will provide invaluable information about the EEMC tower response. Although answers to these questions would be ideally provided by measurements with higher-energy test beams, it is believed that what is learned with lower-energy photons and π^0's at Jefferson Laboratory will impose a sufficient constraint on the simulations discussed above.

7 EEMC Readout Electronics and Triggering

7.1 Overview

The EEMC comprises three detector subsystems: the calorimeter towers, SMD strips, and two layers of preshower. Although each of these detectors is based on plastic scintillator coupled via optical fiber to PMT's, significant differences exist in the front-end electronic (FEE) signal analysis, interface to DAQ, and generation of trigger primitives among the three subsystems. These are due to differing constraints, *e.g.*, on the quality required of the detector response, available signal processing time, and raw channel count.

For much of the spin physics program envisioned for STAR, it is essential that information from the EMC — the calorimeter towers in particular — be integrated into the Level-0 (L0) trigger. As will be shown below, it is also important that complete EMC data (towers plus SMD) be available for several consecutive RHIC beam crossings, which occur every 110 ns. For these reasons, the tower electronics must be capable of processing and digitizing (with sufficient resolution) PMT signals, and creating the needed trigger primitives, at rates of ∼9 MHz. The most critical element for the L0 triggering, which will be described in more detail in Sec. 7.4, is identification of the individual towers ("high towers") and contiguous clusters of towers ("patch sums") which contain particularly high energy deposition. In addition to forming parts of the L0 trigger, this information is also passed on to higher-level (and slower) STAR triggers (L1–L3), where it can be correlated not only with other EMC data, but with the other 'fast' STAR detectors, and eventually with the TPC and SVT tracking detectors. At the moment, we do not envision using either the endcap SMD or preshower information at Level 0; hence slower, but lower cost-per-channel, readout systems can be employed.

To implement the above, most of the readout and trigger electronics currently under development for the barrel EMC [38] can be taken over for use in the endcap with only minor modification. In some cases, changes are needed to accommodate use of alternative technology, such as our choice of an SMD consisting of scintillating strips rather than wire chambers, or are driven purely by the geometry of the disk-like endcap *vs.* the cylindrical barrel. Other changes are motivated by concerns that are unique to *pp* running, with implications for both the endcap *and* the barrel systems. After discussion with members of the barrel electronics group, it appears that in all cases the needed modifications can be made relatively inexpensively, and without extensive R & D effort. In the following subsections, we will concentrate on those aspects of the endcap electronics that differ from the schemes outlined in the barrel EMC Technical Design Report [38], and refer the reader to that document for more detailed descriptions of the many common features of the two systems. We also point out that all ancillary systems, such as PMT HV control, slow controls, and clock and trigger distribution, and the interfaces between these systems and the EEMC electronics, will be modeled closely after those to be used for the barrel, and will not be discussed further here.

7.2 Calorimeter Tower Readout

The electronics for the endcap EMC will reside partially on the STAR magnet and partially on the electronics platform. A schematic overview of all the electronics (DAQ plus triggering) associated with the calorimeter towers is presented in Fig. 43.

After collecting light from the 24 scintillating tiles within each tower, the PMT signals (one per tower) are sent to the tower digitizer cards, mounted in 9U VME crates located on the outside surface of the STAR magnet poletip. As in the barrel EMC, the EEMC digitizer cards will consist of a gated integrator and a 12-bit linear flash ADC for each input channel, with a linearity check
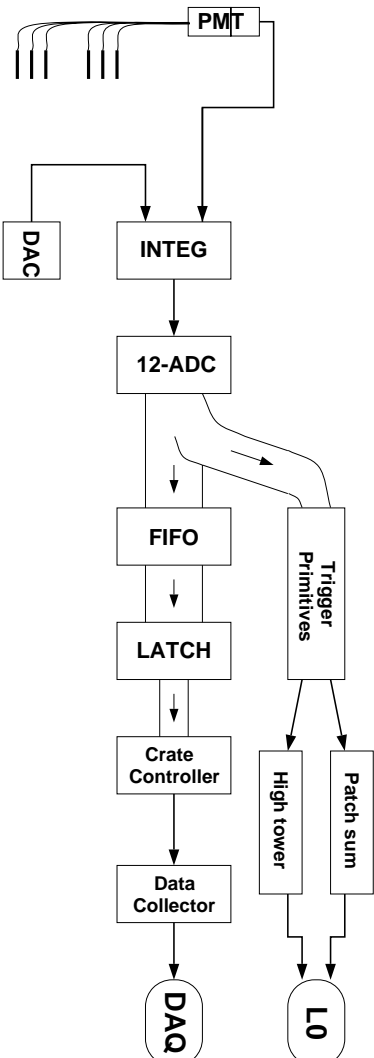
Figure 43: *Schematic overview of the electronics associated with the EEMC tower electronics.*

provided by a DAC-controlled charge injection system. The ADC output (digitized tower pulse-height information), produced for every RHIC beam crossing, is sent to a 64-word deep FIFO, which serves as a latency delay. Upon receipt of a valid trigger, the ADC output corresponding to the beam crossing of interest is strobed into a data latch; this is then read out over the VME backplane by the crate controller, then passed over optical fiber to the (common) EMC data collector on the platform. The full EMC data volume (barrel plus endcap) is then transferred to DAQ and to the Level 2 trigger for further processing. The path to Level-0 indicated in Fig. 43 will be discussed in Sec. 7.4.

With a capacity of five tower digitizer cards per VME crate, and 32 input channels per card, a minimum of 5 crates would be required to handle the 720 endcap towers. If space permits, a better match to the endcap tower modularity would be achieved by using 6 crates containing 4 cards each, in which case each crate would be associated with a particular 60° section. As will be discussed in Sec. 7.4 below, this would result in 15 tower patches (and thus generation of 30 trigger primitives) per crate.

Two aspects of the tower readout scheme perhaps warrant additional discussion. The selection of 12-bit ADC's was to ensure that the pulse height information from each tower would provide sufficient energy resolution for all processes of interest, with $e^\pm$'s from high-energy $W^\pm$ decay placing the most stringent demands on $\Delta E/E$. This will also allow us to span the needed dynamic range of ~1000:1 in energy deposition, extending from detection of individual minimum-ionizing particles (MIP's), useful for system calibration, up to the most energetic $W^\pm$ decay daughters ($E_W \approx 150$ GeV, corresponding to $p_T \approx 40$ GeV/c at the most forward angles), which would result in roughly 10 GeV being deposited in the scintillator layers of a single tower.

For the spin physics program, or any study involving high-luminosity pp running, it is also essential that the capability exist for readout of all EMC tower information for the beam crossings that occur immediately before and after the crossing of interest. With e^- drift velocities of ~5 cm/μs in the TPC, and a beam crossing period of 0.11 μs, the charged particle tracks from close to 20 consecutive crossings would all 'point back' to a 10-cm long interaction diamond. Thus, correlation of individual tracks with particular beam crossings *must* be accomplished by matching the TPC track into the EMC. At pp luminosities of $\mathcal{L}_{pp} \sim 2 \times 10^{32}$, however, one can expect on the order of one minimum bias event per crossing; events of interest will therefore generally be accompanied by additional tracks that exhibit the same timing, and also fire an appropriate EMC tower. Eliminating these additional tracks will rely on accurate traceback to the event origin.

While this can be done in principle, it is important that a sample of tracks correlated (via the EMC) with the *wrong* beam crossing also be available to test our subtraction schemes. These can not be selected randomly in time, but must point back to an origin within the interaction diamond, in order to properly test our track elimination procedures. Crossings that are adjacent in time to that containing the event of interest would be the most useful sample for these purposes.

In order to provide this capability, a field-programmable gate array (FPGA) will be used to generate the output timing strobe(s) for the FIFO in which the tower ADC data has been stored (see Fig. 43). This will allow for multiple strobing of the FIFO, with each strobe selecting out the ADC value associated with a particular beam crossing, each with a fixed time relation to the crossing of interest (*i.e.*, that which contained the trigger event). While this procedure will slightly increase the EMC data volume, it should have negligible effect on any subsystem deadtimes.

7.3 SMD and Preshower Readout

Despite obvious differences in scintillator shape and size between the SMD and preshower detectors, demands on the readout electronics needed for these two subsystems are quite comparable, and have led us to consider use of similar technologies. These are again modeled closely after readout schemes being developed for the barrel SMD; however, because the endcap SMD is based on scintillating strips rather than wire chambers, the initial stages of signal processing (amplification and shaping times) will differ somewhat from the barrel specifications. All subsequent electronics, though, can be identical. The two layers of preshower detector, which may not be instrumented for the barrel, are intermediate between the calorimeter towers and the SMD in both the stringency of their response requirements and in their channel count. Like the SMD, the preshower information is not required at Level 0, so slower and more cost-effective readout systems may be used.

A schematic layout of the SMD (and preshower) readout electronics is shown in Fig. 44. Signals from the 7200 SMD scintillating strips and the 1440 preshower tiles will be sent to 16-channel multi-anode photomultiplier tubes (MAPMT's), mounted on the STAR magnet poletip. Use of MAPMT's is feasible here, due to the less stringent requirements on energy resolution, linearity, and gain calibration for the SMD and preshower responses compared to those of the calorimeter towers. Because information from these detectors is not used in generation of the L0 trigger, it is not necessary (or economical) to digitize each input channel immediately; rather, analog signals can be shaped, then sampled and stored in a cycling switched capacitor array (SCA). Receipt of a valid Level 0 trigger halts this cycle, then initiates transfer of the stored data to a Read Out Module (RDO) for digitization and eventual transfer to DAQ. Multiple data words, *i.e.*, several consecutive time samples of the MAPMT signals, can be read out in this fashion.

The primary difference between this system and that used for the barrel SMD will be the parameters required in the preamplifier and shaper (SAS) chip mounted on the FEE board. In particular, the shaping times of 60–150 ns appropriate for the wire/gas strips used in the barrel must be shortened to the 30–50 ns range, which is quite reasonable for plastic scintillator (shorter times offer little advantage, given the period of the beam crossings). We are currently weighing the advantages of simply modifying the input parameters of the barrel SAS chip *vs.* adopting a pin-for-pin compatible chip designed for other purposes at LBL. For the endcap SCA array, we will use chips developed for the STAR SVT, which are 128 words deep and can operate at up to ~27 MHz, roughly three times the RHIC crossing frequency. In our application, it would be most efficient to sample and strobe the analog data into the SCA storage elements at exactly the RHIC crossing frequency, in which case readout of consecutive elements provides a clear 'snap-shot' of which strips fired (and their integrated light output) for each of several consecutive crossings.
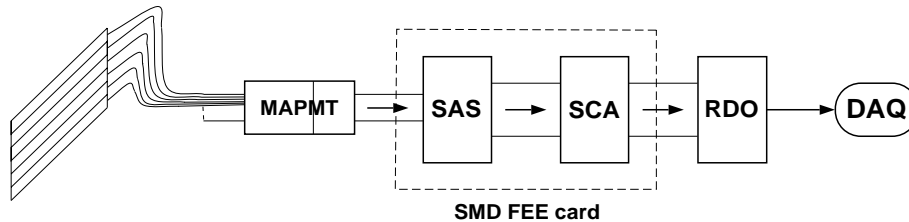
Figure 44: *Schematic layout of the endcap SMD and preshower electronics*

The motivation for this stems from the same argument presented at the end of the preceding subsection; for identification of background tracks, it is highly advantageous to be able to correlate unambiguously the firing of a given SMD strip or preshower tile with a particular beam crossing.

For both the SMD and preshower electronics, each FEE card will contain 20 SAS and SCA chips, with 16 inputs per chip. For the endcap SMD, each 30° sector, with a channel count of 600 strips (plus an additional 40 MAPMT channels needed for light pulser inputs), will require two FEE cards, for a total of 24 cards. This divides naturally into 12 cards for each of two RDO modules (somewhat less than the 15 cards per RDO planned for the barrel), or one RDO for each half of the endcap; thus, two VME crates mounted on the outer poletip surface will easily accommodate all of the SMD electronics. For the preshower layers, with 240 (plus 16 light pulser) input channels from each 60° section of the endcap, modularity suggests use of 6 FEE cards and a single (though under-utilized) RDO module. If space constraints turn out to be severe, it may be possible to combine all SMD and preshower on-magnet electronics into two VME crates.

All connections between the SCA output receivers/drivers and the RDO modules, and all subsequent electronics leading to transfer to DAQ, will use the same equipment and protocols as will be used for the barrel SMD.

7.4   EEMC Contributions to Trigger Logic

The endcap detector systems will enter into the STAR trigger logic primarily at two points: through generation of fast trigger primitives available at Level 0 (and all higher levels), based on calorimeter tower information; and through the full EMC data volume, available at Levels 2 and 3. The former path is illustrated schematically in Fig. 43.

For the pp spin physics program, the primary concern with regard to triggering is to quickly identify events in which a single tower contains the large energy deposition characteristic of a high-p_T electromagnetic shower, usually resulting from an incident direct photon, $e^{\pm}$ from $W^{\pm}$ decay, or leading π^0 from a jet. To identify jets, and, more importantly, to distinguish jets from γ's and e's, it is useful to also form sums of the energies contained in contiguous 'patches' of towers. For each patch, these two data words — the sum (most significant 6 bits) of the patch tower energies, and the highest single tower energy within the patch (also 6 bits) — will be produced on the tower digitizer cards, then sent on to the EMC Level 0 trigger hardware, at which point they can be compared to several preset thresholds or receive further processing (such as correlation tests) in data storage and manipulation (DSM) boards. The results of these tests are then passed to the main STAR L0 board for prescaling and final trigger decision.

This basic logic flow (excluding specific DSM analyses) is already incorporated into plans for the barrel electronics, and will be implemented for the endcap as well. However, one difference arises due to the substantially larger areas (in $\Delta\eta \times \Delta\phi$) subtended by the individual endcap towers
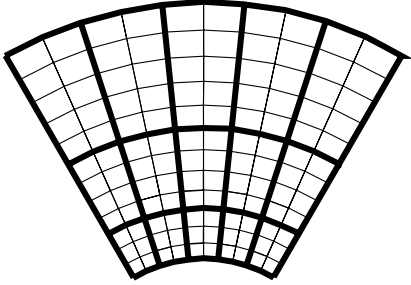
69

Figure 45: *Proposed grouping of the 120 calorime-
ter towers in a 60° section of the endcap into 15
'patches' for use in Level-0 triggering. Each patch
covers a comparable area in η and ϕ, despite the
large variations in (absolute) transverse size.*

compared to those of the barrel. These larger areas are necessary in order to keep each transverse
tower dimension greater than 8 cm (see Sec. 4.1). At the same time, one would like to maintain
patch sizes in the endcap that are roughly comparable to those used in the barrel (0.2×0.2 in
$\Delta\eta \times \Delta\phi$). This choice should provide more uniformity in trigger definitions (especially for jets)
between the endcap and barrel, keep the (raw) particle fluxes in all patches approximately equal,
and ensure that the patches are large enough to minimize leakage of single electromagnetic showers
into neighboring patches, but still considerably smaller than a typical jet profile. One possible way
of grouping the endcap towers into patches that satisfy these criteria is illustrated in Fig. 45 for
a 60° section of the endcap. In this scheme, one matches the ϕ boundaries of the barrel patches
exactly, and divides the detector into three approximately equal ranges in η ($\Delta\eta = 0.32$, 0.32,
and 0.29 as one moves inward), while keeping the patch arrangement sufficiently 'regular' that
unwanted η and ϕ dependences should not be introduced into the triggering. The patch scheme in
Fig. 45 would also allow testing of correlations between EEMC energy and MWC charged particle
multiplicity (*e.g.*, for triggering on jets) within common 60° sectors. It is unfortunately not possible
to match *both* the finer 30° segmentation of the MWC and the BEMC $\Delta\phi = 0.2$ trigger patches.

Figure 45 also makes it clear, though, that despite the somewhat larger patch sizes defined for
the endcap, there will be only 6–10 towers per patch, *vs.* 16 for the barrel. Each tower digitizer
card accepts 32 inputs; thus, the trigger portion of the electronics was designed assuming there
would be only two patches per card, whereas there will be four patches associated with each card
in the endcap. Each card, then, must be capable of generating twice as many trigger data words as
was originally envisioned, which will require some minor reprogramming of FPGA's, plus mounting
a few additional drivers and cable connections. Rather than producing a set of modified cards, we
are currently pursuing the integration of these changes into the 'standard' tower card design to be
used in both the endcap and the barrel EMC. The net result is the EEMC will produce 90 6-bit
high tower energies and 90 6-bit patch energy sums for the EMC L0 trigger.

For the events of primary interest here, *i.e.*, those involving direct photon or $W^{\pm}$ production,
extensive reduction of the L0 trigger rate through higher-level trigger processing may not be re-
quired, at least at the lower pp running energies ($\sqrt{s} = 200$ GeV). Detailed simulations suggest
that even at full luminosity, $\mathcal{L}_{pp} = 8 \times 10^{31}$, a high tower threshold of $p_T \geq 5$ GeV/c for the entire
EMC (endcap and barrel) would result in a trigger rate of only ~ 30 Hz. Thus, in early pp running,
one may be able to pass this trigger directly to Level 3 (see below).

At this stage, we are just beginning to investigate suitable trigger definitions for other processes,
such as identification of jets or di-jets. For these sorts of triggers, rates at L0 can be expected to be
very high, and significant reduction will be necessary. This can be accomplished either by 'blindly'
prescaling the L0 signal down to an acceptable level, or (preferably) by imposing conditions at
Levels 1, 2, and 3 to select out the most suitable candidate events. Though specific event selection

procedures have not yet been developed, we plan to examine possible correlations between energy deposition in a single tower *vs.* that in the surrounding set of towers (a more sophisticated 'patch' comparison), as well as correlations of the EMC data with that of other STAR 'fast' detectors, such as the CTB and MWC. These latter two detectors can provide charged-particle multiplicities over regions in (η, ϕ) that overlap very closely with the barrel and endcap EMC, respectively. Some initial efforts to simulate (in software) the effects of imposing such conditions in the trigger hardware are described in Sec. 3.4 of this report.

Whether such tests can be performed adequately at Level 0, or are more efficiently deferred to L1 or L2 trigger processing, is not yet clear. Regardless of the method used to achieve the needed rate reduction at these earlier levels, however, it is important to note that in *all* cases efficient data acquisition for high luminosity *pp* running will require substantial processing at Level 3 for track reconstruction, in order to remove tracks and track segments that point back to event origins far outside the interaction diamond. This is essential, in order to reduce the large *pp* data volume. While not strictly an electronics issue, this concern is relevant here, in that the extent to which the event data volume can be reduced will directly determine the allowed input rate to L3, and hence set the level of rate reduction required in the lower level triggering.

8 Calibration Issues

8.1 Summary of Calibration Requirements

The requirements for the performance of the endcap electromagnetic calorimeter (EEMC) towers, preshower layers and shower-maximum detector (SMD) have been discussed in Sec. 3 of this document. To clearly delineate what *in situ* calibrations of the EEMC are necessary, a brief synopsis of the calibration requirements is given below.

- An *online* calibration of the EEMC tower readout, accurate to within 20%, is required for individual towers, so that reliable triggering on direct photons and positrons and electrons ($e^{\pm}$) from $W^{\pm}$ decay can be achieved.

- The equivalent photon energy deduced from the EEMC towers must be known to an absolute accuracy of $\pm 2\%$ for photons with transverse momenta, $10 \leq p_T \leq 20$ GeV/c. This requirement is necessary to limit systematic errors in the determination of the integral ΔG. Accurate knowledge of the photon energy is required for the reconstruction of the initial-state partonic kinematics.

- The linearity of the EEMC tower calibration must be known to better than $\pm 5\%$ for $e^{\pm}$ and photons with energies up to 150 GeV, for $\vec{p}+\vec{p}$ experiments at $\sqrt{s} = 500$ GeV. It is measurements at the latter energy that impose the strictest requirements on the high energy calibration, for two reasons: to enable a measurement of $\Delta G(x)$ at large x_{gluon} values, that overlap measurements taken at $\sqrt{s} = 200$ GeV; and to enable reliable detection of $e^{\pm}$ arising from the decay of $W^{\pm}$, and the kinematic reconstruction of the initial state partons that produce the W.

- The additional data needed to perform *in situ* calibrations of the EEMC towers to the required accuracy must be obtained within the same 10-week running period used for the production run at each beam energy. This will enable a timely analysis of the data.

- The relative gains of the SMD scintillator strip readout must be measured to within 30%, assuming *random variation* of the readout gain from strip to strip. It is necessary to ensure that *systematic* differences between the readout gains of *adjacent* SMD strips be kept under 10%. This requirement is imposed by the SMD 'shower-shape' analysis algorithm, used to discriminate single photons from photon pairs arising from the decay of $\pi^0(\eta^0)$ mesons.

- The probability that photons, arising from the decay of π^0 or η^0 mesons, convert into e^+e^- pairs upstream of the first scintillator layer of the EEMC (preshower detector) must be measured as a function of the neutral meson energy to an accuracy of 15%. These measurements are necessary to constrain simulations of the preshower detector performance, to enable statistical subtractions of the π^0 contamination of the prompt photon sample at $p_T \geq 20$ GeV/c.

- The relative geometry between the SMD strips and the boundaries separating EEMC towers must be accurately known. This requirement is needed to use the SMD position information to establish if an EEMC shower is significantly shared between adjacent towers, or if the adjacent towers are responding to a pair of incident particles.

- The relative positioning of the EEMC with respect to the STAR tracking detectors must be determined. This is essential to make use of a space point, obtained from the SMD, in the

tracking of the highest p_T electrons and positrons from $W^{\pm}$ decay, to aid in the discrimination of the sign of the particle's electric charge.

The accurate calibration of the readout of the 720 towers of the EEMC, 1440 preshower scintillators and the 7,200 scintillating strips is a daunting, but achievable, task. It is anticipated that a significant part of the data analysis effort will be devoted to meeting the requirements stated above.

8.2 In Situ Calibration Techniques

Multiple techniques will be needed to perform *in situ* calibrations of the EEMC towers. Immediately prior to each 10-week production run, an on-line calibration of the response of the detector to minimum ionizing particles (MIP) can be used to initially set the gains for the tower readout system. The other methods discussed below can be employed in off-line analyses to establish the calibration over the full energy range. To summarize, the calibration techniques needed for the determination of the integral ΔG include:

- use of energetic charged hadrons, providing energy deposition within the EEMC detectors equivalent to that of minimum ionizing particles;

- use of photons arising from the decay of low-energy $\pi^0(\eta^0)$ mesons, with the two photons in separate EEMC towers;

- use of energetic π^0, arising from the decay of $\rho^{\pm}$ mesons, with coincident detection of the daughter $\pi^{\pm}$ mesons.

As discussed below, additional techniques are required to extend the calibrations to higher energies than required for the integral ΔG measurement, relevant for experiments performed at $\sqrt{s} = 500$ GeV.

8.2.1 Calibrations using minimum ionizing particles

The low energy response of the EEMC towers can be accurately measured using penetrating charged hadrons which, most of the time, deposit energy in the tower scintillators consistent with a minimum ionizing particle (MIP). A momentum determination from the TPC track reconstruction will be more than adequate for selecting sufficiently energetic charged particles, to ensure the likelihood of a MIP response from the EEMC. On average, a MIP will deposit $\sim$ 22 MeV in the EEMC tower scintillators. This energy deposition is equivalent to the sampling of a shower produced by a photon of energy $\sim$ 360 MeV. Due to the variation in the angle of incidence across the EEMC, the centroid of the MIP peak in the tower pulse height distribution varies by 23%. The background under the MIP peak due to charged-hadron-induced showers is simulated to be $\sim$15%. This is small enough to provide a reliable determination of the centroid. The tower photomultiplier gains can be initially set from a small sample of data.

In addition to calibrating the EEMC towers, penetrating charged hadrons can also provide calibration of the relative gains of individual scintillator-strip readout channels for the SMD detector. To ensure that the charged hadron traverses the wide part of the strip (apex to base), it is necessary to require non-zero pulse height in only a single strip of each SMD plane (u and v). Due to the small light output (expected to be 2-3 photoelectrons for each MIP crossing the wide part of the strip) the accuracy of using *only* penetrating charged hadrons to calibrate the SMD will be limited.

The rate of energetic charged hadrons intercepting the EEMC is likely to be large enough to serve as a *continuous monitor* of the calibrations of the tower, SMD strip and preshower readouts. Given sufficient dynamic range of the tower ADC (12 bits), a MIP signal should be readily observed.

Energetic charged hadrons are likely to provide the best method of establishing the relative geometry of the SMD to the EEMC towers, and to determine the geometric relationship between the EEMC and the STAR tracking detectors. Due to the limited reproducibility of positioning the poletip, geometrical calibrations will be required after every poletip removal.

8.2.2 Calibrations using photons from $\pi^0(\eta^0)$ decay

At sufficiently low energies, the two photons from $\pi^0(\eta^0)$ decay will deposit their energy in two separate towers of the EEMC. For this to happen with high probability, the minimum opening angle between the two photons must be comparable to the tower extent; hence, the $\pi^0(\eta^0)$ must have relatively low energy. Fortunately, the p_T distribution of $\pi^0(\eta^0)$ mesons is given by a power law falloff with increasing p_T, implying that very large yields of low-energy neutral mesons are available for calibrations. The signature for these events are two towers of the EMC, each with the deposited energy summed over the sampling layers in excess of $\sim$25 MeV, corresponding to an incident photon energy of 380 MeV, or greater. By demanding energy deposition beyond that generated by a MIP, a substantial portion of the combinatorics background in searching for low energy π^0 can be reduced. An invariant mass reconstruction can be applied to the candidate photon pair, to ensure they arise from π^0 or η^0 decay. An important crosscheck of the tower readout calibration obtained from penetrating charged hadrons, will be the correct reproduction of the $\pi^0(\eta^0)$ invariant mass.

Such di-photon events can supplement information about the low-energy calibrations of the SMD strips, initially provided from the MIP response. Events will be selected where the energy deposition is predominantly within a single strip (at least twice as much pulse height as neighboring strips) within a cluster on a given SMD plane(u or v). This assumes that the readout channels for neighboring strips have had their relative gain determined to better than a factor of two from the MIP calibration. The single strip response, averaged over many events, can then be compared to the measured energy in the towers. The expected $\sqrt{E_\gamma}$ variation of the energy deposition in the SMD can then be used to calibrate the gain of individual SMD strip readouts.

8.2.3 Calibrations using energetic π^0 from $\rho^\pm$ decay

Another calibration method relies on detecting *energetic π^0* mesons, arising from the decay of $\rho^\pm \to \pi^\pm\pi^0$, for events where the $\pi^\pm$ meson is also tracked by the TPC. This calibration technique was used by the CDF group in their measurement of direct photon production cross sections [34]. To calibrate the STAR EEMC, it is important that the neutral pion energy be sufficiently high, so that *both photons* arising from the π^0 decay are in a single EEMC tower. For the EEMC towers at small pseudorapidity, this requirement can be met for $E_{\pi^0} \geq 3.0$ GeV. A distinct advantage of this calibration method, is that $\rho^\pm \to \pi^\pm\pi^0$ events are a prolific background within the 'direct photon' trigger sample, with the definition of the trigger described in Sec. 7. Furthermore, the majority of the $\pi^\pm$ arising from $\rho^\pm$ decay (with an energetic π^0 detected in the EEMC) have a small p_T (≤ 2 GeV/c), which can be very well determined by TPC tracking.

The p_T distribution of energetic π^0, for events with $\pi^\pm$ mesons detected in coincidence, arising from $\rho^\pm$ decay is shown in Fig. 46. By restricting the charged pion to be within a narrow cone around the π^0 candidate, the combinatorics background associated with correlating the π^0 with the correct charged particle track can be greatly reduced. The mean charged particle multiplicity in a cone of half angle 0.5 about the π^0 is 2. Imposing this restrictive condition on valid $\pi^0\pi^\pm$
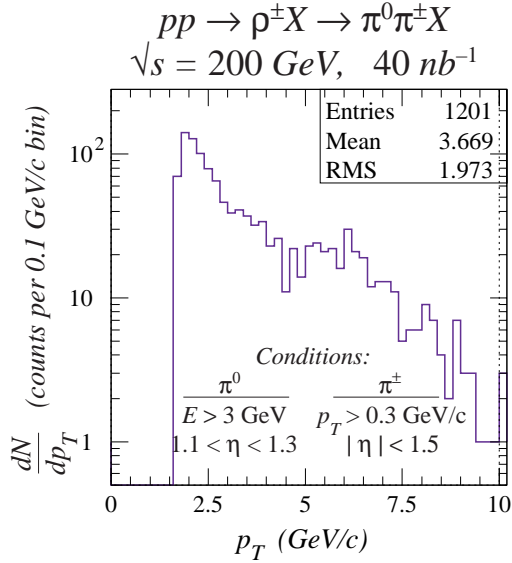
$pp \rightarrow \rho^{\pm}X \rightarrow \pi^0\pi^{\pm}X$
$\sqrt{s} = 200\ GeV,\quad 40\ nb^{-1}$

Entries	1201
Mean	3.669
RMS	1.973

Conditions:

π^0	$\pi^{\pm}$
$E > 3$ GeV	$p_T > 0.3$ GeV/c
$1.1 < \eta < 1.3$	$|\eta| < 1.5$

Figure 46: *The simulated p_T distribution of π^0 mesons arising from $\rho^{\pm}$ decay. The π^0 have energies greater than 3 GeV, so that the two decay photons will most probably fall within the same EEMC tower. The $\pi^{\pm}$ from the $\rho^{\pm}$ decay is detected by the TPC.*

coincidences will reduce the statistics by roughly a factor of two, compared to what is shown in Fig. 46, but should improve the overall statistical significance of the sample by reducing the combinatorics background.

From the distribution in Fig. 46, it can be deduced that, for the full 'direct photon' trigger sample at $\sqrt{s}$=200 GeV (320 pb^{-1}), there will be $\sim$1000 π^0 events (reduced to $\sim$500 events, with the more restrictive $\pi^0\pi^{\pm}$ opening angle condition described above) in *each tower* of the EEMC (assuming a constant value of $dN/d\eta$), in a 0.1 GeV/c p_T bin centered at 6 GeV/c. Reconstruction of the correct mass of the $\rho^{\pm}$ will be a powerful constraint on the calibration of the EEMC towers, spanning a substantial portion of the full energy range needed for the determination of the integral ΔG, for most of the EEMC towers. Due to the rapidly falling $dN/d\eta$ distribution for π^0 mesons coming from $\rho^{\pm}$ decay for $\eta \gtrsim 1.7$, the calibration of the readout of the EEMC towers at very large η may require special techniques, beyond those described above, to span a sufficiently broad range in p_T.

The coincident detection of $\pi^{\pm}\pi^0$ pairs, from the decay of energetic $\rho^{\pm}$ mesons, provides important calibration information, as well, for both the preshower detector and the SMD. For the former, the conversion probability of photons, arising from π^0 decay, upstream of the first scintillator layer (preshower) can be measured for neutral pions having transverse momentum in the range, $3 \leq p_T \leq 15$ GeV/c. The main purpose of this measurement is to determine the complex distribution of material between the interaction point and the EEMC. Once the upstream material distribution is known, a reliable simulation of the preshower response for $p_T \geq 20$ GeV/c can be used to normalize the statistical subtraction of neutral meson background from the direct photon sample at high energies, where the SMD discrimination is limited.

The event sample of π^0's arising from $\rho^{\pm}$ decay will also provide a crucial *in situ* test of the performance of the $\gamma/\pi^0(\eta^0)$ discrimination algorithm, based on the SMD information. In particular, the meson SMD survival probability (P_m), discussed in Sec. 3.2, can be determined from this sample.

75

8.2.4 Higher Energy Calibrations

For experiments at $\sqrt{s}$=500 GeV, it will be necessary to establish the linearity of the EEMC tower calibration to much higher energy, to enable accurate determination of the energies of photons and $e^{\pm}$ having $p_T \geq 20$ GeV/c. The details of how to establish the calibration linearity at higher energies are currently being pursued. In short, the possible methods include:

- observation of the J/ψ via its decay into e^+e^-. The extraction of a reliable signal may require a specialized trigger separate from that used for 'direct photon' detection.

- observation of a single, high-p_T electron or positron from the decay of a heavy quark (charm and bottom). To use this as a calibration tool, it is necessary to independently determine the $e^{\pm}$ momentum from TPC measurements. As well, discrimination between showers in the EEMC produced by $e^{\pm}$ from those produced by energetic charged hadrons will be needed. Finally, the TPC momentum resolution rapidly deteriorates for $\mid \eta \mid \geq 1$, meaning that single electron detection can, at most, be useful for only a portion of the EEMC.

- observation of coincident e^+e^- pairs from the decay of the Z^0.

Simulations are in progress to establish the efficacy of the above methods for establishing the needed checks of the linearity of the EEMC tower calibration.

8.3 Auxiliary Calibrations

The final primary absolute calibrations of the EEMC response will be based on data taken with the detector, when mounted within STAR at RHIC, as described in the preceding subsection. However, these measurements must be supplemented by others, not performed with beam from RHIC, to provide the needed pre-calibrations for initial (coarse) gain adjustment, continuous monitoring of gain stability, and diagnostic tests on components suspected to have deteriorated. These functions will be served by a combination of cosmic rays, radioactive sources, light pulsers, special calibration PMT's and test beams.

Cosmic rays will be used to test the tower, preshower and SMD response to MIP's both during assembly of the EEMC at IUCF, and in place at RHIC, prior to running periods. During assembly, we will furthermore have access, from the outer circumference, to holes in the plastic fiber guides, which allow insertion of radioactive sources at selected points within the EEMC volume. Pre-calibration can be further aided by exposing small prototype sections of the EEMC to test beams at Jefferson Lab (e.g., see Sec. 6.4), the AGS, or other laboratories.

The relative gain of each PMT in the system will be monitored continuously during use with light pulsers. The performance of any individual suspect tile-fiber combination can be checked by switching the fiber inputs from the corresponding megatile to a separate high-gain PMT mounted in the same box (see Sec. 5.2 for details). The relative gain of this extra PMT will also be monitored continuously with the same light-pulsing system. This optical diagnostic system will thus be important to ensure the stability of the absolute calibrations provided by the other means summarized in Sec. 8.2.

9 Integration in STAR
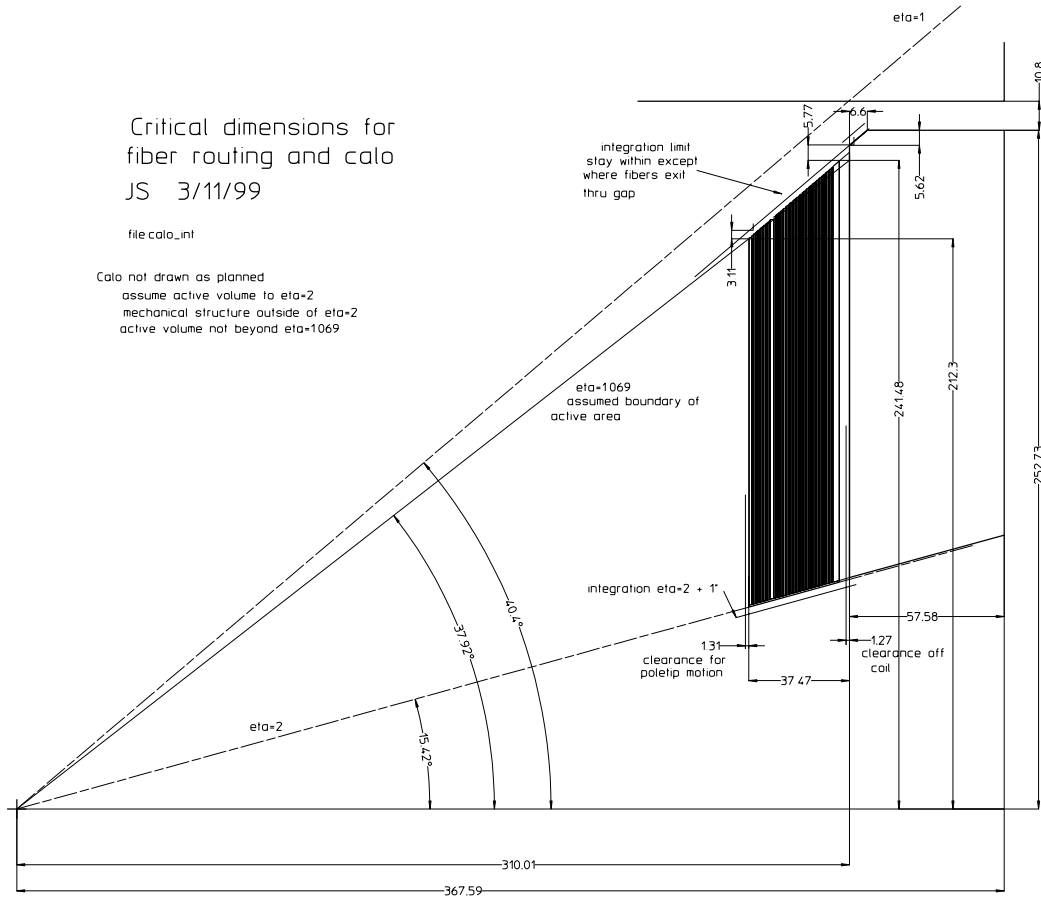
9.1 Space Constraints

Figure 47: *Illustration of relevant integration volume constraints superimposed on the proposed EEMC design. Dimensions are in cm.*

The EEMC must fit within the predefined integration volume indicated in Fig. 1. The relevant dimensions from the EMC Interface Definition - West (SIM160-A-1) have been collected on a drawing of the proposed calorimeter in Fig. 47. The allowed depth, 37.465 cm, begins at the inner surface of the poletip. A 1.3 cm clearance volume must be maintained in front of the EEMC to allow for a "rocking" motion during insertion of the poletip. (Note that current integration drawings still show this 1.3 cm between the pole tip and the EEMC. STAR has agreed to move this clearance to the front of the EEMC, but the drawings have not caught up.) The depth limitation is the primary constraint on the thickness of the calorimeter. The current design, with 21 mm allowed for the shower maximum detector, has a total thickness of 34.36 cm, including the back plate. This leaves 3.11 cm for stiffening and mounting the back plate to the poletip and for distributing among other components. We are currently considering adding 1 mm to the height of each SMD scintillator strip. There is also the possibility that we might make the first 5 scintillator planes

into preshowers, requiring an additional 3 mm. The amount of room needed for stiffening the back plate is yet to be determined from FEA calculations.
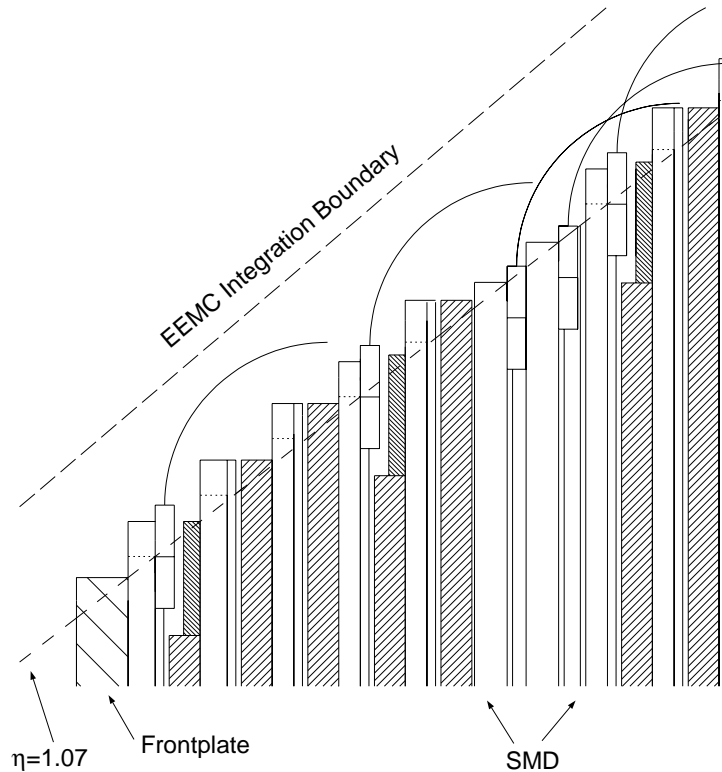

Figure 48: *Details of the integration volume near $\eta=1$ and the first 7 layers of the EEMC. The active volume begins at $\eta=1.07$, so that the integration boundary allows 3-5 cm (depending on depth) for routing of optical fibers, as illustrated schematically in the drawing.*

The outer diameter of the EEMC is limited by an integration line parallel to $\eta=1$ but translated by 12.7 cm toward smaller angles. Our present design of the EEMC leaves the outer 3-5 cm near this line for fiber routing, so that the the EEMC active region begins at $\eta=1.07$. Figure 48 shows schematically how optical fibers will depart toward the poletip from their respective megatile and SMD layers. It appears there is sufficient room (as discussed further below), but we are continuing to investigate the fiber routing questions in detail with 3-dimensional models. (Note that most available integration drawings show the TPC supports violating our integration volume. These supports have now been constructed to respect the EEMC integration volume, so this issue is no longer a concern.)

The integration volume is also limited at $\eta=2$ and our design reflects this. An additional 2.5 cm beyond $\eta=2$ was assigned to the EEMC for routing cables and fibers. Since the inner radius of the EEMC is used in our design as a primary structural support, we envision using most of this 2.5 cm

78

for the wall thickness of the inner conical hub (see Fig. 21). The proposed fiber-routing schemes currently call for all fibers to be routed toward the outer circumference of the EEMC, where they will be mated to fibers to the PMT's. We are maintaining some allowance just beyond η=2 for space to rout a small fraction of the SMD fibers, which would exit at the inner circumference and then bend around toward η=1, in one of the routing scenarios still under consideration. Even in this scheme, however, the active detector volume will extend all the way to η=2.
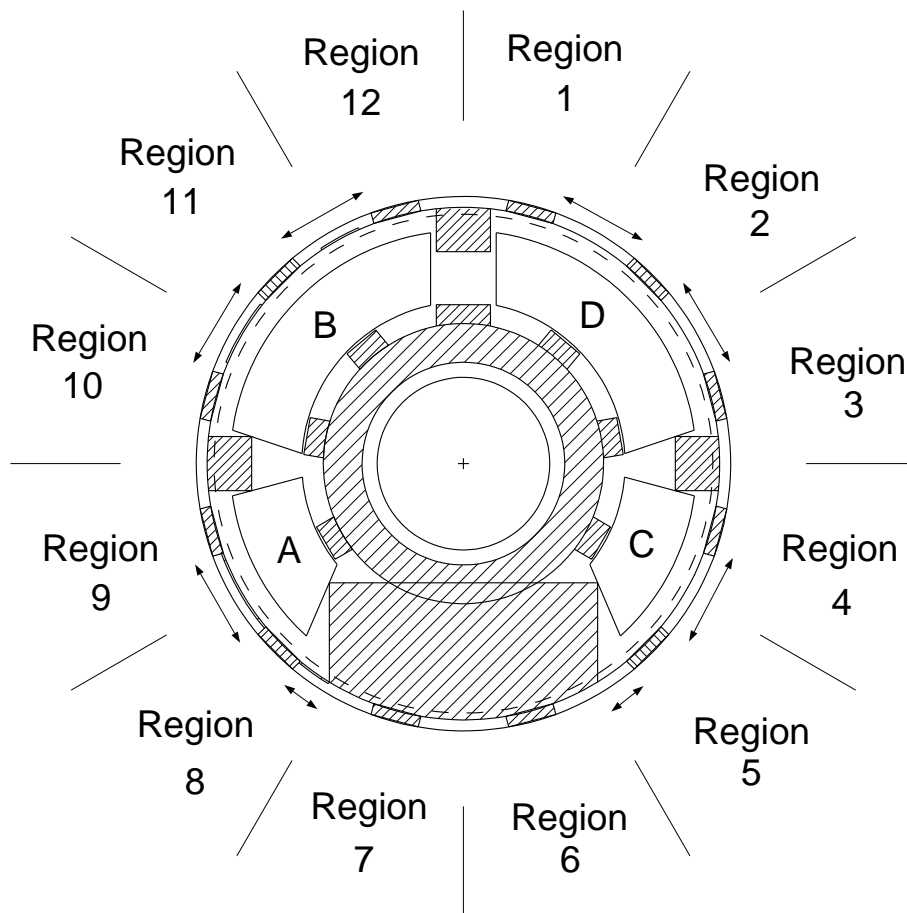

Figure 49: *View of the outside poletip surface. Areas ruled out by integration are shaded. The outermost annulus is the services gap. Regions where cable trays have been installed are also shaded. Unoccupied regions of the services gap available for EEMC fiber cable routing are indicated by arrows around the circumference. Four boxes are shown to estimate the area available for mounting PMT boxes on the poletip surface.*

There is space allocated on the back of the poletip for EEMC electronics, as shown in Fig. 1 and Fig. 49. This integration volume extends 25 cm beyond the poletip surface. In Fig. 49, we show four boxes mounted on the back of the magnet poletip, intended to house the PMT's. These would be just under 25 cm high. Preliminary designs indicate that a PMT with base should be about 4 cm diameter by 19 cm length. A similar size will be needed also for the MAPMT's (of 3 cm square cross section) projected for use for the SMD and preshower. We estimate the needed space by assuming two mounting scenarios. In one, the tubes are all mounted perpendicular to the face of the poletip.

In this case a 5 cm by 5 cm square is a generous estimate for each tube. The second estimate is based on tubes oriented parallel to the face, where they could be stacked four deep and take up an area 5 cm. by 25 cm. In Table 1 we show the number of tubes that could be accommodated in the boxes as drawn under these two scenarios, along with the number of PMT's needed in each box for the tower and SMD sector assignments presented in the table. These assignments are consistent with fiber routing, as well as with minimizing the length of fiber runs, within other constraints. Clearly, there is sufficient room for the PMT's and bases in the envisioned boxes, although some reassignment would be needed in the parallel mounting arrangement. Furthermore, there is adequate space available for the boxes to remain in place during roll-out of the STAR detector from the RHIC ring.

Table 1. PMT Assignments to Light-Tight Boxes Shown in Fig. 49.

Box	Capacity ⊥	Capacity ∥	Tower Region	SMD Region	Total Tubes
A	345	230	7, 8 & 9	7 & 8	284
B	706	480	10, 11 & 12	9, 10, 11 & 12	364
C	345	230	4, 5 & 6	5 & 6	284
D	706	480	1, 2 & 3	1, 2, 3 & 4	364

In addition to the PMT boxes, VME crates will need to be mounted on the poletip. These must be within 20 ft of the PMT's in order to prevent significant signal degradation. Based on current designs of the barrel cards that will be adapted for EEMC use, we estimate that 8 9U VME crates are needed for the EEMC electronics. No dimension of such crates is less than the 25 cm total integration distance allotted outside the poletip surface. Therefore, these crates will need to be removed when the STAR detector is moved between the two halls. We propose mounting these crates on a platform placed over the services for the poletip correction coil. In some envisioned cases, the poletips will be removed and left in the wide angle experimental hall when the STAR detector is rolled out into the assembly hall. At these times, only services would need to be disconnected to move the detector. When the poletips are needed in the assembly hall, the EEMC VME crates would have to be completely disconnected before transport of the detector

As mentioned above, the optical fibers will all be brought out at the outer radius of the detector and then run through the $\eta=1$ services gap to the back of the poletip. They will be enclosed in a cable tray for protection as well as aid in organizing the routing. There are a total of 18,720 tower and preshower fibers, and 7200 SMD fibers to be routed out of the detector to the phototubes. Using multi-fiber ribbon cable seems to give the most efficient packing of the fibers. We estimate that we can get 96 fibers to pass through an area 1.5 cm by 2 cm. Dividing the total number of fibers by 12 30° sectors, we find that a space 24.4 cm by 2 cm is needed for the tower plus preshower fibers from each sector, and an additional 9.4 cm by 2 cm is needed for SMD fibers. (An alternative to flat cable being used in the BEMC is 1/4" tubing for each 12-fiber bundle. The estimated space needed for this option is only 10% larger than the numbers presented here.) Figure 49 shows the annular gaps allowed for EEMC fiber routing, with cross-hatching indicating the areas already taken up by cable trays. The gaps at 12, 3, 6, and 9 o'clock have brackets holding the poletip to the rest of the magnet, leaving little clearance for fibers. Avoiding the poletip lifting fixture leaves a reduced gap at 5 and 7 o'clock. We propose using a region within 2-4 cm of the

surface of the poletip in the gap for each of the regions at 1, 2, 4, 5, 7, 8, 10, and 11 o'clock to run our fibers. Table 2 shows how the space will be used for the fibers and what fraction of the possible gap space is used. On average 14% of the available (remaining) volume in these gaps is used for the fibers. Note that further consideration needs to be given to the fiber-routing details in light of the projected 15° rotation of the physical EEMC sectors with respect to the logical regions denoted in Fig. 49. Nevertheless, there is clearly sufficient room remaining for fiber routing to allow considerable flexibility. For all poletip moving scenarios, the EEMC and the PMT's remain mounted on the poletip, so that no fibers need to be disconnected.

Table 2. Layout of envisioned fiber runs at the $\eta = 1$ gap.

Gap	Width	Tower Region	SMD Region	Space Used	% Width	% Volume
7 o'clock	35.2 cm	7	7	18 cm × 4 cm	53%	21%
8 o'clock	83.9 cm	8 & 9	8 & 9	68 cm × 2 cm	80%	16%
10 o'clock	83.9 cm	10 & 11	10	57 cm × 2 cm	67%	13%
11 o'clock	83.9 cm	12	11 & 12	43 cm × 2 cm	50%	10%
5 o'clock	35.2 cm	6	6	18 cm × 4 cm	53%	21%
4 o'clock	83.9 cm	4 & 5	4 & 5	68 cm × 2 cm	80%	16%
2 o'clock	83.9 cm	2 & 3	3	57 cm × 2 cm	67%	13%
1 o'clock	83.9 cm	1	1 & 2	43 cm × 2 cm	50%	10%
						14% avg.

9.2 Magnetic Field Concerns

An important concern is the magnitude of the magnetic field in the region where the PMT's will be mounted. The field in this region was measured to be as large as 500–2000 G near the gap between the pole tip and outer ring of the STAR magnet, but dropping off toward smaller radii as shown in Fig. 50. These strong fields necessitate housing the PMT's in steel boxes and individually wrapping them in mu-metal to provide adequate magnetic shielding. However, it is critical that addition of these external boxes does not significantly distort the solenoidal field within the TPC tracking volume. Initial magnetic field calculations have been done to understand the amount of shielding needed for the photomultiplier tubes and to investigate the effect of shielding on the internal fields.

As shown in Fig. 49, the PMT boxes are planned to be sections of an annulus with an outer radius of ∼220 cm, chosen to avoid the strongest fields near the gap. A model of the STAR magnet was created and a model of the PMT boxes was placed on the outside surface of the poletip, as shown in Fig. 51. In this figure the PMT box material is defined to be air. This calculation agrees fairly well with Poisson calculations done by the STAR magnet group. (More work needs to be done to get the magnet steel properties in the calculation to match the measurements better.) The PMT box model allows for 3 channels at the outer radius and one at the inner radius where photomultiplier tube assemblies can be placed. The bulk of the box is a solid volume to limit the number of necessary space points. This model can be used to investigate the necessary thickness of the plates separating the phototubes as well as the effects on the internal fields. A calculation with the box material set to steel, including the massive central part of the box, is shown in Fig. 52. It appears that the first box wall may need to be as thick as 3/8", and the next few as much as 1/4", to shield the PMT regions sufficiently so that mu-metal will not be saturated. (Further calculations
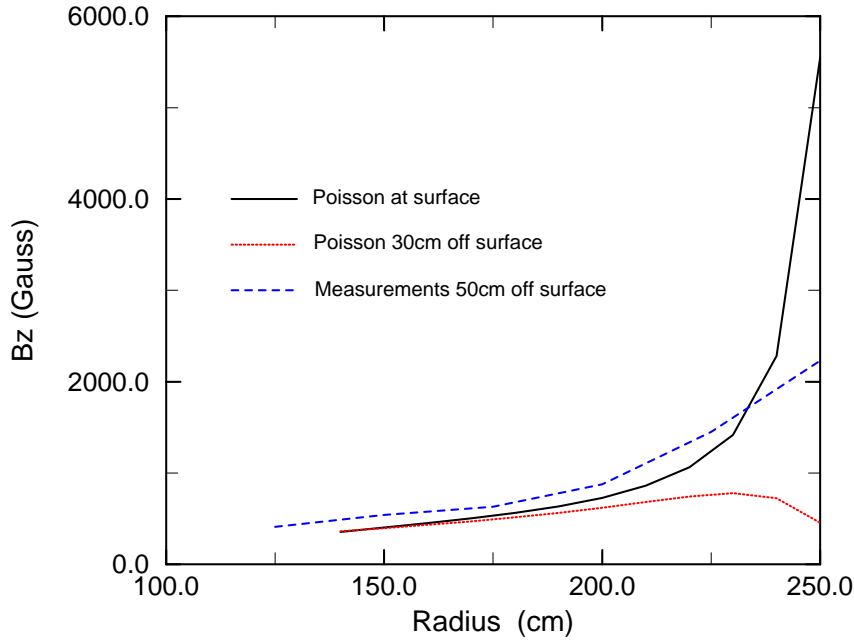
Figure 50: *Measurement of magnetic fields on the back of the poletip in the region where the PMT boxes will be placed, compared to Poisson calculations by the STAR magnet group.*

will be performed to optimize the amounts of mu-metal and regular steel.) The walls will then get progressively thinner as they move toward the inner radius of the box.

The change in the internal field from this model is relatively small and significantly overestimated. As can be seen in Fig. 52 field lines from the poletip are pulled up into the solid steel center of the modeled box, reducing the magnetic resistance of the magnet. This would not happen with the true configuration of walls separated by air gaps. The field on axis increases by a uniform ∼3 G out of 5000 G out to the end of the TPC. As the field change is followed out in radius at the end of the TPC, the increase varies from 3-6 G. The true requirement is that the integral of the radial component of the magnetic field along the drift path in the TPC not exceed a value corresponding to an average of 17 G over the path. The simplified PMT box model used in the calculation for Fig. 52 would then be only marginally acceptable. However since the real box will not be solid steel, we expect that changes of field inside the magnet will be considerably smaller than calculated, and therefore not a problem. Nevertheless, more realistic and detailed calculations will be pursued and followed to conclusion.

9.3   Electronics Integration

The EEMC increases the number of signals, over those associated with the barrel, that must be handled in the trigger and DAQ electronics, but at a quite manageable level. The EEMC has been in STAR's plans all along and, for example, sufficient rack space on the electronics platform is already allocated, as well as capacity for the additional signals into DAQ. The interfaces and
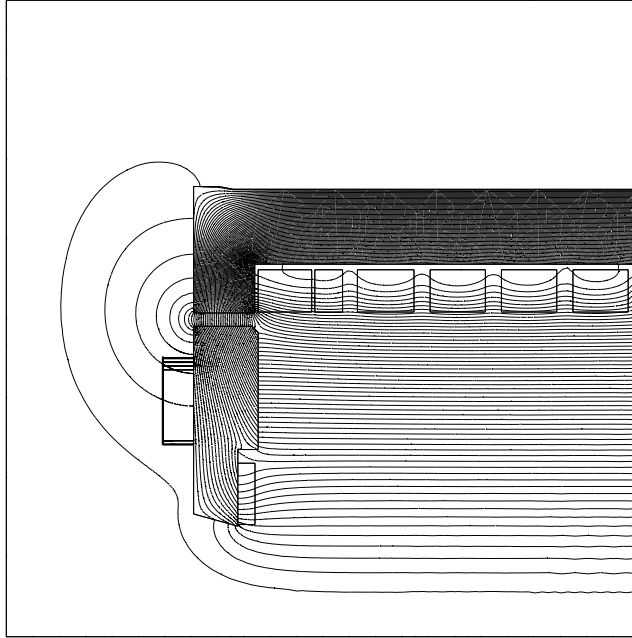
Figure 51: *Baseline calculation of the STAR magnetic fields. A PMT box is placed on the back of the poletip but the material is defined to be air for this calculation. The central field is 5000G.*

data protocols into DAQ, such as data formats, hand shaking and fiber links, are long established and already followed in the the electronics boards we will be adapting to use in the EEMC. Star standards and protocols into the trigger are also followed and simplified by adapting existing designs from other systems, primarily the BEMC. Control and monitoring of the detector is to be handled by STAR standard slow controls through online software interfaces, and again much of this is to be duplicated from the BEMC. Offline software for databases on pedestals and calibrations must be supplied. In addition, algorithms for determining tower energies and SMD shower fitting must be supplied. Finally, no large power or cooling demands will be made on the infrastructure in the STAR hall by the EEMC.

More significant issues are raised by p-p collisions at high luminosity. These issues have already affected the design of the DAQ and trigger systems in STAR in preparation for the demands of the spin physics program. For heavy ion physics, triggers will be generated at ~ 1 Hz. Au-Au events will be very large with track multiplicities in the 1000's. A typical event is expected to be between 10 and 20Mb in size, and all the information must be saved to tape. On the other hand p-p trigger
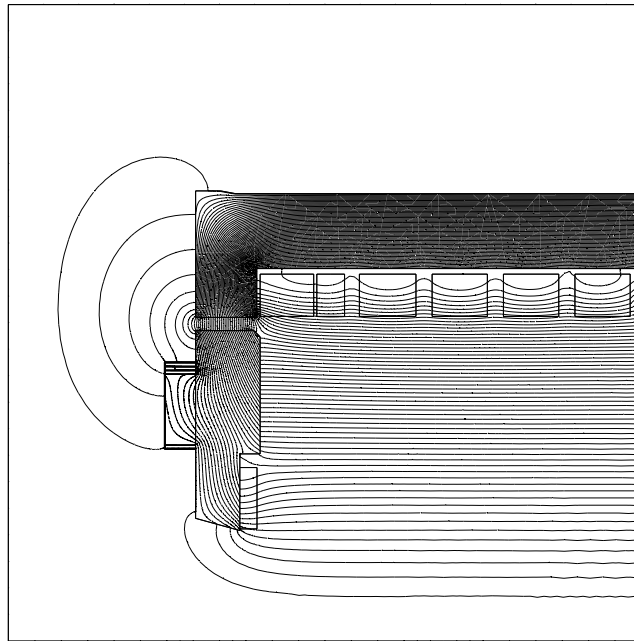
Figure 52: *The magnetic field with a steel box on the back of the poletip. The center of the box is a solid piece of steel to limit the number of space points in the calculation. At the inner and outer edge of the box magnetically shielded channels are created with walls made of steel sheet. A true box will of course have similar channeled construction throughout. Thus the effects on the internal field of this model are significantly overestimated.*

rates will be 10's of Hz, with typical particle multiplicities less than 100. The complication in p-p is the high luminosity. At the highest energy $\sqrt{s}$=500 GeV, the luminosity is 2×10^{32}cm^{-2}s^{-1}, resulting in a minimum bias rate $\approx$ 10 MHz (1/2 to 1/3 of this at 200 GeV), or one almost every beam crossing. The drift time in the TPC is 40 μs, so that one can expect over a thousand pileup track segments in an event (2-3 charged particle tracks per minimum bias event), most of them uninteresting but adding to the data volume. Since the largest data volume comes from the TPC, a single p-p event with TPC pileup will be similar in size to single central Au-Au events, but we must maintain a higher trigger rate. This large volume of data presents a problem for transmittal to the computing facility for archiving. The level 3 trigger (a multi-cpu device) is being designed to identify and parameterize tracks in the TPC, to facilitate elimination of some of the pileup tracks, and compression of the information for the rest, before data is written to tape. Important to this algorithm is correlation with the information from both the barrel and endcap EMC. In order to assess the efficiency of this algorithm, and also the level of contamination remaining after application of offline pileup rejection software, DAQ will be required to read out all EMC information for one beam crossing immediately preceding, and one immediately following, each trigger event, as well as the information from the proper crossing. The level 3 trigger architecture is strongly influenced by the need to transmit compressed TPC information for those tracks that survive level 3.

The spin program also places unique demands on the hardware scalers implemented as part of the trigger. This comes from the need to keep track of the luminosity separately for each spin combination among colliding beam bunches, resulting in a large number of conditions under which to scale quantities. Furthermore, these relative luminosities must be determined far more precisely for the spin program (in order to avoid instrumental asymmetries comparable to the expected physics asymmetries discussed in Sec. 2) than for the heavy-ion collision program. The development of reliable luminosity monitors, undistorted by their own spin-dependence, at these unprecedented polarized collision energies, will require scaling a variety of potential signals simultaneously, so that one can compare them at the required precision level ($\leq 10^{-3}$). In conclusion, the interfacing of spin and the high luminosity of the p-p program have placed significant integration demands back on the STAR systems. These requirements have been designed and planned for, and many are currently being implemented, with the rest projected for upgrades in time for the high luminosity p-p running.

10   Collaborating Institutions

The following institutions (listed with the contact person) have agreed to participate in construction of the EEMC.
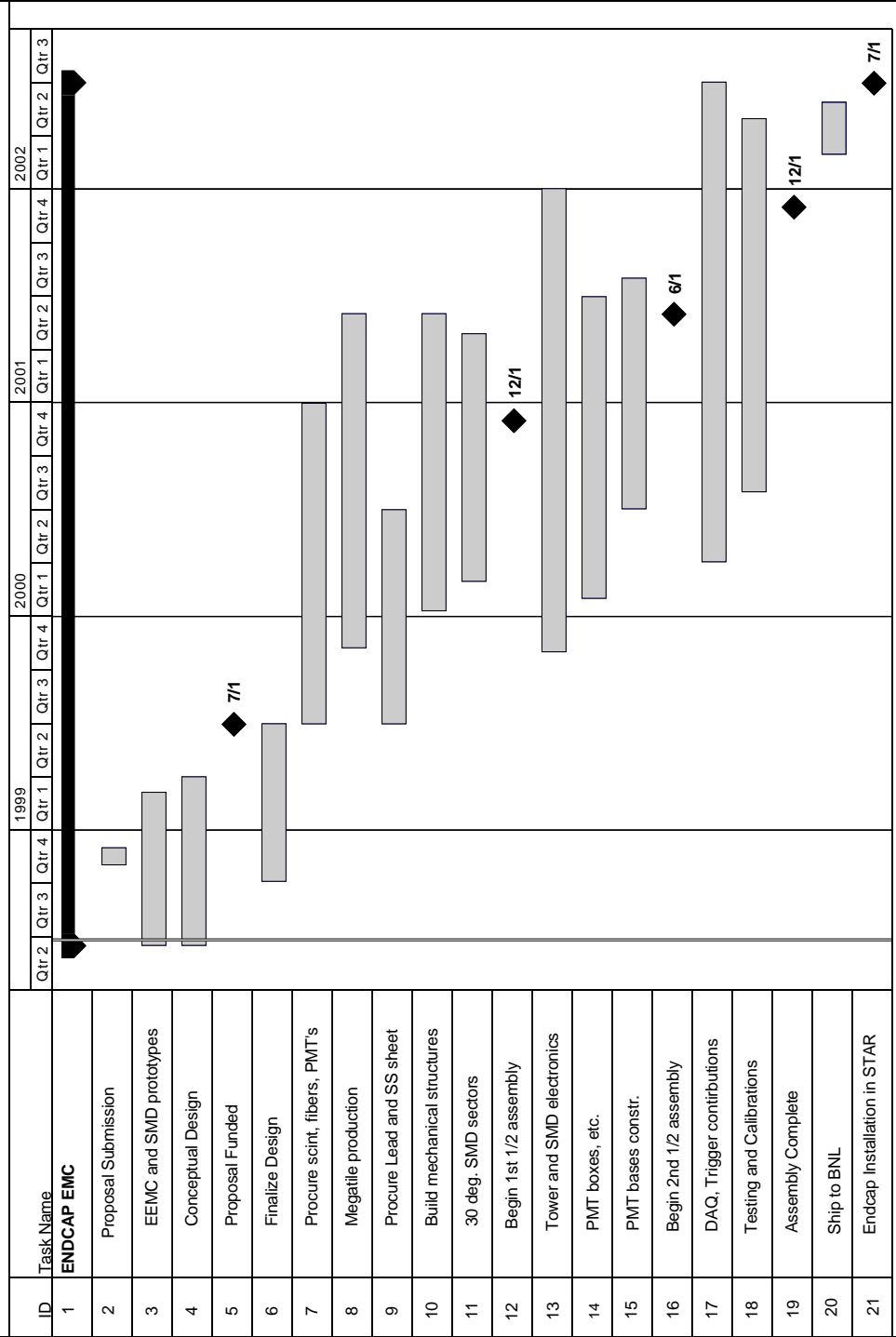
- **Argonne National Laboratory** (H. Spinka)

- **Brookhaven National Laboratory** (T. Hallman)

- **Dubna (JINR) Laboratory of High Energy Physics** (Y. Panebratsev)

- **Dubna (JINR) Laboratory for Particle Physics** (I. Savin)

- **IUCF/Indiana** (S. Vigdor)

- **Kent State University** (B. Anderson)

- **Michigan State University** (G. Westfall)

- **Penn State University** (S. Heppelman)

- **Rice University** (G. Eppley)

- **UCLA** (G. Igo)

- **U. Texas at Austin** (G. Hoffman)

- **Wayne State University** (T. Cormier)

11   Projected Milestones

The goal of the EMC endcap proposal will be completion of the project in time to install the EEMC in the west end of the STAR detector during the summer break in the running schedule for the year 2002. This overlaps with the timeline for installation of the final modules of the barrel EMC. By that time, polarized proton collisions at the luminosities assumed in this proposal should be available at RHIC, so that the full research program outlined above can be initiated promptly. In particular, this schedule will allow STAR's superior measurement of ΔG to be carried out on a time scale comparable to that of the competing experiments COMPASS [12] and PHENIX [11].

While a detailed plan of the construction is not yet in place, several key milestones we envision as necessary to maintain a proper construction schedule are indicated on the accompanying schematic Gantt chart, organized by calendar years.

PRELIMINARY SCHEDULE MILESTONES FOR THE STAR ENDCAP
ELECTROMAGNETIC CALORIMETER

ID	Task Name
1	**ENDCAP EMC**
2	Proposal Submission
3	EEMC and SMD prototypes
4	Conceptual Design
5	Proposal Funded
6	Finalize Design
7	Procure scint, fibers, PMT's
8	Megatile production
9	Procure Lead and SS sheet
10	Build mechanical structures
11	30 deg. SMD sectors
12	Begin 1st 1/2 assembly
13	Tower and SMD electronics
14	PMT boxes, etc.
15	PMT bases constr.
16	Begin 2nd 1/2 assembly
17	DAQ, Trigger contirbutions
18	Testing and Calibrations
19	Assembly Complete
20	Ship to BNL
21	Endcap Installation in STAR

Timeline columns: 1999 (Qtr 2, Qtr 3, Qtr 4), Qtr 1, Qtr 2, Qtr 3; 2000 (Qtr 4, Qtr 1, Qtr 2, Qtr 3); 2001 (Qtr 4, Qtr 1, Qtr 2, Qtr 3, Qtr 4); 2002 (Qtr 1, Qtr 2, Qtr 3)

Milestones: 7/1, 12/1, 6/1, 12/1, 7/1

Legend:
Task
Split
Progress
Milestone

Summary
Rolled Up Task
Rolled Up Split
Rolled Up Milestone

Rolled Up Progress
External Tasks
Project Summary

Project: STAR Endcap EMC
Date: Fri 6/26/98

87

References

[1] G. Bunce *et al.*, Particle World **3**, 1 (1992); Y.I. Makdisi, in *Proc. 12th Intl. Symp. on High-Energy Spin Physics*, eds. C.W. de Jager *et al.* (World Scientific, Singapore, 1997), p. 107; H. En'yo, *ibid.*, p. 118.

[2] M.A. Shifman, A.I. Vainstein and V.I. Zakharov, Phys. Lett. **B78**, 443 (1978).

[3] *Proposal to Construct an Endcap Electromagnetic Calorimeter for Spin Physics at STAR*, available at public ftp site ftp://ftp.iucf.indiana.edu/pub/iustar/eemc_proposal.ps.gz, and at url http://www.iucf.indiana.edu/Experiments/STAR/BNL_proposal.html.

[4] D. Adams *et al.*, Phys. Rev. **D56**, 5330 (1997), and references therein.

[5] F. Schlumpf and S.J. Brodsky, Phys. Lett. **B360**, 1 (1995), and references therein; N. Isgur, in *Physics with Polarized Beams on Polarized Targets*, eds. J. Sowinski and S.E. Vigdor (World Scientific, Singapore, 1990) p. 252.

[6] For a recent review, see H.Y. Cheng, Int. J. Mod. Phys. **A11**, 5109 (1996).

[7] T. Gehrmann and W.J. Stirling, Phys. Rev. **D53**, 6100 (1996).

[8] C. Bourrely, J. Soffer, F.M. Renard and P. Taxil, Phys. Rep. **177**, 319 (1989).

[9] L.E. Gordon and W. Vogelsang, Phys. Rev. **D49**, 170 (1994).

[10] J. Huston *et al.*, Phys. Rev. **D51**, 6139 (1995).

[11] N. Hayashi, Y. Goto and N. Saito, in SPIN96 Proceedings, ed. C.W. de Jager *et al.* (World Scientific, Singapore, 1997), p. 349.

[12] G.K. Mallot *et al.*, in SPIN96 Proceedings, ed. C.W. de Jager *et al.* (World Scientific, Singapore, 1997), p. 441.

[13] A. Bruell, in SPIN98 Proceedings, eds. N. Tyurin *et al.* (World Scientific, Singapore, to be published in 1999).

[14] G. Rädel, A. De Roeck and M. Maul, preprint *hep-ph/9711373* (1997).

[15] E. Laenen, G. Oderda and G. Sterman, preprint *hep-ph/9806467* (1998).

[16] T.P. Cheng and L.-F. Li, Phys. Rev. Lett. **80**, 2789 (1998), and references therein.

[17] C. Bourrely and J. Soffer, Phys. Lett. **B314**, 132 (1993).

[18] M.A. Doncheski *et al.*, Phys. Rev. **D49**, 3261 (1994).

[19] D. de Florian, M. Stratmann and W. Vogelsang, Phys. Rev. Lett. **81**, 530 (1998).

[20] M. Burkardt and R.L. Jaffe, Phys. Rev. Lett. **70**, 2537 (1993).

[21] P. Taxil and J.M. Virey, Phys. Lett. **B364**, 181 (1995) and Phys. Rev. **D55**, 4480 (1997).

[22] S.J. Brodsky and G.P. Lepage, Phys. Rev. **D22**, 2157 (1980) and Phys. Rev. **D24**, 2848 (1981).

[23] J. Ralston and D.E. Soper, Nucl. Phys. **B152**, 109 (1979).

[24] R.L. Jaffe, in Proc. 2nd Topical Workshop on Deep Inelastic Scattering off Polarized Targets, DESY, 1997 (preprint hep-ph/9710465), and references therein.

[25] R.L. Jaffe, Xuemin Jin and Jian Tang, Phys. Rev. Lett. **80**, 1166 (1998).

[26] X.-N. Wang and M. Gyulassy, Phys. Rev. Lett. **68**, 1480 (1992).

[27] A.H. Mueller and J.-W. Qiu, Nucl. Phys. **B268**, 427 (1986).

[28] E. Courant, in Proc. RHIC Spin Workshop, Brookhaven National Laboratory, April 1998.

[29] G. Apollinari, P. de Barbaro and M. Mishina, in Proc. 4th Intl. Conf. on Calorimetry in High Energy Physics, Elba, 1993; CDF II Technical Design Report, FNAL Pub-96/390-E, see http://www-cdf.fnal.gov/upgrades/tdr/tdr_8_plug_cal.html.

[30] W. Vogelsang and A. Vogt, Nucl. Phys. B**453**, 334 (1995).

[31] M.E. Beddo, H. Spinka and D.G. Underwood, STAR Note 77 (1992).

[32] T. Sjöstrand, Comp. Phys. Commun. **82**, 74 (1994).

[33] J. Alitti *et al.*, Phys. Lett. B**299**, 174 (1993).

[34] F. Abe *et al.*, Phys. Rev. D**48**, 2998 (1993).

[35] R. Brun *et al.*, GEANT User's Guide, CERN Program Library W5103.

[36] M. Adams *et al.*, Nucl. Instrum. Meth. A**378**, 131 (1996).

[37] W.B. Christie and K. Shestermanov, STAR Note 196 (1995).

[38] *Technical Design Report for the Barrel EMC in STAR* (1998), available at web site http://rsgi01.rhic.bnl.gov/star/starlib/doc/www/html/emc_l/emc.html.

[39] W.B. Christie, STAR Note 169 (1995).

[40] *Proposal for a Level-3 Trigger and Data Compression System for STAR* (1998), available at web site http://rsgi01.rhic.bnl.gov/star/starlib/doc/www/star.html.

[41] W. Edwards, private communication.

[42] R. Brown, private communication.

[43] Calculations have been done using the program Mechanica from Parametric Technology Corp. Full 3D calculations have not been used. Instead a feature utilizing shells of 2D planes and 1D beam elements with properties of the full structure have been employed to limit computing time.

[44] S. Kim, Nucl. Instr. Meth. A**360**, 206 (1995).

[45] One part TiO is mixed with 2 parts Dow DER 332 resin by weight. Jeffamine D230 hardener from Texaco is then mixed in to form the filler for the isolation grooves.

[46] S. Aota *et al.*, Nucl. Instr. Meth. A**357**, 71 (1995).

[47] S. Kuhlmann, private communication (1998).

[48] A.A. Derevschikov *et al.*, STAR Note 305 (1997).

[49] NIM A381(1996) 349-354

[50] NIM A394(1997) 27-34